

**Alma Mater Studiorum – Università di Bologna**

**DOTTORATO DI RICERCA IN SCIENZE CHIMICHE**

**Ciclo XXVII°**

**Settore Concorsuale di afferenza: 03/B1- Fondamenti delle Scienze Chimiche e  
Sistemi Inorganici**

**Settore Scientifico disciplinare: CHIM/03- Chimica Generale ed Inorganica**

**SYNTHESIS AND CHARACTERIZATION OF FUNCTIONAL INORGANIC  
NANO-MICRO PARTICLES AND THEIR ROLE IN INNOVATIVE  
PRACTICAL APPLICATIONS**

**Presentata da:**

**Dott. Eros D'Amen**

**Coordinatore Dottorato**

**Prof. Aldo Roda**

**Relatore**

**Prof.ssa Simona Fermani**

**Esame finale anno 2016**



## ABSTRACT

In this thesis, the synthesis of nano-micro particles of crystalline inorganic materials and four different applications involving their use, are presented. Inorganic particles have been synthesized following two main criteria: i) the particle's dimensions, specific surface area and crystalline phase of the product have been optimized for the practical application; ii) both the synthesis and application should be based on a simple procedure, environmental low impact, economical affordability.

In particular, Titanium dioxide nanoparticles have been synthesized by sol-gel hydrolysis of Titanium(IV) isopropoxide in an isopropyl alcohol/water solution. The isopropyl alcohol contained in the solvent mixture act as a capping agent stabilizing the forming nanometric particles, and play also a role in the suspension stability. Synthesized Titanium dioxide reveals good photocatalytic properties directly as synthesized, without needing further thermal treatment. Photoactive Titanium dioxide have been used for NO<sub>x</sub> pollutants abatement on waste gases produced by a working plant and as self-cleaning coating on photovoltaic Silicon panels, showing good results.

Crystalline calcium phosphate nano and micro particles, in particular Hydroxyapatite, Brushite, Monetite and Mg-doped  $\beta$ -Tricalcium phosphate have been synthesized. Two applications of the synthesized Calcium phosphates are reported, both based on the drug delivery concept.

Hydroxyapatite nanocrystals were used to adsorb and retain on their surface anticancer drugs based on a Platinum complex, and release them in response to a pH variation.

Phytotherapics active elements have been stabilized by physisorption on Calcium phosphates particles surface. The administration of the obtained suspensions shows good results in terms of plant's healing, using a lower amount of phytotherapeutic elements compared to the commercial products.

## RIASSUNTO

In questa tesi sono riportate sintesi e caratterizzazione di nano-micro particelle di materiale cristallino inorganico, e quattro loro applicazioni. Le particelle inorganiche sono state preparate seguendo due criteri principali: i) le proprietà chimico-fisiche delle particelle devono essere ottimizzate in funzione dell'applicazione; ii) sintesi e applicazione devono essere basate su procedure semplici, con basso impatto ambientale ed economicamente sostenibili. In particolare, nano particelle di Titanio biossido sono state sintetizzate tramite reazione di idrolisi di Titanio(IV) isopropossido in una soluzione di acqua a alcol isopropilico. L'alcol isopropilico presente nella miscela di solventi agisce da agente capping stabilizzando le nanoparticelle in formazione e dimostra un ruolo nella stabilità della sospensione. Il Titanio biossido prodotto ha rivelato buone proprietà foto catalitiche senza bisogno di ulteriori trattamenti termici. Il Titanio biossido foto attivo è stato applicato con buoni risultati nell'abbattimento di NOx dalle emissioni di uno stabilimento e come strato autopulente su dei pannelli fotovoltaici. Sono state sintetizzate nano e micro particelle di calcio fosfati cristallini, nello specifico Idrossiapatite, Brushite, Monetite and  $\beta$ -Tricalcio fosfato Mg-sostituito. Ne sono riportate due applicazioni, entrambe basate sul concetto di *drug delivery*. Nanocristalli di Idrossiapatite sono stati utilizzati per adsorbire e ritenere sulla loro superficie farmaci chemioterapici basati su complessi di Platino, e successivamente rilasciare il farmaco in risposta ad una variazione di pH. Alcuni principi attivi fitoterapici sono stati stabilizzati tramite fisisorbimento sulla superficie di particelle di Calcio fosfati in sospensione. La loro applicazione ha dimostrato buoni risultati curativi sulle piante, utilizzando quantitativi di principio attivo molto ridotti rispetto ai prodotti commerciali.

<b>INDEX</b>	<b>Pag.</b>
1-INTRODUCTION	1
1.1- NANOMATERIALS	1
1.1.1- HETEROGENEOUS CATALYSIS USING NANOMATERIALS	5
1.2- SEMICONDUCTOR MATERIALS	7
1.3- TITANIUM DIOXIDE	9
1.3.1- POLYMORPHS DESCRIPTION	10
1.3.2- PHOTOCATALYSIS MECHANISM IN SEMICONDUCTOR MATERIALS	13
1.4- CALCIUM PHOSPHATES	16
1.4.1- CALCIUM PHOSPHATES IN BIOMEDICAL APPLICATIONS	18
1.5- AIM OF THE THESIS	20
 2- EXPERIMENTAL SECTION	
2.1- PHOTOACTIVE TITANIUM DIOXIDE	22
2.1.1- TITANIUM DIOXIDE SOL-GEL SYNTHESIS ( <i>Synthesis 1</i> )	22
2.1.1.1- TITANIUM DIOXIDE THERMAL TREATMENT	23
2.1.1.2- TITANIUM DIOXIDE HETEROCOAGULATION ON SILICA ( <i>Synthesis 2</i> )	23
2.1.1.3- PHOTOACTIVITY TEST: METHYLENE BLUE SOLUTION ( <i>Experiment 1</i> )	24
2.1.2- NO <sub>x</sub> PHOTOCATALYZED ABATEMENT	25
2.1.2.1- NO <sub>x</sub> PHOTOCATALYZED ABATEMENT, STATIC CONDITIONS ( <i>Experiment 2</i> )	25
2.1.2.1.1- SILANE/SILICA SUPPORT COATING ( <i>Synthesis 3</i> )	28

2.1.2.2- NO <sub>x</sub> PHOTOCATALYZED ABATEMENT, FLUXING CONDITIONS ( <i>Experiment 3</i> )	29
2.1.2.3- NO <sub>x</sub> PHOTOCATALYZED ABATEMENT, FLUXING CONDITIONS ( <i>Experiment 4</i> )	31
2.1.2.4- NO <sub>x</sub> PHOTOCATALYZED ABATEMENT, FLUXING CONDITIONS ( <i>Experiment 5</i> )	33
2.1.3- PHOTOVOLTAIC PANELS COATING ( <i>Experiment 6</i> )	35
2.2- CALCIUM PHOSPHATES NANO-MICRO PARTICLES	36
2.2.1- SYNTHESIS OF CALCIUM PHOSPHATES	36
2.2.1.1- HYDROXYAPATITE SYNTHESIS ( <i>Synthesis 4</i> )	36
2.2.1.2- BRUSHITE SYNTHESIS ( <i>Synthesis 5</i> )	37
2.2.1.3- BRUSHITE SYNTHESIS ( <i>Synthesis 6</i> )	38
2.2.1.4- BRUSHITE SYNTHESIS ( <i>Synthesis 7</i> )	39
2.2.1.5- BRUSHITE SYNTHESIS ( <i>Synthesis 8</i> )	39
2.2.1.6- BRUSHITE SYNTHESIS ( <i>Synthesis 9</i> )	40
2.2.1.7- MONETITE SYNTHESIS ( <i>Synthesis 10</i> )	41
2.2.1.8- MONETITE SYNTHESIS ( <i>Synthesis 11</i> )	41
2.2.1.9- MONETITE SYNTHESIS ( <i>Synthesis 12</i> )	42
2.2.1.10- β-TRICALCIUM PHOSPHATE SYNTHESIS ( <i>Synthesis 13</i> )	42
2.2.1.11- β-TRICALCIUM PHOSPHATE SYNTHESIS ( <i>Synthesis 14</i> )	43
2.2.1.12- BIOMIMETIC POROUS SCAFFOLD SYNTHESIS ( <i>Synthesis 15</i> )	43
2.2.1.13- BIOMIMETIC POROUS SCAFFOLD SYNTHESIS ( <i>Synthesis 16</i> )	44
2.2.2- CALCIUM PHOSPHATES FOR BIOMEDICAL DRUG DELIVERY	45

2.2.2.1- ANTICANCER Pt COMPLEX PHYSISORPTION ON HYDROXYAPATITE ( <i>Synthesis 17</i> )	45
2.2.2.2- ANTICANCER Pt COMPLEX PHYSISORPTION ON HYDROXYAPATITE ( <i>Synthesis 18</i> )	46
2.2.2.3- ANTICANCER Pt COMPLEXES RELEASE FROM HYDROXYAPATITE ( <i>Experiment 7</i> )	47
2.2.3- CALCIUM PHOSPHATES FOR PHYTOTHERAPICAL DRUG DELIVERY	48
2.2.3.1- COPPER SULFATE PHYSISORPTION ON HYDROXYAPATITE ( <i>Synthesis 19</i> )	48
2.2.3.2- SULFUR PHYSISORPTION ON BRUSHITE ( <i>Synthesis 20</i> )	48
2.2.3.3- PHYTOTHERAPIC DRUGS DELIVERY TEST ( <i>Experiment 8</i> )	49
2.3- CHEMICAL-PHYSICAL CHARACTERIZATION TECHNIQUES	51
2.3.1- SCANNING ELECTRON MICROSCOPY IMAGING	51
2.3.2- TRANSMISSION ELECTRON MICROSCOPY IMAGING	54
2.3.3- X-RAY POWDER DIFFRACTION	55
2.3.4- DINAMIC LIGHT SCATTERING SIZE DETERMINATION	57
2.3.5- SURFACE AREA DETERMINATION (BET)	58
2.3.6- UV-VISIBLE SPECTROSCOPY	60
2.3.7- INDUCTIVELY COUPLED PLASMA OPTICAL EMISSION SPECTROMETRY	64

### 3- RESULTS AND DISCUSSION

3.1- PHOTOACTIVE TITANIUM DIOXIDE	66
3.1.1- TITANIUM DIOXIDE CHARACTERIZATION ( <i>Synthesis 1</i> )	66

3.1.1.1- PHOTO ACTIVITY TEST: METHYLENE BLUE SOLUTION ( <i>Experiment 1</i> )	73
3.1.2- TITANIUM DIOXIDE THERMAL TREATMENT, CHARACTERIZATION	78
3.1.2.1- PHOTO ACTIVITY TEST: METHYLENE BLUE SOLUTION	79
3.1.3- TITANIUM DIOXIDE HETEROCOAGULATION ON SILICA, CHARACTERIZATION ( <i>Synthesis 2</i> )	80
3.1.3.1- PHOTO ACTIVITY TEST: METHYLENE BLUE SOLUTION	82
3.1.4- UV SOURCE COMPARISON	83
3.1.5- NO <sub>x</sub> PHOTOCATALYZED ABATEMENT, STATIC CONDITIONS ( <i>Experiment 2</i> )	87
3.1.5.1- STATIC REACTOR - BLANK MEASUREMENT	87
3.1.5.2- STATIC REACTOR - CATALYST EFFECTIVENESS EVALUATION	89
3.1.5.3- SILANE/SILICA SUPPORT COATING ( <i>Synthesis 3</i> )	91
3.1.6- NO <sub>x</sub> PHOTOCATALYZED ABATEMENT, FLUXING CONDITIONS ( <i>Experiment 3</i> )	94
3.1.7- NO <sub>x</sub> PHOTOCATALYZED ABATEMENT, FLUXING CONDITIONS ( <i>Experiment 4</i> )	98
3.1.8- NO <sub>x</sub> PHOTOCATALYZED ABATEMENT, FLUXING CONDITIONS ( <i>Experiment 5</i> )	101
3.1.9- PHOTOVOLTAIC PANELS COATING ( <i>Experiment 6</i> )	108
3.2- CALCIUM PHOSPHATES NANO-MICRO PARTICLES	115
3.2.1- CHARACTERIZATION OF CALCIUM PHOSPHATES	115
3.2.1.1- HYDROXYAPATITE CHARACTERIZATION ( <i>Synthesis 4</i> )	115
3.2.1.2- BRUSHITE CHARACTERIZATION ( <i>Synthesis 5</i> )	118
3.2.1.3- BRUSHITE CHARACTERIZATION ( <i>Synthesis 6</i> )	120

3.2.1.4- BRUSHITE CHARACTERIZATION ( <i>Synthesis 7</i> )	122
3.2.1.5- BRUSHITE CHARACTERIZATION ( <i>Synthesis 8</i> )	124
3.2.1.6- BRUSHITE CHARACTERIZATION ( <i>Synthesis 9</i> )	126
3.2.1.7- MONETITE CHARACTERIZATION ( <i>Synthesis 10</i> )	127
3.2.1.8- MONETITE CHARACTERIZATION ( <i>Synthesis 11</i> )	129
3.2.1.9- MONETITE CHARACTERIZATION ( <i>Synthesis 12</i> )	131
3.2.1.10- $\beta$ -TRICALCIUM PHOSPHATE CHARACTERIZATION ( <i>Synthesis 13-14</i> )	133
3.2.1.11- BIOMIMETIC POROUS SCAFFOLD CHARACTERIZATION ( <i>Synthesis 15</i> )	135
3.2.1.12- BIOMIMETIC POROUS SCAFFOLD CHARACTERIZATION ( <i>Synthesis 16</i> )	137
3.2.2- CALCIUM PHOSPHATES FOR BIOMEDICAL DRUG DELIVERY	139
3.2.2.1- ANTICANCER Pt COMPLEXES PHYSISORPTION ON HYDROXYAPATITE ( <i>Synthesis 17- 18</i> )	139
3.2.2.2- ANTICANCER Pt COMPLEXES RELEASE FROM HYDROXYAPATITE ( <i>Experiment 7</i> )	142
3.2.3- CALCIUM PHOSPHATES FOR PHYTOTHERAPICAL DRUG DELIVERY	144
3.2.3.1- PHYTOTHERAPIC DRUGS DELIVERY TEST ( <i>Experiment 8</i> )	144
4- CONCLUSIONS AND PERSPECTIVES	148
5- BIBLIOGRAPHY	151



# 1-INTRODUCTION

## 1.1- NANOMATERIALS

In the 1959 at the annual meeting of American Physical Society, the Nobel prize Richard Feynmann gave the famous speech “ there’s plenty of room at the bottom”, that focused on the emerging interest towards nanoscale science. During the years, the scientific research addressed a growing interest to nanoscale manipulation and understanding, and nowadays nanomaterials are commercialized and used as commodity. According to the definition reported in [ISO/TS27678, Nanotechnology- Terminology and definitions, Sept. 2008], a nanomaterial is an object showing at least one dimension in the 1-100 nm scale. On the basis of this definition, a first classification of nanomaterials can be made, referring to their dimensionality:

- Zero dimensional materials ( nanocrystals, nanoclusters, Quantum Dots )
- One dimensional materials ( nanowires, nanotubes )
- Two dimensional materials ( nanofilms, 2D arrays )
- Three dimensional materials ( nanostructured bulk solids, zeolites, etc. ), even if not included in the nanomaterials definition, have to be mentioned.

Apart for the ambitious challenge that the synthesis and manipulation of such objects represents, the enormous attention drawn by this materials is certainly due to the unique features they shows. In fact, in virtue of their dimension, nanomaterials exhibit a dramatic change in their intrinsic properties compared to the bulk. A bulk material should have constant physical/chemical features regardless its size, but decreasing dimensions to the nanoscale, new size-dependent properties appears and became predominant. In particles of nanometric scale, the surface to bulk ratio is significantly higher than in macroscopic objects, and their properties are dominated by surface chemistry and physics.

Quantum phenomena like surface plasmon resonance in metals/semimetals, quantum size confinement in semiconductors and superparamagnetism in magnetic material,s become relevant and affect macroscopic properties observed in nanomaterials [J.T.Lue, Enc. Nanoscien. Nanotech., vol. 10, 1-46], such as:

- Insulating properties
- Size-tunable optical emission frequency
- Field emission
- Electrical conduction
- Dielectric constant
- Quantum tunneling
- Magneto-resistance
- Ferromagnetic resonance
- Linear optical properties
- Non linear optical generation

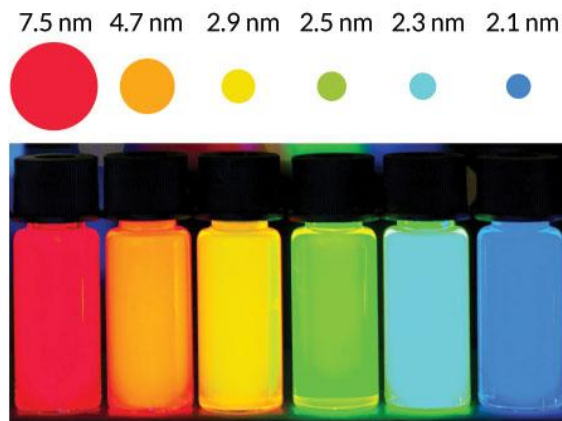


*Fig. 1 – Example of Size-tunable optical emission frequency from Quantum dots [images from: [www.Sciencenews.org](http://www.Sciencenews.org)]*

Nanoparticles are also characterized by a very high specific surface area values, which results in enhanced reactivity and enormous driving force for diffusion. This makes possible, for example, sintering processes performed at very low temperature compared to bulk melting point. In virtue of their huge potential, still poorly mastered, nanomaterials are beginning to find a role in practical applications, as summarized in the following table reported by Gaffet, 2011 (*Tab. 1*).

<b>Nanomaterials</b>	<b>Application fields</b>
<b>Nanoceramics</b>	Structural composite materials - components anti - UV - polishing substrates (wafers) in microelectronics Chemical - photocatalytical applications
<b>Nanometallics</b>	Antimicrobial and/or sector of catalysis - conductive layers of screens, sensors or energetic materials.
<b>Nanoporous</b>	Aerogels for thermal insulation in the areas of electronics, optics and catalysis - bio - medical field for tracing or even implants type applications.
<b>Nanotubes</b>	Electrical conductive nanocomposites - structural materials - single-walled nanotubes for applications in the field of electronics, screens
<b>Massive Nanomaterials</b>	Hard coatings - structural components for the aerospace industry, automotive, pipes for oil and gas, sport or even anticorrosion sector industries.
<b>Dendrimers</b>	Medical field (administration of drugs, rapid detection) - domain cosmetic.
<b>Quantum Dots</b>	Optoelectronics (screens) - photovoltaic cells - inks and paints for applications of type marking anti - counterfeiting
<b>Fullerenes</b>	Sport (nanocomposites) and cosmetics sectors
<b>Nanowires</b>	Applications in the conductive layers of screens or even solar cells and electronic devices

*Tab. 1 – Main application fields of nanomaterials, [E.Gaffet, 2011]*

Beside the enthusiasm generated by these promising technologies, an accurate and cautious evaluation of their effects on health have to be done. Their enhanced reactivity, their capability of migrate through tissues and cellular membrane and accumulate in certain organs may in fact cause health hazards and new pathologies. Among various proposed theories, recent publications refers mainly to two type of mechanism as the origin of specific toxicity of nanoparticles [J. Boczkowski, et al., 2010]:

- Surface adsorption of biologically active molecules: because of their relevant specific surface area, nanoparticles can adsorb and retain biologically active molecules. Especially if those molecules are secreted in controlled quantities, such as growth factor, their sequestration may induce cells suffering or death.
- Oxidative stress induction: metal nanoparticles can generate a relevant amount of free radicals on their surface, or induce their production by cells. Highly reactive radicals can attack and damage both cell's walls or DNA, leading to inflammation reactions, fibrosis

or favor cancerous processes. Moreover, exposure to some kind of carbon nanotubes may cause similar damages to those induced by asbestos.

Overall, actual data about specific nanoparticles toxicity are limited. It appears actually difficult to fully understand the biological effect of such reactive and mobile particles, and mostly to determine their long term effects.

### 1.1.1- HETEROGENEOUS CATALYSIS USING NANOMATERIALS

Particular attention to nanomaterials have been given by the science of heterogeneous catalysis. Great majority of currently used catalyst are in fact solids, and unique behaviors of nanosized solid materials are crucial to improve efficiency or sustainability of many catalytic processes.

First and essential step in every heterocatalyzed reaction is the adsorption of reactants molecules on catalyst surface. Mainly two types of interaction can occur between adsorbent and adsorbate:

- Physisorption, characterized by weak interactions mainly determined by Van der Waals forces, ranging from 2 to 10 kcal/mol in energy. Physisorption produces only small perturbations to the adsorbate's electronic structure.
- Chemisorption, characterized by strong interactions ( 15 to 100 kcal/mol of energy ) occurring between adsorbent and adsorbate, which share the electron density. Heavy perturbations are produced to adsorbate's electronic structure, and bonds breaking may occur concomitantly with the adsorption.
- Key parameters for reactions involving such processes are transport phenomena, dispersion and, primarily, surface chemistry. In particular, surface chemistry play a major role in determining physical/ chemical phenomena occurring at the interface of the two phases. For example, at the surface of crystalline solids the lattice regularity is interrupted, determining a distortion in the electronic band structure and resulting in an interface characterized by a higher free energy compared to the bulk. Furthermore, defective structures often occur at the border surface, and defects may generate different reactivity sites. In virtue of their high specific surface area values and high surface to bulk ratio, nanomaterials are preferred candidates to cover the role of heterogeneous catalysts. Higher reactivity and higher number of disposable active sites guarantees relevant advantages compared to conventional macroscopic catalyst [Fukui, et al., 2004; Zalesskiy, et al., 2012] as:
  - increased efficiency and higher conversion rates;
  - higher retention of catalytic activity after recycling;
  - possibly to work under milder conditions, avoiding nanoparticles denaturation

In order to ensure nanoparticles catalytic behavior and avoid aggregation phenomena resulting in a loss of activity or uncontrolled losses of nanoscaled material, stabilization technologies are applied. Nanoparticulate metals are commonly stabilized in solutions by functionalization steps involving ligands, polymers or oligomers [Roucoux, et al., 2002]. Otherwise nanocatalysts can be anchored on a support which usually is a solid characterized by a high surface area. The catalyst support may be inert or have a role in the reaction [Ma, et al., 2006].

## 1.2- SEMICONDUCTOR MATERIALS

The energy and distribution of electrons in a solid material are described by the band theory that considers the quantum energy level and wave functions of an electron in a large periodic lattice of atoms. On an isolated atom, an electron occupies atomic orbitals, defined by discrete energy levels. When atoms combine, new wave functions (molecular orbitals) each one characterized by a discrete energy level, are obtained, from the overlapping of atomic orbitals. In the case of solids, Avogadro's numbers of atoms overlaps their orbitals producing a massive number of molecular orbitals. By increasing the number of atoms the energy levels related to molecular orbitals became increasingly dense, until they became so close to lose their discrete character, being considered a continuum. What arises are the so called bands, i.e. regions of allowed energies for the solid electrons, and band gaps, i.e. unoccupied regions of prohibited energies, that separate bands. This theory gives a simplified model of solid materials based on the assumption of an infinite homogeneous system of static potential where an electron moves), but is useful to explain some phenomena, like the conduction in solids. By filling bands with electrons starting from the lower energies, the highest energy occupied band is called the "valence band" containing the outermost electrons, while the lowest unoccupied will be the "conduction band". Dependently on the lattice structure and the nature of the atoms, the valence and conduction bands may be separated by a band gap of variable amplitude. On the basis of the width of this band gap, materials are classified in conductors, semiconductors or insulators. A more accurate description of bands filling is introduced the by Fermi level definition according to which at the thermodynamic equilibrium, the probability for a state of a given energy E to be occupied by an electron is expressed by the Fermi-Dirac distribution:

$$f(E) = \frac{1}{1 + e^{\frac{E-E_F}{k_B T}}}$$

where  $k_B$  is the Boltzmann's constant, T is the temperature in Kelvin° and  $E_F$  is the Fermi energy. The Fermi energy defines the energy of the highest occupied level in a fermions system at 0 °K, considering Pauli's exclusion principle. For temperatures above zero, the Fermi-Dirac distribution describes the electron occupancy of the states while the Fermi level indicates the energy level having a probability equal to ½ of being populated. This probability, and in consequence the electron density, rapidly decreases for the energy levels higher than  $E_F$  and

increases for the lower levels. By coupling Fermi-Dirac distribution with the band theory, a more accurate description of solids conduction behavior can be done:

- In a Conductor (metal or semimetal), the Fermi level lies inside one or more superimposed allowed bands. This determines a partial occupancy of that band and as a consequence its charge mobility behavior.
- In semiconductors the Fermi level lies inside the band gap between valence band and conduction band. The band gap of semiconductors is not very wide, like for Silicon (1.21 eV), for this reason electrons can be promoted from the occupied valence band to the unoccupied conduction band. Population of states higher in energy requires thermal or photoinduced excitation, that have to provide to electrons an amount of energy equal or higher to the band gap. For this reason, the conductive character of thermal semiconductors is shown only at high temperature, while at low temperature the conduction band is not populated.
- In insulator, like in semiconductors, the Fermi level lies inside the band gap between valence band and conduction band. Unlike semiconductors, the wide separation of the band gap makes impossible to obtain a sufficient population of conduction band to perform efficient charge transport.

Charge transfer may occur in consequence of two different mechanisms. Each electron promoted to the conduction band creates an empty and positive hole in the valence band. While electrons are the effective charge carriers moving through the partially occupied conduction band, the lack of charge in valence band creates a different mechanism of charge transport: nearby electrons move to fill the hole creating new gaps, and so on. The result is a “motion of gaps” acting as positive charges freely moving within the valence band. Conduction in a solid can be determined by one or both this phenomena. Moreover, some materials can be turned in semiconductors by doping with different atoms: extrinsic semiconductors are obtained by purposely adding conduction electrons ( n-type doping ) or valence holes ( p-type doping ) to the structure. The presence of defects in a crystalline solid may affect its properties both locally or overall. It is possible in fact that a local change in electron-hole recombination efficiency may determine an higher amount of disposable charge carrier for the whole solid, or act as preferred sites of interaction between electron-hole couples and other molecules adsorbed on the solid’s surface.

### 1.3- TITANIUM DIOXIDE

Titanium dioxide is an inorganic semiconductor material actually representing one of the most known, studied and important material that find application in a wide range of fields. Relevant features responsible of such interest toward this material are its chemical stability, non toxicity, relatively low production costs and manageability together with its useful optical, chemical and physical properties. For example, Titanium dioxide powder shows one of the highest reflective index value coupled with strong hiding power and high degree of whiteness, making it an excellent industrial pigment. In addition, it can be easily dispersed in solvents or aqueous media, justifying its wide applicability in many fields as paints, ceramic, plastic, food, pharmaceutical and cosmetic additive. Recently, Titanium dioxide pigment production through the world is estimated in four million tons per year [ Kronos international, 1996]. From 60s, Titanium dioxide found a leading role in many other technological applications, especially in energy and environmental fields, due to its peculiar physical-chemical features as photoactive semiconductor [A. Fujishima, 1999], [K. Hashimoto, et al., 2005]. Crystalline Titanium dioxide can be found at least in eight different polymorph structures. In nature it is present in four minerals: Rutile, Anatase, Brookite and the rarest and less known Columbite-structured TiO<sub>2</sub>. In addition to these, Titanium dioxide shows a rich phase diagram at elevated pressure, crystalline structures similar to Baddelayite, Cotunnite, Pyrite and Fluorite have been described in literature by high pressure coupled techniques [ T. Zhu, et al., 2014 ]. Among the commonly occurring polymorphs the most thermodynamically stable form and also the most abundant is Rutile, while Brookite and Anatase are metastable phases and may be thermally converted into Rutile.

### 1.3.1- POLYMORPHS DESCRIPTION

- **Rutile**

In nature Rutile is found as a mineral mainly composed of Titanium dioxide, that may contain up to 10% of Iron, and relevant amount of Niobium and Tantalum. Its name comes from the Latin word “Rutilus” because of the deep red color observable in some specimen (*Fig.2a*). Rutile can be found in metamorphic or igneous rocks formed at high temperatures and pressures. It crystallizes in a Tetragonal crystal system with cell parameters of  $a=b= 4.587 \text{ \AA}$ ,  $c= 2.954 \text{ \AA}$ , an space group  $P4_2/mnm$ . The base for this structure is a Titanium atom coordinated by six oxygen atoms arranged in a distorted octahedron, resulting in two different Titanium-Oxygen bond lengths (*Fig.2b*).

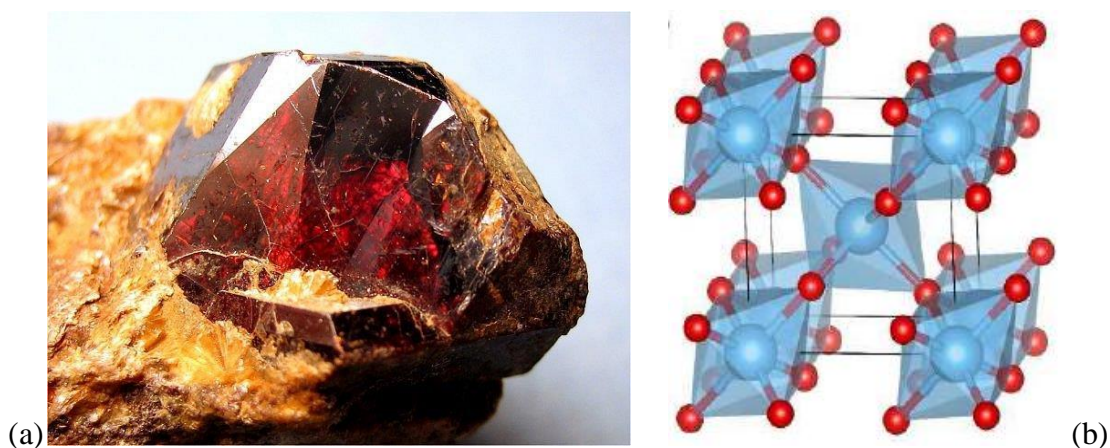


*Fig. 2 – Rutile mineral image (a) and crystalline cell schematization(b), Titanium atoms are represented as blue spheres, Oxygen atoms are represented as red spheres [www.minerali.it, T. Zhu, et al., 2014]*

Rutile is a direct band gap semiconductor, with an experimentally measured band gap of  $3.3 \pm 0.5 \text{ eV}$  [Y. Tezuka, et al., 1994]. However, it is known that Rutile exhibits a scarce activity as photocatalyst and is mainly used in Titanium production and as pigment. In fact, fine powders of Rutile show one of the highest reflectivity index among materials and a bright white color, features that make it widely used in the production of paints, plastic, refractory ceramics, paper, food and cosmetics. In fact, since the nanoparticles of Rutile are transparent to the visible light, but strongly absorb UV radiation, Rutile is also used as screen to protect skin from UV hazards.

- **Brookite**

Brookite is a natural polymorph, sometimes found together with Rutile in an epitaxial face relationship. Like Rutile, it shows a high reflective index, modest Mohs hardness and brownish to red coloration due to metal impurities (*Fig.3a*). It crystallizes in an Orthorhombic crystal system, with lattice parameters of  $a = 9.263 \text{ \AA}$ ,  $b = 5.510 \text{ \AA}$ ,  $c = 5.167 \text{ \AA}$ , and a space group  $Pbca$ . The brookite structure is built up of distorted octahedra with a Titanium ion at the center and oxygen ions at each of the six vertices. Each octahedron shares three edges with the adjoining ones (*Fig.3b*)

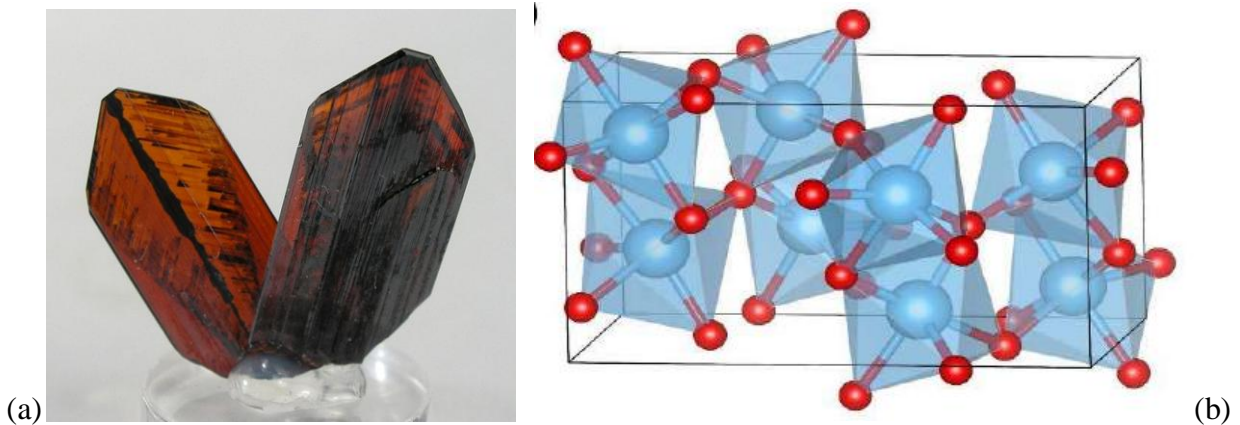


*Fig. 3 – Brookite mineral image (a) and crystalline cell schematization (b), Titanium atoms are represented as blue spheres, Oxygen atoms are represented as red spheres [www.minfind.com, T. Zhu, et al., 2014]*

Like Rutile, Brookite is a direct band gap semiconductor, with a calculated band gap of 3.86 eV [Y. Tezuka, et al., 1994]. However, like in the case of Rutile, Brookite exhibits a negligible activity as photocatalyst. Because of its rare occurrence, there are not specific application for Brookite.

- **Anatase**

Anatase naturally occurs as little, blue crystals, often showing sharply developed octahedral geometries (*Fig.4a*). It crystallizes in a Tetragonal crystal system with cell parameters of  $a=b=3.785 \text{ \AA}$ ,  $c=9.512 \text{ \AA}$ , an space group  $I4_1/amd$ . Also this structure is based on a Titanium atom coordinated by six oxygen atoms arranged in a distorted octahedron (*Fig. 4b*).

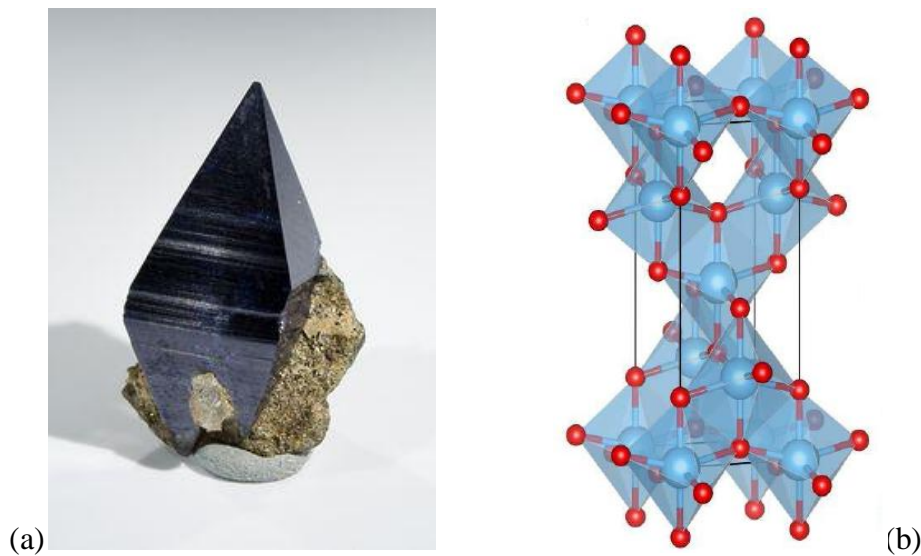


*Fig. 4 – Brookite mineral image (a) and crystalline cell schematization (b), Titanium atoms are represented as blue spheres, Oxygen atoms are represented as red spheres [www.pinterest.com, T. Zhu, et al., 2014]*

Anatase is an indirect band gap semiconductor, with an experimentally measured band gap of  $\approx 3.2 \text{ eV}$  [Y. Tezuka, et al., 1994]. Anatase shows the highest photoactivity among the three most abundant polymorph, for this reason Anatase and its application as photocatalyst have been deeply investigated. An explanation of its highest photoactivity compared to Rutile have been recently proposed by Luttrell, et al., 2014. First of all, Anatase shows an indirect band gap smaller than its direct band gap. Semiconductors with indirect band gap usually exhibit longer charge carriers life time compared to direct band gap ones. This is a consequence of the prohibited radiative recombination of conduction electrons and valence holes. Longer electron-hole pairs lifetime increases their availability in surface reactions. In addition, Anatase has a band gap larger than Rutile and it may raise the valence band maximum to higher energy levels relative to redox potentials of adsorbed molecules. This can increase the “oxidation power” of electrons toward adsorbed molecules. Lastly, in addition to exciton lifetime, the exciton mobility play a relevant role. It have been found that in Anatase along certain crystallographic

directions a major bulk transport of excitons to the surface occurs, drastically increasing electrons and holes participation to surface reactions. It is relevant to mention that phase mixtures demonstrates synergic effects, providing higher photoactivity than pure phases [Luttrell, et al., 2014]

### 1.3.2- PHOTOCATALYSIS MECHANISM IN SEMICONDUCTOR MATERIALS

Titanium dioxide, as previously reported, is a semiconductor material. Band gap values for the two most known polymorphs, Rutile and Anatase, are 3.02 eV and 3.20 eV, respectively. By referring to Plank's law:

$$E = h\nu = h \frac{c}{\lambda}$$

where E is the energy ( J), h is the Plank's constant, c is the speed of light in vacuum and  $\lambda$  is the wavelength in n,

it is possible to calculate the wavelength of an electromagnetic radiation bringing enough energy to overcome the band gap, which results in about 410 nm for Rutile and 386 nm for Anatase. In fact, both Anatase and Rutile shows an intense absorption edge in correspondence of such wavelengths, in the Ultraviolet region of the spectrum. The absorption of a photon of this specific wavelength ( or shorter ) may result in the promotion of an electron from the valence to the conduction band, determining the generation of an electron-hole couple, or exciton. Generated electrons and holes can follow different paths: recombination is surely the preferred way because of its fast kinetics. A conduction electron and a positive valence hole annihilate each other, giving back an amount of energy equal to the band gap. Recombination may occur both by radiative or non-radiative way ( thermal excitement). A charge carrier, i.e. electron or valence hole, that not undergoes immediate recombination, may migrate through the solid, usually following specific crystallographic directions [T. Luttrell, et al., 2014]. Conduction electrons and valence holes reaching the solid surface can interact with adsorbed

molecules, causing redox processes in virtue of their potential of + 2.53 V and – 0.52 V, respectively, versus the Standard Hydrogen Electrode ( SHE ) at pH 7.00. By surface redox reactions, a cascade of radicals is produced. The major active radicals are produced by reaction with adsorbed Water and Oxygen molecules, resulting in the production of:

- Hydroxyl radicals,  $\text{OH}^\bullet$  ( + 2.27 V vs SHE )
- Superoxide ions,  $\text{O}_2^{\bullet -}$  ( -0.28 V vs SHE )
- Hydrogen peroxide  $\text{H}_2\text{O}_2$  ( + 1.35 V vs SHE )

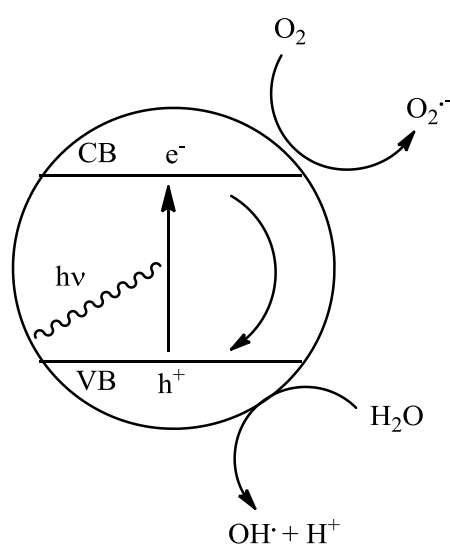


*Fig. 5 – Schematization of electron-hole couple generation and radical production*

Formed radicals can remain adsorbed on catalyst surface or migrate by diffusion mechanisms, and be involved in reactions with other molecules. It has been reported that the strong potentials exhibited by the charge carriers migrating on the solid surface and the reactive radical species can degrade several class of molecules, both organic and inorganic. In general, the degradation is slower for aliphatic compounds compared to oxygenated and aromatic molecules, especially those having an electron donor substituent, capable of activating the aromatic ring toward  $\text{OH}^\bullet$  radical electrophilic attack [J. M. Hermann, 1999] The final product of such reactions are low weight, stable, oxidized molecules. In particular, organic compounds are converted to  $\text{CO}_2$  and  $\text{H}_2\text{O}$ , Nitrogen compounds and Nitrous oxides to Nitrates and nitric acid, Sulfur compounds to sulfates [L. Frazer, 2011] .

In addition, reactive species produced on catalyst surface shows high cytotoxicity, determining an effectiveness in bacterial load abatement and surface sanification. Due to this relevant properties, Anatase Titanium dioxide and a small family of similar photoactive semiconductors ( chalcogenide oxides or sulfides ) have found many technological applications in pollutants removal and environmental solutions [A. Fujishima, 1999], [ K. Hashimoto et al., 2005]. Main fields of environmental interest are nowadays i) water treatment, ii) air purification and iii) water disinfection. Actually, the bigger limit is represented by the wide band gap of Titanium dioxide, that determines the necessity of UV photons to promote the electron-hole generation. To overcome this limit, many ways have been reported to shift the band gap energy to longer wavelengths, in the visible spectrum. Unfortunately, heavy chemical modifications are necessary to obtain an absorption redshift, such as non-metal doping (mainly Nitrogen doping), or expensive techniques like noble metals layer deposition [M. Pelaez et al., 2012].

## 1.4- CALCIUM PHOSPHATES

Calcium phosphates are minerals and also the main components of calcified tissues in vertebrates. For example bones and dentin are composed of more than the 70 % of Hydroxyapatite, a calcium phosphate containing an hydroxide group, intergrowth with organic molecules, mainly collagen. Despite Hydroxyapatite and other Calcium phosphates are naturally occurring minerals, their mechanical and morphological features cannot be compared to biogenic materials, even if characterized by the same elemental composition. Biogenic calcified tissues are in fact highly sophisticated composite materials, determined by an high degree of hierarchical organization. In bones, the Hydroxyapatite phase is non stoichiometric, carbonate substituted and poorly crystalline [Roveri, et al., 2010]. Inorganic lamellar shaped microstructures are intimately intergrowth with aligned collagen fibrils, guided by epitaxial surface recognition with fibrils charge pattern. Composite structural motifs hierarchically develop until defining both macroscopic cavities of trabecular bone and dense cortical bone, allowing vascularization and cell colonization. Every detail in structure and composition is functional to determine mechanical strength, lightness, reliability and adaptability requested to the bone tissue. Comparable properties are far to be obtained by the only mineral phase itself. Such degree of sophistication is obtained in biosynthesis by a fine spatial control of chemistry at nanoscale level. Inter-intra cellular spaces, membranes, vesicles delimitates spaces in which biomineralization can be controlled nearly at single atoms level.

Obviously Calcium phosphates are completely biocompatible and, in certain cases, shows good bioreabsorbibility. Due by their almost perfect behavior in the interaction with the biological environment, Calcium phosphates are an elective material for biomedical applications. For this reason a relevant amount of literature has been produced concerning their synthesis, characterization and appliance. Since the beginning, the major interest was addressed to these crystalline phases characterized by a Calcium to Phosphor molar ratio comprised between 1 and 2. Outside this range, Calcium phosphate phases shows high solubility and acidic or basic features, not suitable for a biological environment destination. In particular, the crystalline phases fulfilling this requirement are: Anhydrous dicalcium phosphate ( Monetite ), dicalcium phosphate dihydrate ( Brushite ), octacalcium phosphate,  $\alpha$ -tricalcium phosphate,  $\beta$ -tricalcium phosphate, Hydroxyapatite, with the inclusion of a defective Calcium deficient Hydroxyapatite

and amorphous Calcium phosphate [F. Chen, et al., 2012]. A brief description of these phases is reported in *Tab.2*.

Name, Formula	Ca/P ratio	Space group and lattice parameters
Anhydrous dicalcium phosphate ( Monetite) $\text{CaHPO}_4$	1.00	Triclinic, P1 $a = 6.910 \text{ \AA}$ $\alpha = 96.34^\circ$ $b = 6.627 \text{ \AA}$ $\beta = 103.82^\circ$ $c = 6.998 \text{ \AA}$ $\gamma = 88.32^\circ$
Dicalcium phosphate dihydrate ( Brushite ) $\text{CaHPO}_4 \cdot 2\text{H}_2\text{O}$	1.00	Monoclinic, 1a $a = 5.812 \text{ \AA}$ $\alpha = 116.42^\circ$ $b = 15.180 \text{ \AA}$ $c = 6.239 \text{ \AA}$
Octacalcium phosphate $\text{Ca}_8\text{H}_2(\text{PO}_4)_6 \cdot 5\text{H}_2\text{O}$	1.33	Triclinic, P1 $a = 19.692 \text{ \AA}$ $\alpha = 90.15^\circ$ $b = 9.523 \text{ \AA}$ $\beta = 92.54^\circ$ $c = 6.835 \text{ \AA}$ $\gamma = 108.65^\circ$
$\alpha$ -tricalcium phosphate $\alpha\text{-Ca}_3(\text{PO}_4)_2$	1.50	Monoclinic, P21/a $a = 12.887 \text{ \AA}$ $\alpha = 126.20^\circ$ $b = 27.280 \text{ \AA}$ $c = 15.219 \text{ \AA}$
$\beta$ -tricalcium phosphate $\beta\text{-Ca}_3(\text{PO}_4)_2$	1.50	Rombohedral, R3c $a = b = 10.439 \text{ \AA}$ $c = 37.375 \text{ \AA}$
Hydroxyapatite $\text{Ca}_{10}(\text{PO}_4)_6\text{OH}_2$	1.67	Hexagonal, P63/m $a = b = 9.421 \text{ \AA}$ $c = 6.884 \text{ \AA}$
Hydroxyapatite, Calcium deficient $\text{Ca}_{10-x}(\text{PO}_4)_{6-x}(\text{HPO}_4)_x\text{OH}_{2-x}$	1.50 - 1.67	Hexagonal, P63/m $a = b = 9.421 \text{ \AA}$ $c = 6.884 \text{ \AA}$
amorphous Calcium phosphate $\text{Ca}_x\text{H}_y(\text{PO}_4)_z \cdot n\text{H}_2\text{O}$	-	-

*Tab. 2 – Summary description of Calcium phosphates characterized by a Calcium to Phosphor molar ratio comprised between 1 and 2*

Among the reported crystalline phases, octacalcium phosphate, tricalcium phosphate ( $\alpha$  and  $\beta$ ), Hydroxyapatite and the amorphous calcium phosphate are particularly suitable for biomedical application. These Calcium phosphates are similar to biogenic calcified tissue components, so they are not recognized as foreign material in the body and can integrate into living tissues by bone-remodeling processes.

#### **1.4.1- CALCIUM PHOSPHATES IN BIOMEDICAL APPLICATIONS**

The main usages of calcium phosphates in biomedicine are:

- Hard tissue engineering

As a consequence of traumatic events, invasive therapies, degenerative diseases, a loss of structural hard tissues may happen. Fast replacement of this tissue can accelerate healing while providing an increase in patients ease. Characteristics of an ideal bone replacement are: biocompatibility, bioreabsorbibility, osteogenesis and osteoconduction capability obtained by optimal cell colonization, and obviously mechanical strength. Biomaterials science extensively studied Calcium phosphate base materials as bone filler or bone substituent. Many techniques have been developed to produce solid materials containing micro and macro porosity ( useful for cell colonization ) , void structures, 3D architectures, in order to constantly improve body response to their appliance. Nanomaterial science applied to hard tissue engineering introduced relevant improvements. Due to the similar dimensions with respect to the inorganic components of calcified tissues and to the enhanced surface reactivity, nanosized calcium phosphates reveal: better osteoconduction/ osteoinduction properties, enhanced interaction with organic materials, better sinterability and mechanical properties [F. Chen, et al., 2012].

- Drug/gene delivery

After implantologic surgery, any pathological situation ( infection, inflammations, etc ) unfavorably affects the performance of the implant in terms of healing and resorption process. To avoid these phenomena, implanted biomaterials may be “charged” with drugs, acting as carriers responsible of local drug release. Calcium phosphate biomaterials have been

promisingly studied as drug delivery systems, both as drugs releasing bone substituents and drug carrier nano-micro particles [E. Verron, et al., 2010; F. Chen, et al., 2012]. In particular, Hydroxyapatite is capable to bound a variety of molecules and most therapeutic agents under physiological conditions [N.Roveri, et al., 2010]. E. Verron, et al., 2010, reported that Hydroxyapatite bone cements revealed promising issues in local delivery of drugs characterized by low efficiency of systemic administration. Hormones, growth factor, bone morphogenic protein and antibiotics characterized by short half-time have been successfully administered by Calcium phosphates bone substituent, while bisphosphonate drugs can be strongly adsorbed on Calcium phosphates carriers [P. Pascaud et al., 2014]. In general, local drug delivery could reduce side effects and improve the efficacy of existing drugs. By adjusting the properties and the morphology of the carrier, addressing and rate of drug release may be controlled by various mechanisms.

Hydroxyapatite, provides a surface chemistry that facilitates adsorption of organic compounds (i.e. proteins ) as well as charged inorganic particles [R. K. Singh, et al., 2013]. K. Wang et al, 2012, investigated the adsorption mechanism of proteins on bioceramics, suggesting the relevant parameters affecting these phenomena. For an example, it was found that large molecules near their isoelectric point adsorb readily, because of the wider variety of disposed charges capable to match with surface Calcium and phosphates ions. It have also been demonstrated [I.S. Harding, et al., 2005] that HA faster accumulates positive charge below the point of zero charge than it accumulates negative charge above it. In this work focused on the adsorption/desorption processes the authors reported that in many conditions phosphate groups will predominate at the HA surface. On this basis mechanism for surface adsorption has been proposed to be deprotonation of surface  $\text{HPO}_4^{2-}$  sites and subsequent adsorption of cations to the lattice surface site ( if cation is Calcium, lattice growth occurs ). [N. Lyczko, et al., 2014], also, proposed and reported a study on the capability of Hydroxyapatite to link, retain and sequester heavy metals from aqueous media, for environmental purposes.

## 1.5- AIM OF THE THESIS

Inorganic nano and micro particles retrieved along years large interest, and abundance of literature is nowadays available investigating their potentiality in many fields. The control and tuning of their properties, joined with their intrinsic behavior allow to obtain versatile, stable, efficient technological materials. Relying on already well known properties of inorganic materials, the aim of this thesis is to synthesize specific inorganic nano and micro particles and to develop and optimize working applications involving their use. In particular this research work has been focused on Titanium dioxide and Calcium phosphate materials. Such materials are purposely synthesized with the aim of showing effectiveness in desired application. Particular attention is given to the surface properties and particle dimensions. The focal point and main challenge of this work is to retrieve relevant performances while strongly looking for the high simplicity, environmental low impact and economical affordability of the synthesis and application. The syntheses have been designed and performed in non-toxic and non-hazardous solvents and the use of heavy metals or reaction additives, such as surfactants, stabilizers, capping agents have been avoided or limited. Moreover, the used reaction conditions were as much as possible mild and safe, as proposed by the “green chemistry” principles. Also the design and development of applications and prototypes must take into account the environmental impact, working simplicity and economical affordability.

In particular, environmental and energetic fields applications are reported for photocatalytic Titanium dioxide nanoparticles. Optimizing the parameters for an efficient and massive radical generation process, Titanium dioxide nanoparticles have been applied in gaseous pollutant abatement. Subsequent prototypes have been built and tested with the aim of reduce the emissions of a working plant. In addition, photoactive Titanium dioxide have been deposited on photovoltaic panels with the purpose of exploit their self-cleaning properties in order to enhance their efficiency.

By pointing on adsorption capabilities, synthesized sub-micrometric Calcium phosphates showing high surface area have been tested as drug carriers in two different applications. Hydroxyapatite nanoparticles have been used, dispersed into their own mother solution to avoid aggregation phenomena induced by drying, to prepare an injectable suspension for local anticancer drugs delivery. Hydroxyapatite nanoparticles and Brushite microparticles have also

been proposed and tested for an innovative use as agricultural drug carriers for phytotherapies delivery, similarly to biomedical applications. Nowadays in fact, Calcium phosphates are used in agriculture only as phosphor containing fertilizers.

## 2- EXPERIMENTAL SECTION

### 2.1- PHOTOACTIVE TITANIUM DIOXIDE

#### 2.1.1- TITANIUM DIOXIDE SOL-GEL SYNTHESIS ( *Synthesis 1* )

The photoactive Titanium dioxide have been obtained by hydrolysis/polycondensation of an alkyl-oxo Titanate in aqueous solution under controlled conditions; Isopropyl alcohol have been added as stabilizing and capping agent in order to control the hydrolysis and crystal growth rate. Titanium (IV) isopropoxide have been chosen as Titanium (IV) source and 0.3 mol of this reagent have been dissolved in 300 ml of Isopropyl alcohol in a well dried flask and stored capped. At the same time 900 ml of distilled water are heated to 80°C in a three-necked flask. The Titanium alkyl-oxide isopropanol solution is now transferred into a dropping funnel and slowly added dropwise to the aqueous media under vigorous stirring. To avoid the uncontrolled reaction of Titanium isopropoxide with water vapor on the dripper tip causing the formation of solid aggregates and irregular flow, a mild air soufflé is directed to the droplets line. The reaction occurs immediately, forming a white suspension of Titanium dioxide nanoparticles in the water phase. After the dropping the reaction is maintained at 80°C under stirring for 3 hours. Part of the hydro-alcoholic suspension is now centrifuged at 7000 rpm for 10 minutes, the precipitate is collected and dried at 70°C for 4 hours, then finely crushed in a mortar. The synthesis have been performed again by varying the alkyl-oxo-Titanate concentration ( 1/10 proposed molar amount ) in order to affect the average size of crystallites aggregates in suspension.

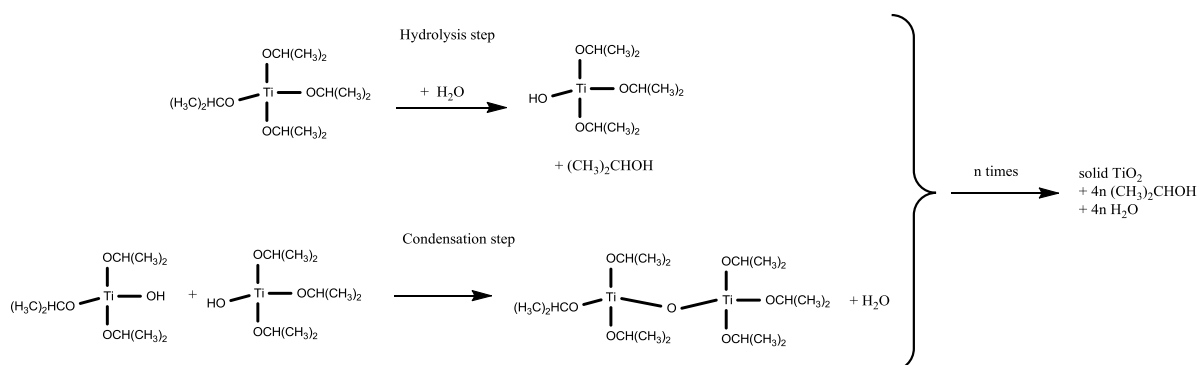


Fig. 6 – Reaction scheme of Titanium (IV) isopropoxide hydrolysis/polycondensation reaction leading to Titanium dioxide formation

Reagents:

- $\text{Ti}[\text{OCH}(\text{CH}_3)_2]_4$ , Sigma Aldrich, reagent grade, pur. 98%
- $(\text{CH}_3)_2\text{CH}_2\text{OH}$ , Sigma Aldrich, pur. >99%,

#### **2.1.1.1- TITANIUM DIOXIDE THERMAL TREATMENT**

Dry solid Titanium dioxide powder have been finely grounded in a mortar and heat treated to increase crystallinity, trying to enhance photoactivity [S. Sakka, 2005 ]. 5.0 grams of powders are placed in an Alumina crucible and heat treated for 1 hour at 420°C after a 5°C/min ramp in air atmosphere. Heat treatment performed with Thermal system TSH 17/50/300 elite limited tubular oven.

#### **2.1.1.2- TITANIUM DIOXIDE HETEROCOAGULATION ON SILICA ( *Synthesis 2* )**

To improve Titanium dioxide photocatalytic behavior by avoiding aggregative phenomena resulting in loss of active surface area, Titanium dioxide nanoparticles have been adsorbed on silica microparticles by heterocoagulation. 1.0 g of fumed silica are dispersed in 100 ml bidistilled water and kept under mild stirring in a plastic beaker. A small amount of 0.01 M ammonia solution is added to reach pH 5.00. Then, 50 ml of Titanium dioxide hydro alcoholic suspension prepared as previously described, are added dropwise and the mixture kept under slow stirring for 30 minutes. The solid phase is now filtered and washed with distilled water to remove Ammonia and excess of Titanium dioxide, and dried 10 hours at 40 °C.

Reagents:

- $\text{SiO}_2$  fumed silica, Sigma Aldrich, surf. Area 175-225  $\text{m}^2/\text{g}$ , pur. 99,8%
- $\text{NH}_4\text{OH}$ , 28-30% solution in water, Sigma Aldrich, ACS reagent grade
- $\text{TiO}_2$  suspension produced by reported *synthesis 1*

### 2.1.1.3- PHOTOACTIVITY TEST: METHYLENE BLUE SOLUTION (*Experiment 1*)

$3.13 \cdot 10^{-5}$  mol Methylene blue (3,7 bis-(dimethylammino)phenazationium chloride) are dissolved in 100 ml distilled water and the solution is stored in dark. 50 mg of Titanium dioxide powder are dispersed in 90 ml distilled water by bath sonication for 15 min, then 5 ml of the methylene blue solution are added keeping the mixture under stirring to avoid aggregation/sedimentation of titania, and finally the solution volume is adjusted to 100 ml. The mixture is placed in a dark box under vigorous magnetic stirring, and a 3 ml sample of suspension is transferred in a glass cuvette (1 cm optical path) to collect the UV-Vis spectrum at the time zero. To minimize baseline fluctuations given by light scattering the spectrum is collected in a range of 720 -540 nm and the signal is set equal to zero at  $\lambda=720$  nm for each measure. In fact, aggregated Titanium dioxide particles in suspension scatter visible light causing a slight turbidity of the solution. Moreover, the aggregation phenomena affect particle size during the measure changing the baseline value with time. After collecting the spectrum *versus* a blank of distilled water, the sampled amount is transferred back into the mixture to keep the initial volume. Inside the box, the mixture is then irradiated with a UV source (typically high pressure Hg vapor lamp,  $\lambda=365$  nm, 25 W) placed at 15 cm distance to the suspension surface still under stirring. The sampling procedure is repeated and spectra are collected at various time intervals until 180 minutes. The described setup allows to work easily with simple equipment, and producing reproducible data characterized by good signal to noise ratio within the absorbance linearity range of the analyte in reasonable times. In order to identify the most performing commercially available light source, this test have been repeated using a 365 nm high pressure Hg lamp, a 254 nm low pressure Hg lamp and a set of 365 nm LED; the data obtained have been compared and the effective emission spectra of this sources recorded and related to the results.

Reagents:

- Methylene blue (3,7 bis-(dimethylammino)phenazationium chloride), Sigma Aldrich, pur. >97%
- TiO<sub>2</sub> produced by reported *synthesis 1*

Tested lamps specifications:

- High pressure Hg lamp,  $\lambda$  emission = 365 nm, power 25 Watt, UVL-225D Mineral lamp model, UVP
- Low pressure Hg lamp,  $\lambda$  emission = 254 nm, power 25 Watt, UVL-225D Mineral lamp model, UVP
- LED system,  $\lambda$  emission = 365 nm, composed by 160 LEDs for a total 22.6 Watt, purposely built by DELLED

## **2.1.2- NO<sub>x</sub> PHOTOCATALYZED ABATEMENT**

### **2.1.2.1- NO<sub>x</sub> PHOTOCATALYZED ABATEMENT, STATIC CONDITIONS** *(Experiment 2)*

The performances of prepared Titanium dioxide catalyst in photocatalytic degradation of gaseous nitrous oxides ( NO and NO<sub>2</sub> mixture, commonly indicated as NO<sub>x</sub> ) have been at first tested in static conditions. A sealed glass box of the approximate volume of 8 liters have been equipped with a 9 Watt low pressure Hg vapor lamp (  $\lambda=254$  nm, UV ) and a NO<sub>x</sub> portable analyzer ( CROWCON GAS-PRO IR 452164/03-001 equipped with IR detector ). Pictures of experimental apparatus are reported in *Fig.7*.



*Fig. 7 – Pictures of experimental apparatus used for static NO<sub>x</sub> photocatalyzed abatement tests*

At first the chamber have been filled with NO<sub>x</sub> certified solution to the final concentration of approximately 50 ppm ( total NO<sub>x</sub> ), but some air have been allowed to remain inside. The NO<sub>x</sub> concentration have been monitored for 90 minutes to evaluate the spontaneous equilibration reaction between the two nitrous oxide species and the environmental oxygen, and to avoid the presence of gas loss in the system as well.

Due to the fact that NO<sub>x</sub> gaseous solution used for the reported tests is mainly composed of the mono oxidized specie NO, oxidation reaction spontaneously occurs when mixed with environmental oxygen. Equilibrium conditions between NO, O<sub>2</sub> and forming NO<sub>2</sub> are reached within 60 minutes, as visible in *Fig. 8*, after that the analytes concentrations can be considered constants. Following this results, each subsequent test is performed after an equilibration delay of 60 minutes, in order to cut off this phenomena from affecting catalysis data measurement.

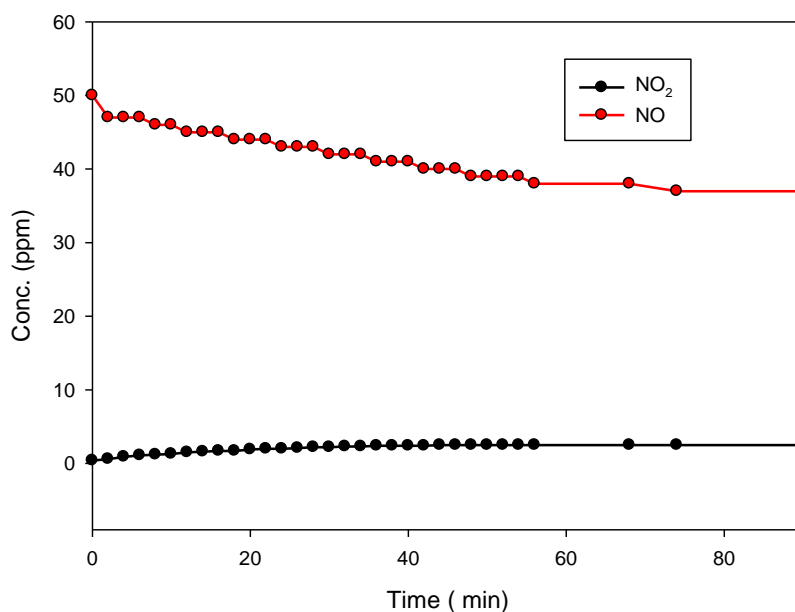


Fig. 8 – Concentration variations of NO and NO<sub>2</sub> within a sealed chamber, in absence of UV irradiation or catalyst due to equilibration of NO, O<sub>2</sub> and forming NO<sub>2</sub>.

In order to separate and evaluate the single role of different mechanism contributing to NO<sub>x</sub> scavenging from the system, the UV induced photolysis have been measured. The test chamber have been filled with NO<sub>x</sub> certified solution to an approximate final concentration of 50 ppm ( total NO<sub>x</sub> ), leaving some air inside. The system have been sealed and left 60 minutes in absence of light to allow NO and NO<sub>2</sub> to reach the equilibrium concentrations. After that the UV source is turned on in absence of any catalyst and the NO<sub>x</sub> concentrations is monitored for 45 minutes. The data obtained are normalized and reported as percentage value, and referred as the blank for all subsequent tests involving catalysts.

A stainless steel net basket ( 8 cm length, 3.5 cm diameter, 45 μm mash holes ) is added to the chamber setup surrounding the UV lamp to act as catalyst support ( estimated disposable surface 60 cm<sup>2</sup>). The basket have been previously carefully cleaned by sonication in acetone and washed with water, dried and soaked in the Titanium dioxide suspension obtained via sol-gel synthesis, previously described ( *Synthesis I*). After drying, the soaking is repeated for a better covering up of the surface. No adhesive or linker is added to the suspension and the catalyst particles are weakly grabbed to the metal surface, but the adhesion is sufficient to avoid material loss by shaking. Approximately 12 mg of active Titanium dioxide are anchored to the support.

The test chamber so prepared have been filled with NO<sub>x</sub> certified solution to the approximate final concentration of 25 ppm ( total NO<sub>x</sub> ), leaving some air inside. The system have been sealed and left 60 minutes in absence of light to allow NO and NO<sub>2</sub> to reach the equilibrium concentrations. Then, the UV source is turned on and the NO<sub>x</sub> concentrations is monitored for 120 minutes.

Reagents:

- NO<sub>x</sub> certified solution (gas mix from SIAD, NO = 80.0 ± 1.7 ppmvol, NO<sub>2</sub> = 0.8 ppmvol, in Nitrogen)
- TiO<sub>2</sub> suspension produced by *synthesis*

#### **2.1.2.1.1- SILANE/SILICA SUPPORT COATING (*Synthesis 3*)**

In order to increase the catalyst adhesion on the solid support and improve the dispersion of the particles, Titanium dioxide is deposited on a silica covered substrate. The steel basket is carefully cleaned by sonication in acetone and water to remove the deposited catalyst, and dried. 67.0 ml of TEOS ( tetraethyl-oxy-silane) are placed in a 200 ml flask under mild stirring and heated to 35°C. 19.0 ml TMCS ( trimethyl-chloro-silane) are added and left mixing for 10 minutes. After that 37.5 ml of Isopropyl alcohol are added and left reaching the correct temperature. Meanwhile, 7.5 ml of Ammonia ( 30% solution in water ) are added to 22.5 ml isopropyl alcohol, transferred into a dropping funnel, and added dropwise to the silane mixture. The formation of a white mist, due to the gas-phase reaction between NH<sub>3</sub> and HCl formed by TMCS hydrolysis, and a white precipitate inside the flask can be observed. After the dropping the reaction is kept 5 hours at 35-40°C under mild stirring, then the white precipitate is filtered, the liquid phase is collected and taken up to 150 ml volume with isopropyl alcohol. The steel basket is now quickly soaked in the alcoholic silane mixture, excessive liquid is removed by shaking and finally gently sprinkled with fumed silica dust. The basket is then left aging for 72 hours at room temperature. After aging, silica dust in excess is removed by a air blow and the silica-coated steel basket is soaked in the Titanium dioxide hydro-alcoholic suspension obtained via sol-gel synthesis 1. After drying, the soaking is repeated to improve the covering up of the surface. The coated basket is then mounted in the test chamber filled with NO<sub>x</sub> certified

solution to reach the approximate final concentration of 25 ppm ( total NO<sub>x</sub> ), leaving some air inside. The system have been sealed and left 60 minutes in absence of light to allow NO and NO<sub>2</sub> to reach equilibrium concentrations. After that the UVC source is turned on and the NO<sub>x</sub> concentrations is monitored for 120 minutes.

Reagents:

- Si(OC<sub>2</sub>H<sub>5</sub>)<sub>4</sub>, Sigma Aldrich, reagent grade, pur. 98%
- (CH<sub>3</sub>)<sub>3</sub>SiCl, Sigma Aldrich, reagent grade, pur. >98%
- NH<sub>4</sub>OH, 28-30% solution in water, Sigma Aldrich, ACS reagent grade
- (CH<sub>3</sub>)<sub>2</sub>CH<sub>2</sub>OH, Sigma Aldrich, pur. >99%,
- SiO<sub>2</sub> fumed silica, Sigma Aldrich, surf. Area 175-225 m<sup>2</sup>/g, pur. 99,8%
- NO<sub>x</sub> certified solution (gas mix from SIAD, NO = 80.0 ± 1.7 ppmvol, NO<sub>2</sub> = 0.8 ppmvol, in Nitrogen)
- TiO<sub>2</sub> suspension produced by *synthesis 1*

#### **2.1.2.2- NO<sub>x</sub> PHOTOCATALYZED ABATEMENT, FLUXING CONDITIONS** **(Experiment 3)**

To approach the real conditions in which the photocatalytic system have to work, some degradation tests on fluxing gas have been carried out. A scale model of the real scrubbing tower have been purposely built in PVC plastic, and added of an electric powered fan to simulate the effective pressure and flow. Within the inner cavity of the drainpipe ( 100 cm length x 13 cm diameter ) a photocatalytic system is mounted according to the most effective setup identified by previous static tests. The tube have been lined interiorly with 40 mm thick glass fiber wool previously coated with Titanium dioxide ( by spraying nearly 500 ml of prepared hydro-alcoholic titanium dioxide suspension). When dried, a UV source is fitted in the

remaining cavity; the source consisted in two in-line mounted low pressure Hg lamp, emission  $\lambda = 254 \text{ nm}$ , 30 W total power ( technical datasheet reported in *Fig. 9*). In order to increase as possible the catalytic surface, empty spaces of the tube have been filled with Titanium dioxide coated silica glass pieces, recovered from scraps ( approximate average size 20x30x5 mm). The so prepared catalytic tube is mounted on the scale-model prototype, and flow tests have been carried out with air to evaluate the working conditions and to avoid obstructing phenomena; by calculations the estimated flow is 8.5-10 m<sup>3</sup>/hour, and the travelling time of gaseous species trough the catalyst 5 to 7 seconds.

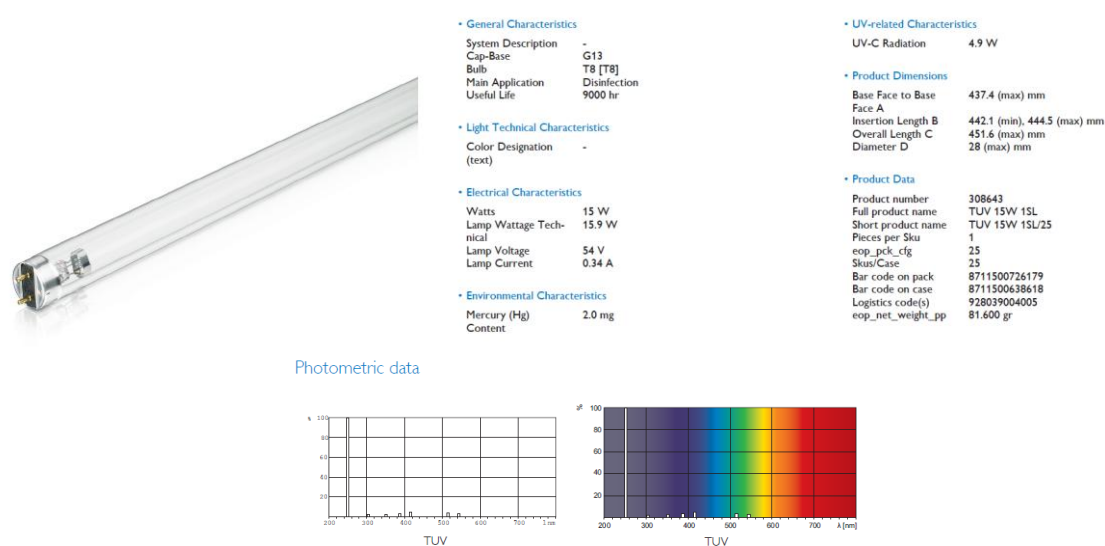


*Fig. 9 – Technical datasheet of low pressure Hg lamp used in tests and prototypes construction*

The prototype is tested to measure its effective capability of reduce the NO<sub>x</sub> concentration of a flowing by gas mixture. An NO<sub>x</sub> real time analyzer (CROWCON GAS-PRO IR 452164/03-001 equipped with IR detector) is applied to the prototype exhaust pipe ( after the fan) and a Nitrous oxide certified solution is blown into the input pipe. Because of the input pipe diameter ( 130 mm) and the strong suction, a relevant amount of environmental air is drawn and mixed to the NO<sub>x</sub> solution, making possible to obtain an exit top concentration of 14 ppm, only. A set of tests have been performed by repeatedly turning on and off the UV source while the gas mixture is flowing by the prototype and collecting data about the exit NO<sub>x</sub> concentration variations related to time.

Reagents:

- NO<sub>x</sub> certified solution (gas mix from SIAD, NO = 80.0 ± 1.7 ppmvol, NO<sub>2</sub> = 0.8 ppmvol, in Nitrogen)
- TiO<sub>2</sub> suspension produced by reported *synthesis 1*

### **2.1.2.3- NO<sub>x</sub> PHOTOCATALYZED ABATEMENT, FLUXING CONDITIONS** **(Experiment 4)**

Because of the gas mix cylinder's scarce capacity and low concentration, it appears difficult to obtain reproducible data; during the tests in fact NO<sub>x</sub> concentration tended to decrease and after only five set of test the NO<sub>x</sub> mixture pressure was over. Furthermore the concentrations value reached and gas composition was not truly representative of the effective output of the plant process on which the photocatalytic process have to be applied. The prototype have so been modified and directly connected to the plant's exhaust chimney. Instead of loading the photocatalytic system in the narrow aspiration tube, the full width of the prototype's central body is used; the internal exchange plastic bodies have been removed and at its place a sort of filtering layout is prepared by fitting three floors of stainless steel net perpendicular to the gas flow. A new type of catalyst is prepared and deposed on the net supports to a thickness of nearly 25 mm each floor. The catalyst consisted of scrap glass pieces taken from the glass recycling spinneret for negligible costs; the silica glass particle are nearly same size and shape (cube 4x4x4 mm), without sharp edges, showing an average weight of 0.158 g each. By simple calculations an average surface area of 6330 cm<sup>3</sup> per kilograms is shown by this low cost, chemically inert support. Residual impurity (mostly metal pieces) are removed and the glass substrate is carefully washed with water and with an ammonia solution( pH 10); meanwhile 5 ml of concentrated HCl solution ( 38% w/v) are added to 5 liters of Titanium dioxide hydro-alcoholic suspension. The acidified Titania suspension is now spray-applied to the still wet glass pieces, previously spreaded on polypropylene sheets. After 24 hours drying glasses are collected

and mildly washed with water to remove excessive catalyst and ammonium chloride; 50 kg of glass supported catalyst were prepared, but approximately only half have been used in the prototype. The UV source has been improved as well, by increasing the total system power from 30 to 100 Watts disposing three lamps ( one each floor) parallel to the catalyst surface ( about 150 mm above this) and a fourth lamp perpendicular to these, crossing all the catalyst floors. The modified prototype was connected to the plant's exhaust chimney, the fan turned on and the effective gas mix produced by anodizing process let flow by. Gas analysis was performed by a portable multi gas analyzer (LAND, LANCOM 4) capable of measuring eight different gas-phase analytes by electrochemical cells, including NO<sub>x</sub>. Placed the sampling probe at the prototype exhaust, a "white " measurement have been carried out , showing the effective NO<sub>x</sub> emission profile along time related to a single plant process cycle. The UV source was then switched on and the measurement repeated, obtaining real data about NO<sub>x</sub> knocking down capability of photocatalytic prototype. Unfortunately the effective exhaust gas shown high corrosive features, quickly damaging the hand made electric wiring of UV lamps; for this reason was only possible just to turn on one of three displaced lamps, working with 30 Watts power, before a complete breakdown of electrical circuit. Furthermore the electric powered fan turned out to be undersized to overcome the intense sucking power of the plant's chimney, leading to a low gas flow rate into the prototype. Nevertheless it was possible to obtain promising data on the photocatalyzed reaction on the real gas mixture.

Reagents:

- NH<sub>4</sub>OH, 28-30% solution in water, Sigma Aldrich, ACS reagent grade
- HCl, fuming >38% solution in water, Sigma Aldrich, ACS reagent grade
- TiO<sub>2</sub> suspension produced by *synthesis 1*

#### **2.1.2.4- NO<sub>x</sub> PHOTOCATALYZED ABATEMENT, FLUXING CONDITIONS** *(Experiment 5)*

In order to get closer to a pilot plant configuration, a new improved prototype was built enhancing catalyst displacement, UV irradiation and flow. A 300 mm diameter PVC tower was built and 20 catalytic floor have been made inside by glass fiber net, each one was charged with approximately 600 g of Titanium dioxide coated glass pieces disposed on the net support. Every catalytic floor was spaced 100 mm, and in the middle two compact UV lamp (9 watt, low pressure Hg vapor, emission  $\lambda = 254$  nm) were placed. A most powerful fan was applied to the setup and the electrical wiring was completely related to the outside of flow tunnel; the assembled prototype resulting in a 2.2 meters catalytic tower was connected to the plant's exhaust chimney, the fan turned on and the effective gas mix produced by anodizing process let flow by. Pictures of the complete prototype and particulars of the catalytic floor are reported in *Fig.10*.

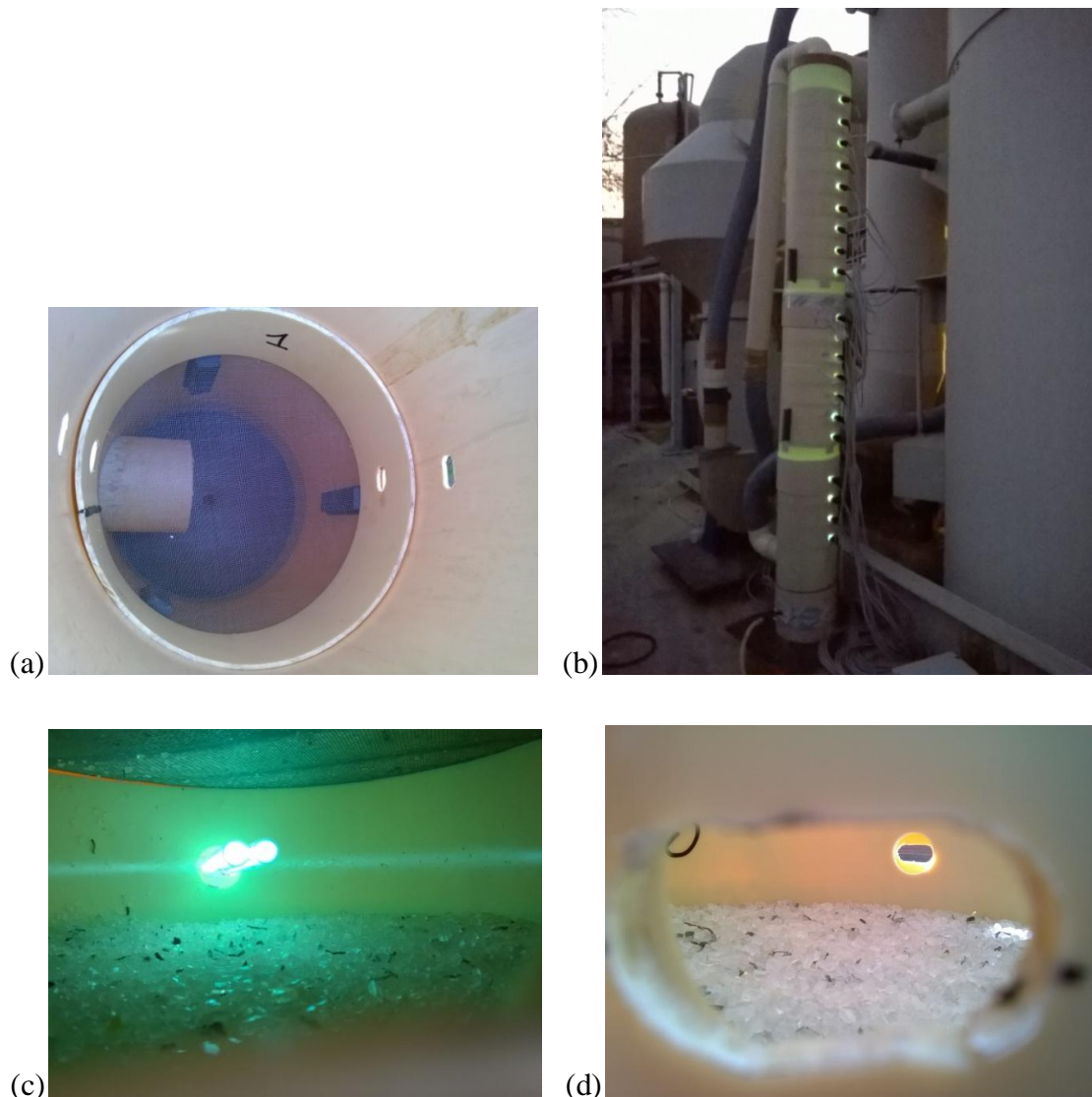


*Fig. 10 – Pictures of the complete prototype (b); particulars of catalytic floors without catalyst (a), loaded with catalyst (d) and UV irradiated (c)*

After a purging time required by the huge amount of condensation liquid drained by the prototype from the plant's chimney, a first set of tests have been carried out: the outgoing gases from the prototype have been sampled and analyzed following the official methods reported in "estensione del decreto ministeriale 25-08-2000 all.4 comma 2 D.M. 12-07-1990". A bubbler is charged with 30 ml of 0.025 M Potassium permanganate and 1.25 M Sodium hydroxide solution and connected to the prototype tower and the gas is sampled to a flow speed of 0,5 liters/min for 30 minutes. A "white" sample is collected with UV lights turned off, then the sampling procedure is repeated three times turning on: 10 UV lamps active on 10 catalytic

floors, 20 UV lamps active on 20 catalytic floors, and 30 UV lamps on 20 catalytic floors. It is relevant to mention that during each sampling time, four production cycle are performed in the plant, producing peaks of emission considerably stronger than the average. The sampled solutions have been analyzed by ionic chromatography ( Metrohm XXR basic IC plus 883 with supp 5 anion column, carbonate suppressor cartridge, calibrated with Absolute standard Anion mix#2 certified solution) and the nitrate concentration reported to the sampled gas volume. After the bubbler sampling analysis, a second set of tests have been performed by a portable multigas analyzer (LAND, LANCOM 4, 8 channel analyzer with electrochemical detectors) in order to drawing up the emission profile of NO<sub>x</sub> concentration in time, related to a single production cycle of the plant, and evaluate the abatement performed by the prototype in different setups. Sampling is recorded by reading NO<sub>x</sub> value every 10 seconds for 7 minutes after the productive cycle has began. A “white “ sample is collected with UV lights turned off, then the sampling procedure is repeated three times turning on: 10 UV lamps active on 10 catalytic floors, 20 UV lamps active on 10 catalytic floors and 30 UV lamps on 20 catalytic floors, respectively.

Reagents:

- KMnO<sub>4</sub>, Sigma Aldrich, ACS reagent grade, pur. >99,0%
- NaOH, Sigma Aldrich, ACS reagent grade, pur. >97%
- TiO<sub>2</sub> suspension produced by *synthesis 1*

### **2.1.3- PHOTOVOLTAIC PANELS COATING ( *Experiment 6* )**

A stabilized hydro-alcoholic suspension of titanium Dioxide have been developed to increase efficiency of solar light conversion made by Silicon photovoltaic panels. Even if synthesis and precise formulation couldn't be clearly reported for property reasons, photoactive Titanium dioxide active principle is obtained by previously reported sol-gel synthesis, based on Titanium isopropoxide hydrolysis controlled by isopropyl alcohol in the double role of co-solvent and capping agent for the growing crystal nuclei.

Testing of effective energy production enhancement have been performed with real on field application on a photovoltaic plant. Testing site have been chosen following at least two criteria:

easy access to the panels, i.e. a ground installed plant and a suffering due to pollution fouling which causes a certain loss of transmittance from the external glass covered with environmental carbonic matter and a subsequent decrease in efficiency of the plant. The selected plant was a power plant producing near 1 MegaWatt sited near Ferrara. Four strings composed by 23 panels each have been selected as test bench. Two couple of strings (composed by a treated string and a reference one, each) have been tested under different conditions: one couple have been washed before the treatment, while on the other couple application have been performed directly on dirty panels. Have to be mentioned that treated string of each couple have been purposely chosen because of its lower performances compared to the respective reference. The stabilized suspension have been applied by simple spraying on dry panels surface, to an average amount of 6 ml suspension per square meter. An electric pump vaporizer have been modified for this purpose by applying a small diameter (50  $\mu\text{m}$ ) nozzle. At this point the hourly amount of power produced by each string have been monitored for one year, and particularly the ratio between treated vs the untreated string of each couple.

## **2.2- CALCIUM PHOSPHATES NANO-MICRO PARTICLES**

### **2.2.1- SYNTHESIS OF CALCIUM PHOSPHATES**

#### **2.2.1.1- HYDROXYAPATITE SYNTHESIS (*Synthesis 4*)**

Hydroxyapatite nanocrystalline particles have been prepared by neutralization reaction in aqueous media. In a 2 liters flask, a suspension containing 1.35 mol of Calcium hydroxide in 1000 ml of distilled water is prepared and kept under mechanical stirring to avoid sedimentation; then the suspension is cooled down to 5°C in a ice bath. Meanwhile, 0.756 mol of phosphoric acid are dissolved in 550 ml of distilled water and the solution is transferred into a dropping funnel. The phosphoric acid solution is slowly added dropwise to the hydroxide suspension under nitrogen flux. The overall reaction is exothermic, and the dripping have to be settled in order to avoid temperature to raise. The reaction mixture is now allowed to reach room temperature and kept under stirring 6 hours without cooling; the product is filtered, washed with distilled water and dried in oven at 80°C for 5 h.

Reagents:

- $\text{Ca}(\text{OH})_2$ , Riedel de Haen, pur. >96 %
- $\text{H}_3\text{PO}_4$ , Sigma Aldrich, 85% v/v aqueous solution

### 2.2.1.2- BRUSHITE SYNTHESIS (*Synthesis 5*)

To obtain a Brushite particles suspension a metathesis reaction between Calcium acetate and diammonium phosphate has been performed in pH controlled aqueous solution.

0.02 mol of Calcium acetate are dissolved in 50 ml distilled water and added dropwise to a solution containing 0,01 mol dibasic ammonium phosphate and 0,01 mol Phosphoric acid in 150 ml distilled water under stirring at room temperature. The calcium phosphate phase immediately forms giving a white precipitate, and after 30 min the reaction is complete reaching pH 5.0; the product is filtered, washed with distilled water and dried in oven at 80°C for 5 h.

Reagents:

- $\text{Ca}(\text{CH}_3\text{COO})_2$ , Riedel de Haen, pur. 99,0 +/- 0,5 %
- $(\text{NH}_4)_2\text{HPO}_4$ , Riedel de Haen, pur. >99%
- $\text{H}_3\text{PO}_4$ , Sigma Aldrich, 85% v/v aqueous solution

To evaluate the role of concentration the procedure has been repeated by increasing 10 times the concentration of reagents: 0.06 mol of Calcium acetate are dissolved in 20 ml distilled water and slowly dropped in a 20 ml water solution containing 0.05 mol dibasic ammonium phosphate and 0.01 mol phosphoric acid kept under stirring at RT. After 30 min a white slurry suspension is obtained, the product is filtered, washed with water and dried at 80°C.

Reagents:

- $\text{Ca}(\text{CH}_3\text{COO})_2$ , Riedel de Haen, pur. 99,0 +/- 0,5 %
- $(\text{NH}_4)_2\text{HPO}_4$ , Riedel de Haen, pur. >99%
- $\text{H}_3\text{PO}_4$ , Sigma Aldrich, 85% v/v aqueous solution

### 2.2.1.3- BRUSHITE SYNTHESIS (*Synthesis 6*)

Differently from the previous synthesis the acidic phosphate solution is added to the basic Calcium solution controlling the temperature in order to affect the growth rate of the forming crystalline phase. A suspension containing 0.01 mol Calcium acetate and 0.03 mol Calcium hydroxide in 100 ml distilled water is prepared and cooled to 5°C in ice bath under mechanical stirring; a solution of 0.025 mol of dibasic ammonium phosphate and 0.015 mol phosphoric acid in 100 ml distilled water is slowly added dropwise. After 30 min the reaction pH reach 8.5, the precipitate is filtered, washed with distilled water and dried in oven at 80°C for 5 hours.

Reagents:

- $\text{Ca}(\text{CH}_3\text{COO})_2$ , Riedel de Haen, pur. 99,0 +/- 0,5 %
- $\text{Ca}(\text{OH})_2$ , Riedel de Haen, pur. >96 %
- $(\text{NH}_4)_2\text{HPO}_4$ , Riedel de Haen, pur. >99%
- $\text{H}_3\text{PO}_4$ , Sigma Aldrich, 85% v/v aqueous solution

#### 2.2.1.4- BRUSHITE SYNTHESIS (*Synthesis 7*)

In this synthesis, the crystallization of Brushite phase is forced even if Hydroxyapatite formation should be favoured by the pH range of the reaction mixture, by adding Magnesium in 1/3 molar ratio in respect to Calcium. The  $Mg^{++}$  ion is known to compete for  $Ca^{++}$  sites in apatitic structure, and at high concentrations, this process destabilizes the growing apatitic phase, promoting the precipitation of Brushite. 0.15 mol of Calcium hydroxide and 0.05 mol Magnesium chloride are dissolved in 80 ml distilled water; the solution is heated to 40°C under stirring and 100 ml of 1.3 M phosphoric acid solution are slowly added dropwise. A white precipitate is quickly obtained, and after 30 min the product is filtered, washed with distilled water and dried at 80°C for 5h.

Reagents:

- $Ca(OH)_2$ , Riedel de Haen, pur. >96 %
- $MgCl_2$ , anhydrous, Sigma Aldrich, pur. >98%
- $H_3PO_4$ , Sigma Aldrich, 85% v/v aqueous solution

#### 2.2.1.5- BRUSHITE SYNTHESIS (*Synthesis 8*)

In order to reduce the size of forming Brushite particles without adding capping agents to the reaction mixture, *synthesis 5* have been modified with some easily manageable expedients: 0.01 mol of Calcium acetate are dissolved in a mixture of 20 ml distilled water and 5 ml ethanol. A solution composed of  $5 \cdot 10^{-3}$  mol dibasic ammonium phosphate and  $5 \cdot 10^{-3}$  mol phosphoric acid in 20 ml water is prepared. Both solutions are stored capped in a refrigerator to cool down to 5°C. When the correct temperature is reached, the acidic phosphate solution is put under vigorous stirring by a turbo-emulsifier device, and the Calcium acetate solution is quickly added to perform a massive immediate reaction. The mixture is kept under turbo mixing for 15 minutes, than the product is filtered, washed with distilled water and dried at 80°C for 6 hours.

Reagents:

- $\text{Ca}(\text{CH}_3\text{COO})_2$ , Riedel de Haen, pur. 99,0 +/- 0,5 %
- $\text{CH}_3\text{CH}_2\text{OH}$ , Sigma Aldrich, ACS grade 96%
- $(\text{NH}_4)_2\text{HPO}_4$ , Riedel de Haen, pur. >99%
- $\text{H}_3\text{PO}_4$ , Sigma Aldrich, 85% v/v aqueous solution

#### **2.2.1.6- BRUSHITE SYNTHESIS (*Synthesis 9*)**

The synthesis of Brushite crystals from marble samples have been performed by treating Carrara marble powders with phosphate containing solutions: 1.0 g of Carrara marble powder placed in a Petri dish is covered with a solution containing 0.01 mol of dibasic ammonium phosphate and  $1.5 \cdot 10^{-3}$  mol of Magnesium carbonate in 20 ml distilled water. Slowly, Ammonia evolution is observed and the solution pH moves from 8 to 9; after 24 hours the powders are filtered and dried. Moreover, a second marble powder sample have been similarly treated with a solution containing 0.01 mol Potassium dihydrogen phosphate in 20 ml distilled water. Within 24 hours the pH value of the solution moves from 4.5 to 7.1. The white powders are filtered and dried.

Reagents:

- $(\text{NH}_4)_2\text{HPO}_4$ , Riedel de Haen, pur. >99%
- $\text{MgCO}_3$ , Sigma Aldrich, pur. >98%
- Carrara marble powder, unknown purity
- $\text{KH}_2\text{PO}_4$ , Riedel de Haen, pur. >99,5%

### 2.2.1.7- MONETITE SYNTHESIS (*Synthesis 10*)

Sub-micrometric monetite crystals have been obtained by the same reaction described in *Synthesis 5*, but changing the reaction environment. A suspension containing 0.01 mol dibasic ammonium phosphate and 0.01 mol phosphoric acid in 150 ml ethanol is prepared and cooled down to 5°C in a ice bath. When the correct temperature is reached a solution containing 0.02 mol Calcium acetate in 50 ml distilled water is added dropwise keeping under mechanical stirring. By adding the aqueous phase, the still solid ammonium phosphate is slowly dissolved and the white calcium phosphate product is formed. The precipitate is filtered, washed with distilled water and dried at 80°C for 6 hours.

#### Reagents:

- $\text{Ca}(\text{CH}_3\text{COO})_2$ , Riedel de Haen, pur. 99,0 +/- 0,5 %
- $\text{CH}_3\text{CH}_2\text{OH}$ , Sigma Aldrich, ACS grade 96%
- $(\text{NH}_4)_2\text{HPO}_4$ , Riedel de Haen, pur. >99%
- $\text{H}_3\text{PO}_4$ , Sigma Aldrich, 85% v/v aqueous solution

### 2.2.1.8- MONETITE SYNTHESIS (*Synthesis 11*)

0.02 mol of Calcium acetate are dissolved in 50 ml distilled water and added dropwise to 150 ml ethanol solution containing 0.02 mol Phosphoric acid under stirring at room temperature. The calcium phosphate phase immediately forms giving a white precipitate, and after 30 min the reaction is complete reaching pH 3.0; the product is filtered, washed with distilled water and dried in oven at 80°C for 5 h.

#### Reagents:

- $\text{Ca}(\text{CH}_3\text{COO})_2$ , Riedel de Haen, pur. 99,0 +/- 0,5 %
- $\text{CH}_3\text{CH}_2\text{OH}$ , Sigma Aldrich, ACS grade 96%

- $\text{H}_3\text{PO}_4$ , Sigma Aldrich, 85% v/v aqueous solution

#### **2.2.1.9- MONETITE SYNTHESIS (*Synthesis 12*)**

0.01 mol of Calcium nitrate tetrahydrate are dissolved in 25 ml ethanol and added dropwise to a solution of 0.01 mol phosphoric acid in 75 ml ethanol under stirring. The precipitate is filtered, washed with distilled water and dried at 80°C.

Reagents:

- $\text{Ca}(\text{NO}_3)_2 \cdot 4 \text{H}_2\text{O}$ , Sigma Aldrich, ACS grade, pur. 98%
- $\text{CH}_3\text{CH}_2\text{OH}$ , Sigma Aldrich, ACS grade 96%
- $\text{H}_3\text{PO}_4$ , Sigma Aldrich, 85% v/v aqueous solution

#### **2.2.1.10- $\beta$ -TRICALCIUM PHOSPHATE SYNTHESIS (*Synthesis 13*)**

To obtain  $\beta$ -Tricalcium phosphate powders, Calcium carbonate and dihydrate Calcium hydrogen phosphate (Brushite) in molar ratio 1:2, respectively, are finely mixed in a mortar. The powder mix is transferred in a Alumina crucible and heated to 950°C for 6 hours in air. Heat treatment is performed with Thermal system TSH 17/50/300 elite limited tubular oven.

Reagents:

- $\text{CaCO}_3$ , Sigma Aldrich, pur. >99,0%
- $\text{CaHPO}_4 \cdot 2 \text{H}_2\text{O}$  (Brushite), obtained by *synthesis 8*

### 2.2.1.11- $\beta$ -TRICALCIUM PHOSPHATE SYNTHESIS (*Synthesis 14*)

Magnesium doped  $\beta$ -Tricalcium phosphate have been synthesized by a thermal treatment of Calcium and Magnesium sources with a calcium phosphate precursor.  $1.0 \cdot 10^{-2}$  mol dihydrate Calcium hydrogen phosphate (Brushite) are finely mixed in a mortar with  $4.5 \cdot 10^{-3}$  mol Calcium carbonate and  $5.0 \cdot 10^{-4}$  mol Magnesium carbonate (1:0.45:0.05 molar ratio); the powder mix is transferred in a Alumina crucible and heated to 950°C for 6 hours in air. Heat treatment is performed with Thermal system TSH 17/50/300 elite limited tubular oven.

Reagents:

- $\text{CaCO}_3$ , Sigma Aldrich, pur. >99,0%
- $\text{MgCO}_3$ , Sigma Aldrich, pur. >98%
- $\text{CaHPO}_4 \cdot 2 \text{H}_2\text{O}$  (Brushite), obtained by *synthesis 8*

### 2.2.1.12- BIOMIMETIC POROUS SCAFFOLD SYNTHESIS

(*Synthesis 15*)

A porous scaffold mainly composed of magnesium doped  $\beta$ -Tricalcium phosphate and hydroxyapatite have been obtained via thermal treatment of pristine marine sponge (*Euspongia officinalis* Adriatica, also known as fine dama). The sample have been cut to reach the desired shape ( approximately  $10 \text{ cm}^3$  volume) and immersed in a Tricalcium phosphate aqueous suspension (1.5 g Mg doped Tricalcium phosphate in 15 ml distilled water, 0.25 ml dodecyl alcohol, sonicated 5 min). By soaking several times the sponge's micropores have been completely filled with the suspension, and the so prepared sample have been placed in an Alumina crucible and thermally treated at 800°C for 4 hours in air atmosphere. Heat treatment is performed with Thermal system TSH 17/50/300 elite limited tubular oven.

Reagents:

- $\text{Ca}_{2,91}\text{Mg}_{0,09}(\text{PO}_4)_2$ , obtained by *synthesis 14*
- $\text{CH}_3(\text{CH}_2)_{11}\text{OH}$ , Sigma Aldrich, pur. >98%

### 2.2.1.13- BIOMIMETIC POROUS SCAFFOLD SYNTHESIS (*Synthesis 16*)

Another porous scaffold composed of magnesium doped  $\beta$ -Tricalcium phosphate and hydroxyapatite have been obtained by *in situ* solid state reaction of Calcium and Magnesium sources with a calcium phosphate precursor. A marine sponge sample (*Euspongia officinalis* Adriatica, also known as fine dama) have been cut to reach the desired shape ( approximately 10  $\text{cm}^3$  volume). A suspension containing  $1.0 \cdot 10^{-2}$  mol dihydrate Calcium hydrogen phosphate (Brushite),  $4.5 \cdot 10^{-3}$  mol Calcium carbonate and  $5.0 \cdot 10^{-4}$  mol Magnesium carbonate (1:0.45:0.05 molar ratio) in 18 ml distilled water and 2 ml Triethanolamine have been prepared and sonicated in a bath 5 minutes. The sponge sample is repeatedly soaked until the micropores have been completely filled with the suspension; the sample is then placed in an Alumina crucible and thermally treated at 920°C for 6 hours in air. Heat treatment is performed with Thermal system TSH 17/50/300 elite limited tubular oven.

Reagents:

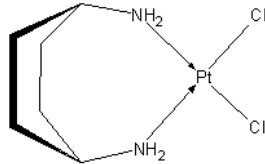
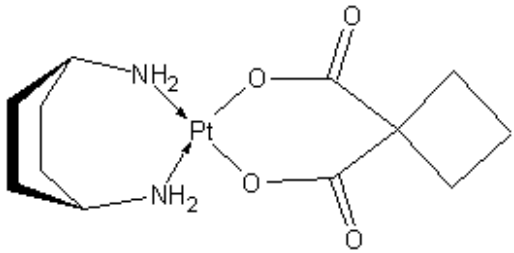
- $\text{CaCO}_3$ , Sigma Aldrich, pur. >99,0%
- $\text{MgCO}_3$ , Sigma Aldrich, pur. >98%
- $\text{CaHPO}_4 \cdot 2 \text{H}_2\text{O}$  (Brushite), obtained by *synthesis 8*
- $(\text{HOCH}_2\text{CH}_2)_3\text{N}$ , Sigma Aldrich, pur. > 98%

## 2.2.2- CALCIUM PHOSPHATES FOR BIOMEDICAL DRUG DELIVERY

### 2.2.2.1- ANTICANCER Pt COMPLEX PHYSISORPTION ON HYDROXYAPATITE

#### (*Synthesis 17*)

To obtain physical adsorption of anticancer drugs onto Calcium phosphate substrate, Hydroxyapatite nanocrystals have been chosen. Two different square-planar Platinum complexes, based on modifications of already known *Oxaliplatin* anticancer, have been prepared and provided by the group of Prof. G. Natile at the Department of Chemistry, University of Bari [N. Margiotta et al., 2012]. Complexes brief description reported in *Tab. 3*.

<p><u>EP230 (Kiteplatin)</u></p> <p>[PtCl<sub>2</sub>(<i>cis</i>-1,4-DACH)]</p> <p>C<sub>6</sub>H<sub>14</sub>Cl<sub>2</sub>N<sub>2</sub>Pt</p> <p>MW=380,17 u</p> <p>Water solubility ≈ 2 mg/ml</p>	
<p><u>SMF30</u></p> <p>[Pt(1,1-CBDCA)(<i>cis</i>-1,4-DACH)]</p> <p>C<sub>12</sub>H<sub>20</sub>N<sub>2</sub>O<sub>4</sub>Pt</p> <p>MW=451,38 u</p> <p>Water solubility ≈ 1 mg/ml</p>	

*Tab. 3 – Anticancer Platinum complexes description*

50 ml of suspension containing 1 % w/v of hydroxyapatite particles in phosphate buffer solution at pH 7.2 are prepared and kept under stirring at room temperature. 100 mg of [PtCl<sub>2</sub>(*cis*-1,4-DACH)] (EP230 , *Kiteplatin*) are added and kept under mild stirring. At increasing time interval, 500 µl of suspension are collected in a vial, centrifuged at 14000 rpm

for 5 minutes. A volume of 300  $\mu$ l of supernatant solution is diluted to 4.5 ml volume with bidistilled water and acidified with 500  $\mu$ l of 69 % v/v HNO<sub>3</sub> solution. Drug adsorption have been monitored by ICP-OES analysis following the free Platinum content of sampled solutions until a plateau is reached at 360 minutes. After 20 hours stirring, the suspension have been filtered and the solid phase carefully dried at 37°C for 12 hours. Drug charged Hydroxyapatite particles are analyzed by SEM imaging with EDS probe in order to reveal Platinum presence on the surface and evaluate morphology and dimensions of aggregates.

Reagents:

- Phosphate buffer solution pH 7.2 +/-0.2, Sigma Aldrich, for Microbiology
- [PtCl<sub>2</sub>(cis-1,4-DACH)], produced by synthesis
- Ca<sub>10</sub>(PO<sub>4</sub>)<sub>6</sub>OH<sub>2</sub>, produced by *synthesis 4*
- HNO<sub>3</sub>, Sigma Aldrich, 69.0 % v/v solution, Ultrapure, trace metal analysis grade

#### **2.2.2.2- ANTICANCER Pt COMPLEX PHYSISORPTION ON HYDROXYAPATITE (*Synthesis 18*)**

100 ml of suspension containing 1 % w/v of Hydroxyapatite particles in phosphate buffer solution at pH 7.2 are prepared and kept under stirring at room temperature. 100 mg of [Pt(1,1-CBDCA)(cis-1,4-DACH)] (SMF30) are added and kept under mild stirring. At increasing time interval, 500  $\mu$ l of suspension are collected in a vial, centrifuged at 14000 rpm for 5 minutes. A volume of 300  $\mu$ l of supernatant solution is diluted to 4.5 ml volume with bidistilled water and acidified with 500  $\mu$ l of 69 % v/v HNO<sub>3</sub> solution. Drug adsorption have been monitored by ICP-OES analysis following the free Platinum content of sampled solutions until a plateau is reached at 360 minutes. After 20 hours stirring, the suspension have been filtered and the solid phase carefully dried at 37°C for 12 hours. Drug charged Hydroxyapatite particles are analyzed by SEM imaging with EDS probe in order to reveal Platinum presence on the surface and evaluate morphology and dimensions of aggregates.

Reagents:

- Phosphate buffer solution pH 7.2 +/-0.2, Sigma Aldrich, for Microbiology
- [Pt(1,1-CBDCA)(cis-1,4-DACH)], produced by synthesis
- Ca<sub>10</sub>(PO<sub>4</sub>)<sub>6</sub>OH<sub>2</sub>, produced by *synthesis 4*
- HNO<sub>3</sub>, Sigma Aldrich, 69.0 % v/v solution, Ultrapure, trace metal analysis grade

### **2.2.2.3- ANTICANCER Pt COMPLEXES RELEASE FROM HYDROXYAPATITE** **(Experiment 7)**

Four Citrate buffer solutions ( pH 4.00- 4.65- 5.00 -5.50) are prepared and 80 mg of Platinum complex charged hydroxyapatite are dispersed by bath sonication in 10 ml of each one. At established time intervals up to 360 minutes, 500 µl of suspension are collected in a vial, centrifuged at 14000 rpm for 5 minutes. A volume of 300 µl of supernatant solution is diluted to 4.5 ml volume with bidistilled water and acidified with 500 µl of 69 % v/v HNO<sub>3</sub> solution. Drug release is monitored by ICP-OES analysis following the free Platinum content of sampled solutions. The procedure is repeated for both two drugs charged Hydroxyapatite.

Reagents:

- Citrate buffer solution ( pH 4.00- 4.65- 5.00 -5.50), Fluka, HPCE grade
- HNO<sub>3</sub>, Sigma Aldrich, 69.0 % v/v solution, Ultrapure, trace metal analysis grade

## 2.2.3- CALCIUM PHOSPHATES FOR PHYTOTHERAPICAL DRUG DELIVERY

### 2.2.3.1- COPPER SULFATE PHYSISORPTION ON HYDROXYAPATITE

(*Synthesis 19*)

22.3 g ( $8.9 \cdot 10^{-2}$  mol) of solid Copper sulfate pentahydrate are grounded in a mortar and slowly added (approximately 2 g each time, waiting until dissolution) to 100 ml water suspension containing 6.7 % w/w nanocrystalline Hydroxyapatite (as obtained by synthesis 4) under moderate stirring. An opaque light blue suspension is obtained, quite stable to sedimentation, containing Copper ions in approximately 5 % w/w.

Reagents:

- $\text{CuSO}_4 \cdot 5 \text{H}_2\text{O}$ , Sigma Aldrich, reagent grade, pur. > 98,0 %
- $\text{Ca}_{10}(\text{PO}_4)_6\text{OH}_2$ , produced by *synthesis 4*

### 2.2.3.2- SULFUR PHYSISORPTION ON BRUSHITE (*Synthesis 20*)

46.0 g of wettable Sulfur powder (colloidal) are slowly added to 100 ml water suspension containing 8 % w/w microcrystalline Brushite (as obtained by synthesis 8) under vigorous stirring. A brownish dense and viscous homogeneous suspension is obtained containing approximately 40 % w/w Sulfur.

Reagents:

- Sulfur powder, Brenntag, pur. 95 %
- $\text{CaHPO}_4 \cdot 2 \text{H}_2\text{O}$  (Brushite), water suspension, obtained by *synthesis 8*

### 2.2.3.3- PHYTOTHERAPIC DRUGS DELIVERY TEST (*Experiment 8*)

The obtained suspensions have been tested with in field tests. After synthesizing an appropriate amount of previously described suspension, three test have been planned in order to evaluate their effectiveness as phytotherapeutic treatments in comparison with commercially available products.

- First test regarded Copper sulfate suspension application in treatment of *Downy mildew* plant illness: four hectares of grapevine cultivation affected by *Downy mildew* (*Peronospora* disease ) have been subject to four different treatment. One hectare have been treated by spray applying 5.0 liters of suspension ( opportunely diluted ) six times within a month. One hectare have been treated by spray applying 5.0 liters of suspension (opportunely diluted) nine times within a month. One hectare have been treated by spray applying a commercial product for *Peronospora* abatement ( based on Copper sulfate itself ) nine times within a month, following recommended dosage. One hectare have been not treated as a reference.
- Second test regarded Sulfur suspension application in treatment of *Powdery mildew* plant illness: three hectares of grapevine cultivation affected by *Powdery mildew*(*Oidio*) have been subject to three different treatment. One hectare have been treated by spray applying 2.5 liters of suspension ( opportunely diluted ) seven times within a month. One hectare have been treated by spray applying a commercial product for *Powdery mildew* treatment ( based on Sulfur itself ) seven times within a month, following recommended dosage. One hectare have been not treated as a reference.
- Third test regarded Copper sulfate suspension application in treatment of *Kiwi Psa* (*Pseudomonas Syringae actinidiae*) plant illness: three hectares of Kiwi cultivation affected by *Kiwi Psa* have been subject to three different treatment. One hectare have been treated by spray applying 1.0 liter of suspension ( opportunely diluted ) six times within a month. One hectare have been treated by spray applying a commercial product for *Kiwi Psa* treatment ( based on Copper sulfate itself ) six times within a month, following recommended dosage. One hectare have been not treated as a reference.

After one month treatment as described, effectiveness have been evaluated by carefully inspecting leaves, bunches and floral buttons. For each part are reported percentage values of incidence ( percentage of affected parts ) and severity ( percentage of coverage by symptoms ). Aim for this experiment is to provide a stabilization and controlled release of phytotherapeutic elements, reducing their atmospheric leaching.

## **2.3- CHEMICAL-PHYSICAL CHARACTERIZATION TECHNIQUES**

### **2.3.1- SCANNING ELECTRON MICROSCOPY IMAGING**

Scanning electron microscopy ( SEM ) have been developed to overcome a physical limit of optical microscopy, known as diffraction limit, which allows to obtain resolved image only to a theoretical value of 200 nm, but limiting in practical the imaging to the micrometric scale. By investigating a sample surface with a shorter wavelength radiation than visible light, it is possible to obtain resolved image of smaller objects. For this reason in scanning electron microscopy technique, an electron beam, accelerated to energy in the KeV scale and producing wavelength of picometers is used to obtain resolved images of sub-micrometric objects.

A scanning electron microscope is schematically constituted by the following elements:

- A column address, where the electron beam is generated and accelerated
- A series of electromagnetic lenses to guide the electron beam
- A vacuum chamber where samples can be scanned by the electron beam
- Detectors of various typology, acquiring signals from the interaction between electron beam and the sample
- An algorithm capable of reconstructing an image from the detectors signals

Within the column address, kept under vacuum, electrons are produced by thermionic effect from a Tungsten filament cathode heated to high temperature and accelerated to energy ranging from hundreds to tens of thousands eV ( commonly from 200 eV up to 40 KeV ) by applying a potential difference. A series of electromagnetic lenses and slit converge and focus the beam on a little window overlooking on the sample chamber. To perform the scan of the sample's surface a series of coils deflect alternately the beam to explore the selected area and a last lens focus the beam and provide optical defects corrections. The incident electron beam interact at this point with the sample; as the electrons penetrate trough the surface, a portion of their energy is lost and re-emitted by the sample in different manners. Detectors records various forms of emissions, used to recreate an image or provide structural/compositional information. The sample have to be conductive or needs to be previously coated with a ultra thin layer of

conductive material (gold or graphite) to prevent localized charging phenomena resulting in loss of information and imaging capability. Except for this requirement, any non-fluidic or volatile sample can be analyzed. Penetration of electrons through the sample's surface determine the volume of the sample, called volume of interaction and given by the depth of penetrated matter and a delimited area (little more extended than the beam diameter) producing the signals. The size and shape of the volume of interaction both depends on beam parameters and sample's composition, and often determine a resolution limit. Within the volume of interaction, incident electrons collide with nuclei and electron clouds of the sample following two principal mechanism: elastic and inelastic scattering. As a result of this kind of interactions a wide variety of signals are produced:

- Secondary electrons
- Backscattered electrons
- Transmitted electrons
- Absorbed electrons
- Auger electrons
- Hole-electron pairs generation
- X-ray emission
- UV to IR electromagnetic emission

The most common setup of SEM's detector equipment provides for signals arising from secondary electrons and backscattered electrons. In particular, accurate three-dimensional imaging of sample surface is obtained by secondary electrons analysis; this kind of radiation is originated by inelastic scattering phenomena, producing low energy electrons ( $< 50$  eV) with little penetration capability. For this reason the signal collected is related to the most superficial portion of the interaction volume ( few nm ) and is strongly dependent from the surface morphology. On this basis a high resolution grey scale image, with shades and three dimensional appearance is reconstructed. Backscattered electrons are conversely characterized by higher energy than secondary electrons, as a function of the incident beam. They are obtained from elastic scattering up to few micrometers in depth on the sample scanned region,

and directly related to the atomic average weight of the crossed matter. For this reason the obtained black and white image represents a chemical composition map of the analyzed region, in which the contrast emphasizes high average atomic weight areas with brighter tones, and lower atomic average weight areas in darker, providing useful structural and compositional information, spatially defined within the investigated area. Fascinating sample characterization are possible by coupling this two kind of electronic imaging. Commonly, last generation SEM instruments are also equipped with X-Ray detectors, to perform EDS analysis ( Energy Dispersive X-Ray Spectroscopy ). Incident electron beam can reach energies high enough to remove electrons from the internal shells of colliding atoms from the sample, higher shell electrons falls in energy to fill the electronic hole, and dispersed energy is emitted in form of X-ray radiations. Since each atom possess different energy spacing between internal levels, it is possible to recognize atomic species by analyzing the X-Ray emission spectra generated instantly from the sample. By relating emission peaks to typical K emission of elements, and previously calibrating to the relative intensity of each peak, it is possible to obtain a semi-quantitative analysis of the interaction volume at the same time as a morphological imaging. Also, by performing a scanning motion of the beam on a wider surface of the sample, and collecting cumulating data, an elemental map of the inspected region is formed, providing compositional/ constitutional analysis coupled with a precise distribution image of each element within the inspected region. In this work SEM image and EDS analysis are performed with a Carl Zeiss SEM EVO MA 10 equipped with Oxford microanalysis EDS probe.



*Fig. 11 – Picture of Carl Zeiss SEM EVO MA 10*

### 2.3.2- TRANSMISSION ELECTRON MICROSCOPY IMAGING

Transmission electron microscopy ( TEM ) is an imaging technique capable of providing resolved images and structural information of very small objects. Like in scanning electron microscopes, an accelerated electrons beam is used to investigate the sample, in order to overcome resolution limit imposed by optical microscopes. The main difference with SEM instrument is that in TEM technique transmitting electrons passing through the sample are collected to generate the image. This involve higher energy electron beams are required ( typically 100-300 KeV ) and a different geometry, with the detectors placed under the sample holder. After the sample crossing, transmitted electrons beam is diverged, enlarged and focused by subsequent magnetic lenses in order to increase resolution power, and finally collected by the detector. By this setup is possible to reach resolution in the order of 0.2 nm. Information are obtained from the sample by analyzing exiting electron waves, both by their intensity, amplitude and phase. By acting on electromagnetic lenses many operating modes are possible to produce contrast formation, leading to different kind of information retrieved from sample analysis:

- Bright field imaging
- Diffraction contrast
- Electron energy loss
- Phase contrast
- Diffraction

The most common operating mode is bright field imaging, where contrast image is formed simply by sample electron absorption. Thicker parts of sample, or regions composed by higher atomic number matter, appear darker, providing a simple two dimensional projection of the sample. More sophisticate operating mode allows to focus on crystalline structures, highlighting defects or determine sample's elemental composition. In this work TEM image are obtained with a Philips CM 100 instrument working at 80 kV voltage.

### 2.3.3- X-RAY POWDER DIFFRACTION

Soon after the X-Ray radiation discovery in the early twentieth century, theories on single crystal diffraction was developed to explain the observed phenomena of diffraction patterns generation from irradiated crystal lattices. Different approaches permitted scientist such as Laue (1912), Ewald (1913) and Bragg( 1915-1935) to explain the phenomenon, contributing to build the modern theory of crystal X-Ray diffraction. The complete theoretical treatment is quite complex and lengthy, but in a simplified description it could be related to the physics of light diffraction from grids. In both phenomena there are some requirements to observe diffraction: a translational periodicity in the space of the diffracting elements ( which is also a requirement to define a crystalline material ) and similarity between the diffracting elements spacing and the incident radiation wavelength. Therefore, an electromagnetic radiation with wavelength in the same magnitude order of atomic distances in crystal lattices is needed. Monochromatic X-Ray colliding on a crystalline atomic lattice will be elastically reflected by each crystalline plane, according to Bragg's law:

$$2 d_{hkl} \sin\Theta = n \lambda$$

Where:

$d_{hkl}$  is spacing between crystal planes,  $\Theta$  is the radiation incidence angle and  $\lambda$  is the radiation wavelength; for  $n$  integer values, radiations reflected by planes are in phase and a diffraction spot is observed.

The real phenomena is more complex to rationalize, but with mathematical operation ( appealing inverse Fourier transform and recurring to reciprocal lattice) it is possible to determine the effective electron density in a crystal by its generated diffraction pattern. In powder diffraction techniques, crystal structure resolution is made also more complex by having Avogadro numbers of diffracting lattices, randomly arranged and oriented in a macroscopic volume interacting with the incident X radiation. It provokes the observation of concentric diffraction cones ( Laue's cones) instead of spots arranged in patterns. Anyway several techniques have been developed to obtain information from powder diffraction: structural determination can be challenged by simulated annealing and charge flipping, known material

crystalline structure can be refined by Rietveld simulation, crystallites average size can be approximated by Sherrer's formula:

$$D = K \lambda / \beta_{1/2} \cos \Theta$$

Where D, the average size of crystallites is approximated by relating to  $\lambda$ , the incident wavelength, the line broadening at half the maximum intensity,  $\beta_{1/2}$ , the angle of diffraction,  $\Theta$ , and corrected by a dimensionless shape factor K, ranging from 0.7 to 1.7 and depending on shape of crystallites and hkl reflecting planes ( usually a value of 0.9 is assumed in case of unknown crystal shape).

Multiphase determination can be performed by matching experimental diffraction profile with spectra contained in a database and semiquantitative analysis can be performed easily by RIR (relative intensity ratio) comparison with an internal standard by peak area integration ( less accurate than Rietveld multiphase refinement, but quite fast and easy to perform).

#### Operating procedure

Finely grounded crystalline material is softly pressed in a slide specimen holder ( usually built to eliminate background scattering or peaks) and placed in axis of a goniometric system providing the correct geometry of the system. The most common instrumental configuration consist of a fixed sample holder placed between an X-Ray generator and a detector, both applied on swinging arms (Bragg-Brentano geometry). X-Ray are generated by striking a metal anode (usually Copper) with accelerated electrons that colliding with metal atoms extract inner shell electrons and the energy of outer shells electron falling in the lower levels, is emitted as X-radiation with characteristic spectra ( for each element ) composed of peaks (  $K\alpha$ ,  $K\beta$ , ..) and a background (Bremsstrahlung radiation). Outcoming radiation is filtered to select only the wavelength of K emission and to cut the background, converged, collimated and directed to the sample. The diffraction pattern generated is collected by a detector ( scintillation or CCD ) by moving the goniometric arms in order to vary the radiation incidence angle. The obtained spectra reports intensity of diffraction peaks vs  $2\Theta$  ° ( twice incidence angle). Data reported in this work are obtained by a Panalytical Xpert diffractometer equipped with Xcelerator detector and a Bruker D8 Advance diffractometer equipped with Linxeye detector, both working with Copper generators providing X-rays with a wavelength ( $\lambda$ ) of 1.5406 Å.

### 2.3.4- DINAMIC LIGHT SCATTERING SIZE DETERMINATION

This easy performable technique allows to determine the size distribution profile of small particle in suspension by analyzing the physical scattering of an electromagnetic radiation crossing a volume section of the liquid suspension. When a radiation hit suspended particles small enough compared to the incident wavelength, Rayleigh scattering is observed in all directions. Since the particles in suspension undergo Brownian motion, spatial position and distance of scatterers vary constantly, provoking little fluctuations in the scattering intensity over the time. By irradiating a sample with monochromatic and coherent radiation, as LASER radiation, it is possible to resolve and analyze temporal fluctuations in scattering intensity by means of a photon auto-correlation function. Different mathematical approach can be applied to gain information from the time resolved data, but the simplest is to treat the first order function as a single exponential decay. Several parameters practically influences the goodness of data acquisition and mathematical treatment: multiple scattering, polydispersity or anisotropy of the sample, electrostatic interactions between particles or double layer formation can affect the measure, which is by itself an approximation ( particles in suspension are considered spherical ). Anyway the technique can easily and quickly provide plausible size determination and distribution values, which can be precise and accurate in optimized experimental conditions.

#### Operating procedure

A suspension is obtained by finely dispersing a known solid sample in a liquid by sonication to reach a strongly diluted but still slightly turbid scattering sample. To stabilize suspension and avoid aggregation/flocculation or sedimentation phenomena, solvent mixture or surfactants can be used, but with the severe limitation given by the fact that refractive index and density of the liquid phase should be known ( tables are available reporting data and applicability of a range of recommended solvent mixtures ). Approximately 1.5 ml of suspension is placed in a transparent cuvette, giving attention not to form bubbles or voids, capped and placed in the instruments. After a thermal stabilization time, optimizing operations ( like positioning of incident beam or photomultiplier gain) are performed by the instrument itself in order to obtain good quality data; if quality criteria are not satisfactory, it is appropriate to change sample preparation by varying dilution and/or solvent. Once measurement begins an Infrared polarized LASER beam is directed trough the sample and scattering time fluctuations are collected by a photodetector

placed at 90° to the incident beam after another polarizer ( other geometries are also used). Measure is repeated several times to obtain cumulative data. Size distribution data are generated accompanied by PDI (polydispersity index) and quality evaluation parameters to better define calculated values. Data presented in this work have been collected with Malvern ZEN 3600 nano-sizer instrument.

### 2.3.5- SURFACE AREA DETERMINATION (BET)

Surface area determination is based on the application of the Brunauer-Emmett-Teller theoretical extension to Langmuir's adsorption model. Langmuir explained the adsorption of ideal gas molecules on an adsorbent solid surface in isothermal conditions, by assuming the formation of a continuous monolayer of adsorbate on the solid surface. The Brunauer-Emmett-Teller theory evolved from this hypothesis, by considering the possibility of a multilayered adsorption occurring on solid surfaces. The focus points of the theory are: 1) The physical adsorption of gas on solid occurs infinitely in multiple layers; 2) there is no interaction between gas molecule layers, so the completion of a layer before the formation of a second one is not necessary; 3) the Langmuir's theoretical treatment can be applied to each layer. The Brunauer-Emmett-Teller theory can be formalized by the following formula:

$$\frac{1}{v[(p_0/p) - 1]} = \frac{c - 1}{v_m c} \left( \frac{p}{p_0} \right) + \frac{1}{v_m c},$$

Where:

v = adsorbed gas amount ( volume units)

p = equilibrium pressure

p<sub>0</sub> = saturation pressure

v<sub>m</sub> = monolayer adsorbed gas amount ( volume units)

c = BET constant, containing physical parameters like heat of adsorption for the monolayer

The reported adsorption isotherm can be linearly plotted as  $1/v[(p_0/p)-1]$  vs  $p/p_0$ . The obtained value of slope (A) and intercept on y axes (I) can be used to calculate  $v_m$ , relating to the total surface area as reported:

$$v_m = 1/(A + I)$$

$$\text{Total surface area} = (v_m N_a S) / V$$

Where:

$N_a$  is Avogadro's number,  $V$  is the gas molar volume,  $S$  is the adsorption cross section of adsorbing solid

#### Operating procedure

A little amount of solid sample is weighed and placed in a quartz cell. Once connected to the instrument's degas station, vacuum is gently applied inside the cell (to avoid powder material suction inside the vacuum line) and the whole system heated up to 180-200 °C by slow step to completely remove gaseous species adsorbed on the sample surface. After this preparation procedure the sample is weighed again in the sealed cell (accurate tare has to be performed) and then connected to the instrument measure station and kept under vacuum. The cell is now cooled at 77°K by immersing in liquid Nitrogen and the analysis performed automatically by the instrument, measuring the pressure micro variations obtained in response to the subsequent injection of a defined gaseous (Nitrogen) volume. The instrument works in the linearity range of  $p/p_0$  value, ranging from 0.05 to 0.35. Data reported in this work have been obtained with Quantachrome NOVA 4200 instrument.

### 2.3.6- UV-VISIBLE SPECTROSCOPY

UV-Visible spectrophotometry is a technique based on the phenomena of electromagnetic radiation absorption by molecules. Different kinds of physical interaction can occur between radiations and molecular matter, primarily depending on the wavelength of incident electromagnetic radiation, leading to phenomena from vibro-rotational thermal excitement to ionization or bond cleavage. In particular UV-Visible spectrophotometry refers to the visible and ultraviolet portion of electromagnetic spectrum, ranging from 800 nm to 200 nm wavelength. Photons characterized by this wavelength and related energy value can be absorbed by molecules producing energy transitions between the outer electrons and leading to excited electronic states. Due to the energy requirement in rules determining the effectiveness of an electronic transition,  $\pi$ -electrons are commonly involved in this kind of phenomena. In fact, their electron density is located outside the axes between nuclei and lies at higher level than  $\sigma$  electrons in the energy diagram ( *Fig. 12* ), often taking part to the HOMO and LUMO configuration. Real absorption spectra deviates from this description , in fact wide articulate absorption bands are observed instead of lines corresponding to transition energies; this is due to the dense vibro-rotational progression of states accompanied to each electronic configuration. Furthermore, within solutions, solvation effects and interactions occur between densely packed molecules, resulting in almost infinite energy levels affordable, blurring sharp spectral lines into bands; this is clearly visible by comparing solution spectra to vapor phase spectra, where vibrational level transition are visible as band superimposed on the main electronic transition band.

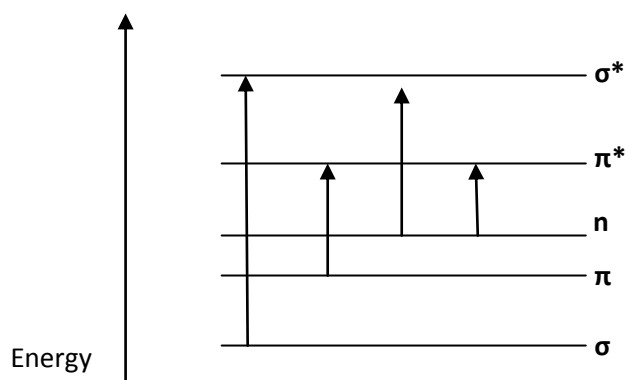


Fig. 12 – Schematization of electron transitions between molecular orbitals and relative energy scale

Transition	Wavelength of required energy
$\sigma \rightarrow \sigma^*$	110 – 135 nm
$n \rightarrow \sigma^*$ $\pi \rightarrow \pi^*$	160 – 255 nm
$n \rightarrow \pi^*$	> 285 nm

Tab. 4 – Typical wavelength associated to electron transitions

If  $\pi$  electrons conjugation occurs in molecules, electronic delocalization decreases the energy gaps moving electromagnetic absorption towards less energetic region of spectra, in the visible range. Electronic delocalization can involve the whole molecule or be located in particular groups, called chromophores, separated by fully saturated, non conjugating bonds; in this case the absorption spectrum can be considered the sum of each chromophore contribute.

The major benefits of this technique are the easy relation existing between absorption and concentration of molecules interacting with the radiation, and the mechanical and practical simplicity of the analysis.

A monochromatic radiation ( or more realistically a very narrow band of spectrum, selected by a grid coupled to a monochromator) is directed trough a sample solution with an initial intensity

( $I_0$ ). If absorption occurs, beyond the sample a decreased intensity ( $I$ ) will be read by the detector; the ratio between transmitted and incident light is defined Transmittance ( $T$ ), given by:

$$T = I / I_0$$

We also can refer to the Transmission rate ( $\%T$ ) expressed as percentage:

$$\%T = T * 100 = I / I_0 * 100$$

A value of  $\%T = 100$  indicates that the incident beam has not been weakened, so no absorption occurred, while a value of 0 refers to a complete absorption of the specific wavelength radiation by the sample. However, the amount of absorbed radiation is commonly expressed by Absorbance ( $A$ ) which is equal to the Transmittance reciprocal logarithm:

$$A = \log ( 1/T ) = \log ( I / I_0 )$$

Absorbance is easily relatable to the concentration of a light absorbing molecule in solution as expressed by the Lambert-Beer law:

$$A = \epsilon * c * d$$

Where:

$A$  = Absorbance (adimensional, a.u.)

$\epsilon$  = molar extinction coefficient (  $L \text{ mol}^{-1} \text{ cm}^{-1}$  )

$c$  = concentration (  $\text{mol l}^{-1}$  )

$d$  = optical path length ( cm )

The molar extinction coefficient is a measure of the absorbing capability of a substance, and depend on incident wavelength, solvent, pH. According to Lambert-Beer law, the absorbance of a solution is directly proportional to the molar concentration of a molecule and to the depth of solution crossed by the radiation; in practical, the proportionality is an abstraction and the linearity of signal to concentration is valid only for dilute solution ( up to absorbance value of 1 – 1.2 ); in case of more concentrate solutions experimental data deviates from law's prediction, leading to scarcely reliable analytical measurements.

## Operating procedure

A solution containing a photo absorbing molecule is placed in a quartz cuvette, commonly with a 1 cm path length, and placed in a dark sector of the spectrophotometer. Polychromatic light coming from a source is directed by mirrors on a prism or grid and splitted in its constituent wavelengths. A narrow portion of the entire spectrum is selected by a monochromator and subsequent slits, and directed to the sample. A detector ( phototube or CCD) aligned at 180° to the source ,collect the transmitting radiation and convert it in electrical signal. By moving the diffracting grid, the incident radiation wavelength is changed and a scan on the entire UV-Visible spectrum is obtained. Absorbance spectrum of the analyte is obtained by subtraction of the spectrum of blank constituted only by the sample solvent ( corrections are also needed to consider the source's emission profile, usually automatically performed by instrument's software ). Data reported in this work have been collected with Varian Cary BIO, Shimadzu UV 2600, Ocean optics USB 2000+ instruments.

### **2.3.7- INDUCTIVELY COUPLED PLASMA OPTICAL EMISSION SPECTROMETRY**

Inductively coupled plasma ( ICP ) atomic emission spectroscopy is a powerful analytical technique to determine and precisely quantify trace elements in various matrix. The instrument setup, although quite simple, is very sensitive and needs particular care of working parameter and conditions. The instrument is composed of two principal blocks: the plasma unit and an accurate spectrometer. The ICP torch consist of a set of quartz tubes surrounded by a powerful RF (radio frequency) generator in form of a coil. A strong electromagnetic field is created inside the working coil by a high intensity radio frequency ( typically working in the range 30-40 MHz) while Argon gas flows through the quartz torch at a speed of 20-50 liters per minute. To “ignite” the torch a discharge arc is created at the moment by a Tesla unit, starting the ionization process. Once started, the ionization process expands driven by the RF coil strong signal: ionized atoms repeatedly collides each other and with other gas molecule by inelastic impacts producing new ionized species and free electrons. Then, a stable high density plasma is obtained, confined by the RF coil, showing temperatures ranging from 5000 to 10000° K and electron densities of  $10^{15}$  per cubic centimeter. At this point a peristaltic pumps system provide the injection of samples into the plasma torch: water solutions ( acidified to better stabilize ions in solution) or organic liquid phase are pumped and spray vaporized into a cylindrical chamber ( cyclonic chamber) where a smooth Argon flow provides a little and constant transport of vapor into the ICP torch. Within the plasma, molecules broke up and atoms are repeatedly excited, ionized and recombined; along this processes energy is emitted by atoms as electromagnetic radiations, each element by its characteristic wavelength ( depending on different energy spacing in electronic shells). The emitted electromagnetic radiation ( ranging in the UV-Vis region ) is collected by optical paths to an extremely sensitive spectrometer; the light is separated by a diffracting grid and a monochromator which provides a bandwidth resolution in the order of  $10^{-3}$  nm, and converted to electrical signal by a detector (photodiode or CCD ). Intensity of emission to characteristic wavelength can be properly related to element concentration in injected solution, and by previous calibration line construction an accurate trace analysis can be performed, providing linearity ranges of over 6 order of magnitudes and limits of detection for analytes in the order of ppb.

## Operating procedure

Samples in various matrix can be prepared for ICP-AES analysis; a little amount of sample (depending on the analyte concentration, but enough to be representative of the whole bulk ) liquid or solid, is placed in a 50 ml falcon tube and dissolved in 5 ml ultrapure nitric acid ( 69.0 % v/v), to provide complete mineralization the tube is heated up to 85°C by a digester. The completely dissolved acidic solution is now transferred to a class A volumetric flask and diluted with bidistilled water to a desired volume (dilution is made by estimating the analyte concentration to be in the calibration range). The solution is now filtered at 0.45 µm and transferred to a Falcon tube. Once the instrument is turned on and the stable plasma is reached, blank baseline spectra and calibration line are built for different characteristic emission lines of desired elements by certified standard solutions. Commonly, the analysis is performed relying each analyte on a single emission line, but in this work quantification analysis has been based on three different characteristic lines per element, to avoid interferences and improve statistical data treatment. The sample is now injected in the cyclonic chamber and analysis performed with three repetition each line; different samples are spaced by a rinse procedure with 3 % v/v solution of ultrapure nitric acid in MilliQ water. Analysis reported in this work are performed by an HORIBA YOBIN ULTIMA 2 ICP-OES instrument.



*Fig. 13 – Picture of HORIBA YOBIN ULTIMA 2 ICP-OES instrument*

### 3- RESULTS AND DISCUSSION

#### 3.1- PHOTOACTIVE TITANIUM DIOXIDE

##### 3.1.1- TITANIUM DIOXIDE CHARACTERIZATION (*Synthesis 1*)

Titanium dioxide hydro-alcoholic suspension obtained by reported sol-gel synthesis (*Synthesis 1*) appears as a bright white opaque homogeneous liquid, quite stable to sedimentation (coagulation and phase separation appears only after 2-3 days of rest ) with a dry solid residue measured in 3 % weight. Suspension and solid phase have been characterized in order to evaluate chemical-physical parameters related to stability and photoactivity of product.

- **X-ray powder diffraction Characterization**

X-ray diffraction pattern obtained by dried  $\text{TiO}_2$  ( *Fig. 14* ) reveals peaks confirming crystalline features of the solid product.

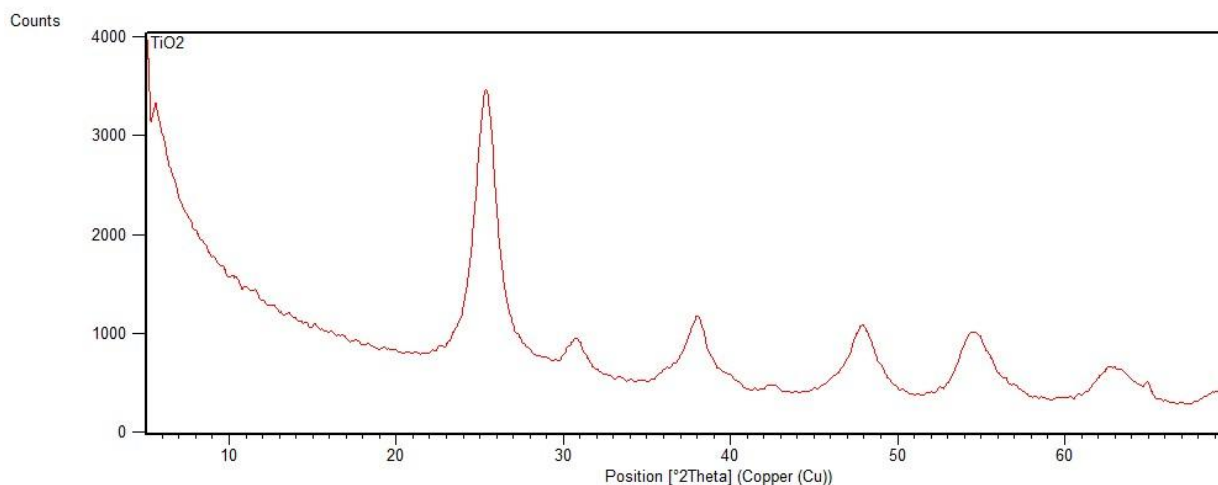


*Fig. 14 – Experimental X ray diffraction pattern of the dried product of Synthesis 1*

By comparing reflection peaks position and relative intensity to ICSD database it was possible to identify crystalline Anatase as main constituent, but residue analysis shows the presence of a secondary phase, corresponding to the polymorph Brookite. ( *Fig. 15* , reference ICSD codes: 03-065-5714 for Anatase, 01-076-1934 for Brookite).

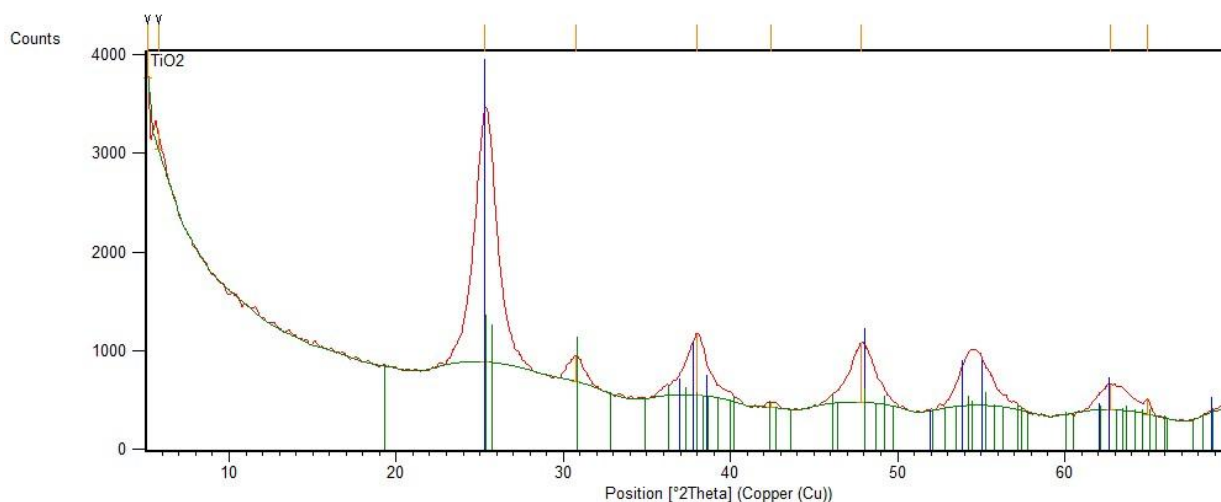


*Fig. 15 – Experimental X ray diffraction pattern of the dried product of Synthesis 1 with peak position of reference patterns*

By analyzing the integrated area values of the two phases characteristic peaks, and their ratio, opportunely scaled by reflexes relative intensity ratio, it was possible to calculate an approximate weight composition of:

Anatase = 97.7% w/w

Brookite = 2.3 % w/w

The reported percentages are obtained as average value of different synthesis, in which Brookite weight percentage oscillates between 1-3 %, but is always present. It is noticeable that all peaks appears broadened and less sharp compared to common crystalline powder diffraction pattern, possibly due to the small dimensions and/or to a low degree of order and high amount of defects of crystallites. Moreover, in the case of nanocrystalline materials, which are characterized by higher ratio of less-ordered and defective border matter to well crystalline bulk, an additional broadening of diffraction pattern can be observed. It was possible to calculate the approximate dimensions of diffracting crystallites by using the Sherrer's equation. However, this last formula can underestimate the particle size calculated value since it consider the crystallites dimensions as unique contribution to the peak broadening. The shape factor is assumed equal to 0.9 commonly used as a mean value assigned to unknown shaped crystallites.

CRYSTAL SIZE ( <i>Sherrer formula</i> )		
Wavelength Cu $K\alpha$ (Å)	1.541874	
Shape factor	0.9	
Bragg's angle ( $2\theta$ °)	25.343	
Amp. $1/2 h$ ( $2\theta$ °)	1.0029	
Crystallite size approx. (nm)		16.3

Tab. 5 – Parameters and crystal size calculation of the dried product of Synthesis 1 with Sherrer's formula

In order to evaluate the role of reactant concentrations on crystallites average size, the sol-gel synthesis (*Synthesis 1*) have been performed by decreasing to 1/10 the starting molar amount of Titanium (IV) isopropoxide. The less concentrated reaction results in similar products.

- **Scanning Electron Microscopy (SEM) morphological characterization**

Dried Titanium dioxide powders have been morphologically investigated by SEM imaging. Obtained images are reported in *Fig. 16*.

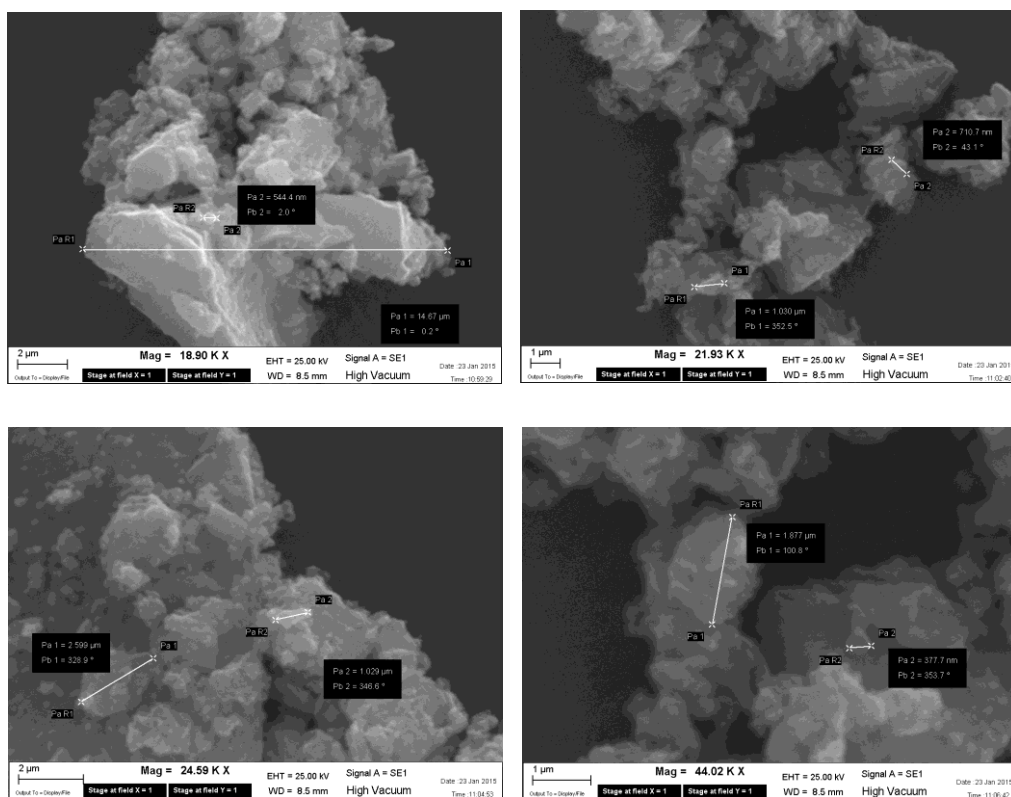
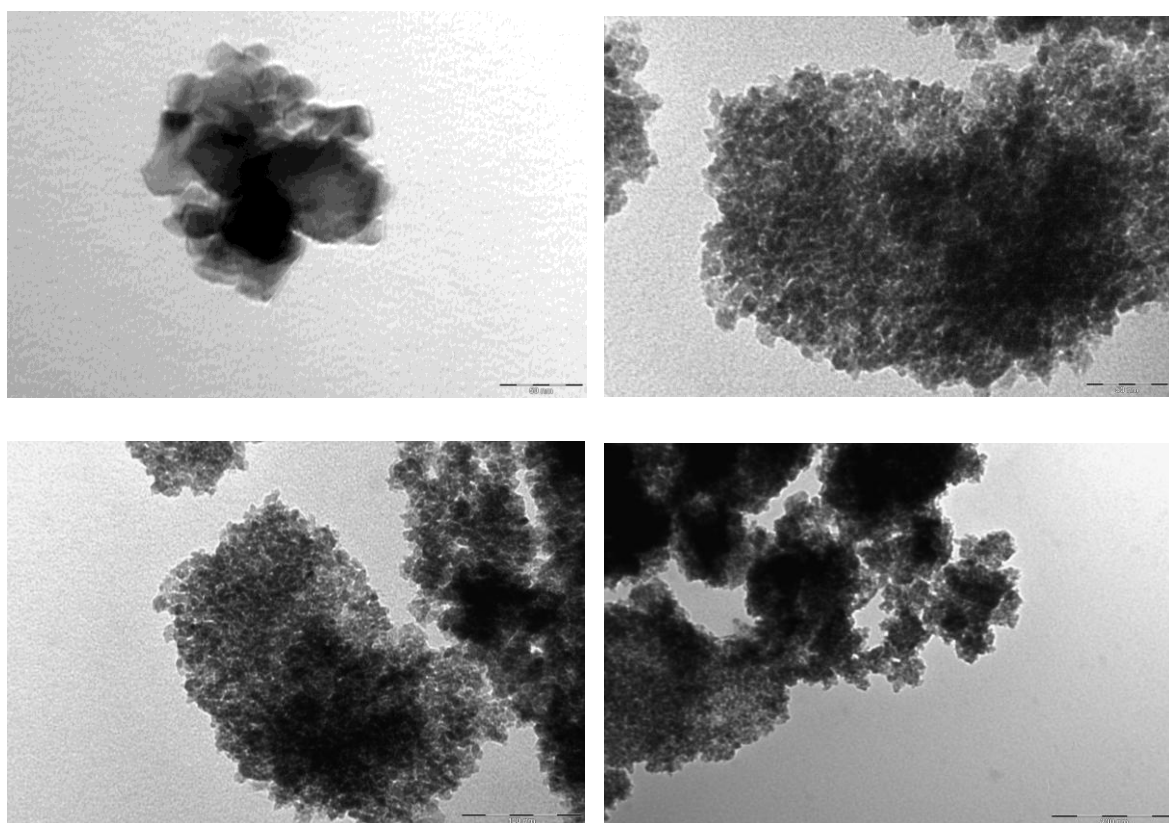


Fig. 16 – SEM images of the dried product of Synthesis 1

SEM images reveals agglomerated particles with sizes ranging in the micrometric scale. It is not possible to identify regular crystalline shapes, confirming that the dimensions of single crystallites are in a lower order of magnitude than microns, below the resolution capability of SEM.

- **Transmission Electron microscopy (TEM) morphological characterization**

TEM allowed to morphologically characterize the single crystallites composing the sample, as showed in *Fig. 17*.



*Fig. 17– TEM images of the dried product of Synthesis 1*

Observed agglomerates are composed by particles of irregular and compact shape ranging from 10 nm to 30 nm ( in agreement with the approximate value obtained by Sherrer equation ) showing a quite narrow size distribution. Moreover, the recorded images suggest that the Titanium dioxide nanoparticles should have elevate values of relative surface area.

- **DLS size measurement**

DLS measurements have been performed on a suspension of Titanium dioxide nanoparticles to obtain information about the aggregation state of the particles in liquid phase excluding the influence of a forced drying applied in the preparation of SEM and TEM samples. Initially, the sample was prepared by diluting 50  $\mu\text{l}$  of Titanium dioxide nanoparticles suspension into 50 ml distilled water, followed by sonication. The analysis shows a size distribution composed of three main population with a hydrodynamic diameter of 888 nm, 195 nm and 4866 nm, ordered by intensity (*Fig. 18*) and a high polydispersion index.

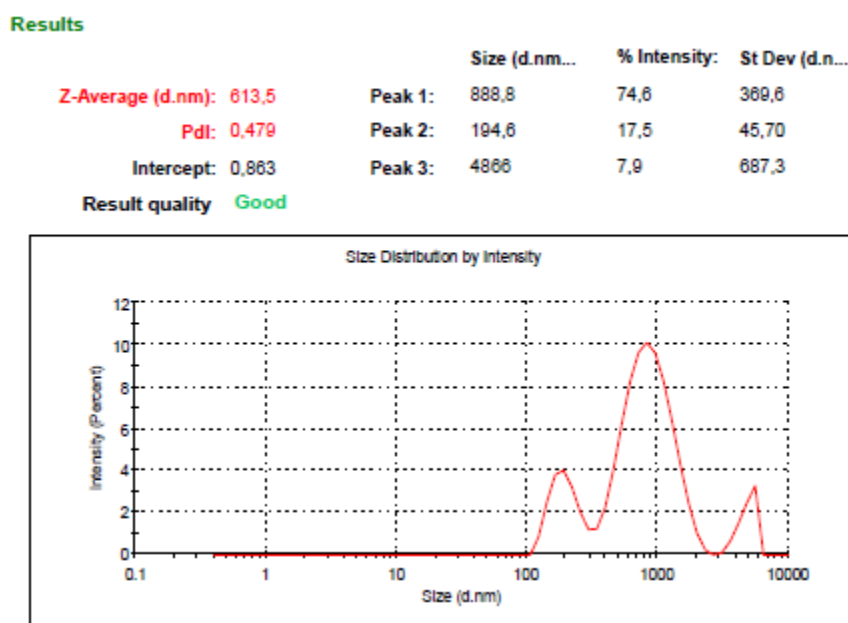


*Fig. 18 – DLS size measurement report of the product of Synthesis 1 dispersed in water*

Since the aggregation of the nanoparticles is highly affected by the solvent, a second analysis was performed by diluting Titanium dioxide nanoparticles suspension into a 25 % volume isopropyl alcohol solution in water, similar to the reaction environment, followed by sonication. The refractive index of the solvent was deduced from reported tables.

The second analysis shows a lower polydispersion index ( PdI ), a main population of particles with a hydrodynamic diameter of 253 nm, and a small population with hydrodynamic diameter in the nanoscale ( 58 nm ) as reported in *Fig. 19*.

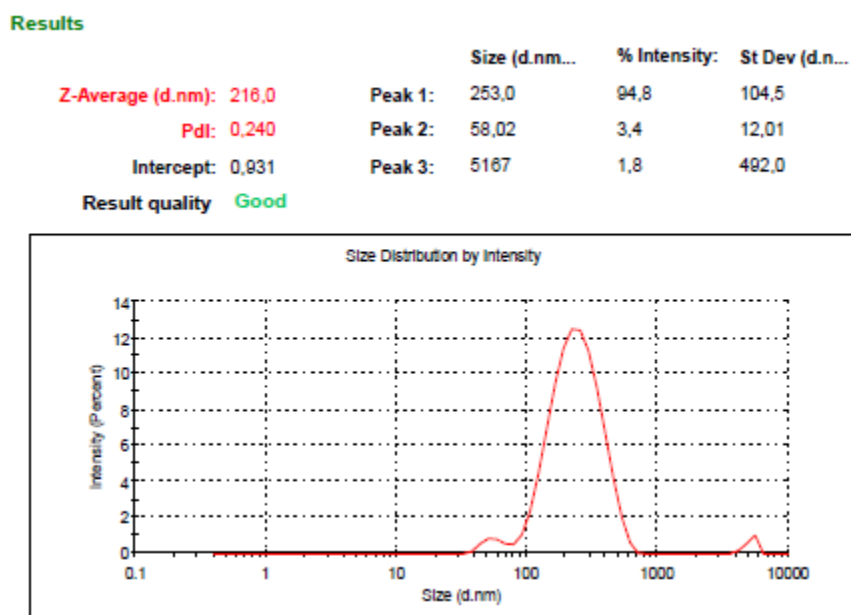


Fig. 19 – DLS size measurement report of the product of Synthesis 1 dispersed in hydro-alcoholic suspension

A measured average size of 216 nm reveals that aggregation phenomenon still occurs in hydro alcoholic suspension, but the lower value and the presence of a secondary peak at 58 nm indicates that the hydro-alcoholic mixture play a role in stabilizing dispersed Titanium dioxide nanoparticles, and successive modifications to the synthesis product ( i.e. dilution with different solvents or solid phase separation processes ) results in agglomeration of particles and possibly in loss of activity.

The addition of surfactants or stabilizing agents will probably improve particle dispersion, but this clashes with the aim of obtaining a highly active material by a synthetic path as “green” and simple as possible. Moreover, the presence of surfactant can interfere in solid surface spray application and removal could be challenging.

- **BET surface area measurement**

Effectiveness of any heterogeneous catalyst, whatever the mechanism related to adsorption and reaction, is largely dependent by catalyst surface area [Knözinger et al., 2002 ]. To measure the specific surface area of produced Titanium dioxide nanoparticles, BET technique have been performed on dried samples; in order to minimize aggregation phenomena occurring during drying procedure, powders have been dry sonicated before analysis.

Results, reported in *Tab. 6*, shows a value of 239.3 m<sup>2</sup>/g for the specific surface area which is quite relevant. The data is accompanied by quality analysis parameters indicating a very good linearity of experimental points and the correct response of sample to the technique: a positive C value not far from 100-200 is in fact evidence of completion of the Langmuir monolayer.

### Multi-Point BET

#### Data Reduction Parameters Data

<u>Adsorbate</u>	Nitrogen	Temperature	77.350K	
	Molec. Wt.: 28.013	Cross Section:	16.200 Å <sup>2</sup>	Liquid Density: 0.808 g/cc

#### Multi-Point BET Data

Relative Pressure [P/Po]	Volume @ STP [cc/g]	1 / [ W((Po/P) - 1) ]	Relative Pressure [P/Po]	Volume @ STP [cc/g]	1 / [ W((Po/P) - 1) ]
7.16190e-02	50.8157	1.2147e+00	1.96500e-01	64.7637	3.0213e+00
7.91470e-02	51.6843	1.3306e+00	2.25284e-01	67.8601	3.4287e+00
9.73850e-02	53.8548	1.6029e+00	2.46113e-01	70.1008	3.7261e+00
1.22605e-01	56.7407	1.9705e+00	2.73413e-01	73.0617	4.1209e+00
1.45878e-01	59.2798	2.3052e+00	2.97981e-01	75.8265	4.4789e+00
1.78724e-01	62.8168	2.7718e+00			

#### BET summary

Slope =	14.351
Intercept =	2.007e-01
Correlation coefficient, r =	0.999977
C constant =	72.489
<b>Surface Area =</b>	<b>239.326 m<sup>2</sup>/g</b>

*Tab. 6 – Report of the BET surface area measurement of the dried product of Synthesis 1*

### 3.1.1.1- PHOTO ACTIVITY TEST: METHYLENE BLUE SOLUTION (*Experiment 1*)

Photo induced oxidative capabilities of produced Titanium dioxide nanoparticles, have been evaluated by following the degradation performed on an organic dye 3,7 bis-(dimethylammino)phenazationium chloride, commonly known as methylene blue (*Fig. 20*). This heterocyclic aromatic compound shows an intense absorption band in the visible region, with a maximum at 668 nm characterized by a molar absorption coefficient  $> 70000$  and a shoulder at 615 nm due to dye dimerization, as shown in *Fig. 20*.

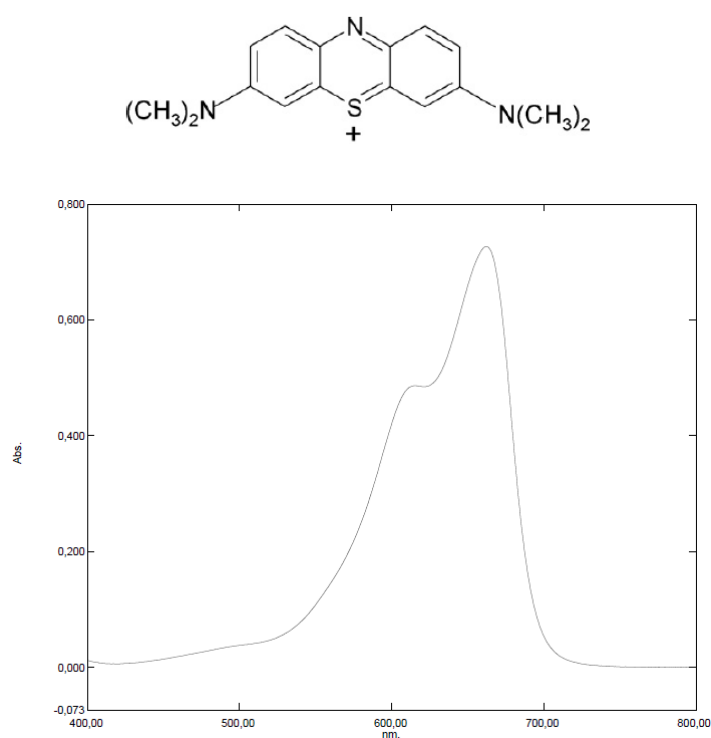
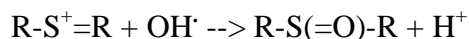


*Fig. 20 – Molecular structure and absorption spectrum of 3,7 bis-(dimethylammino)phenazationium cation, commonly known as methylene blue in the chloride salt form*

By monitoring the absorption value decay along photoinduced reaction it is possible to appreciate the amount of oxidizing species produced by a catalyst. In particular degradation of this molecule by Titanium dioxide nanoparticles in aqueous solution proceed by two different

paths: oxidation of the dye and sequential cleavage of N-CH<sub>3</sub> bonds. OH<sup>•</sup> radicals diffusing from the catalyst surface can attack the functional group C-S<sup>+</sup>=C with formation of a sulfoxide:



The electrophilic attack involve the doublet free heteroatom S, resulting in oxidizing it, however the preservation of conjugation of the double bonds is required, inducing then the central opening of the aromatic ring, and hence the disappearance of visible absorption (*Fig. 21*) [S. Xia, et al, 2015].

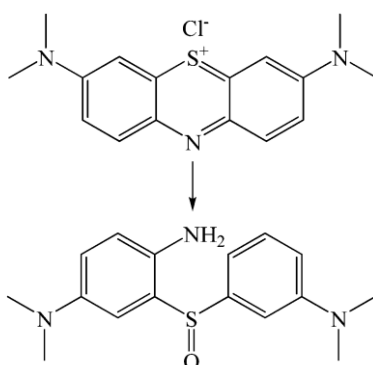


*Fig. 21 – Reaction scheme of opening of the central aromatic ring of methylene blue as a result of the electrophilic attack of OH<sup>•</sup> radicals.*

Necessary H atoms to CH and NH bond formation may result from the reduction of protons by photogenerated electrons on catalyst conduction band [A.Houas et al., 2001]. Meanwhile the degradation of the two auxocromic groups ( -NR<sub>2</sub> ) [M. A. Raufet al., 2010] is relatable to observed ipsocromic effect, comporting a “blue shift” in the maximum absorption lambda due to subsequent formation of intermediate absorbing species ( *Fig. 22* ).

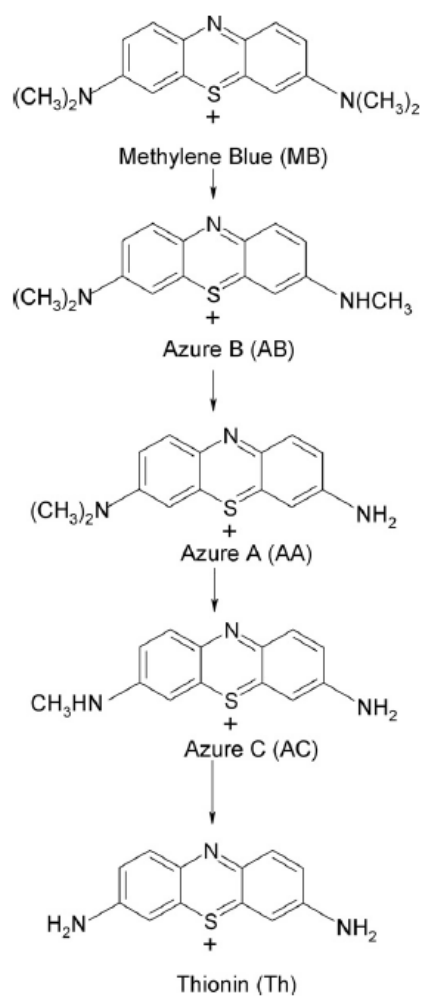
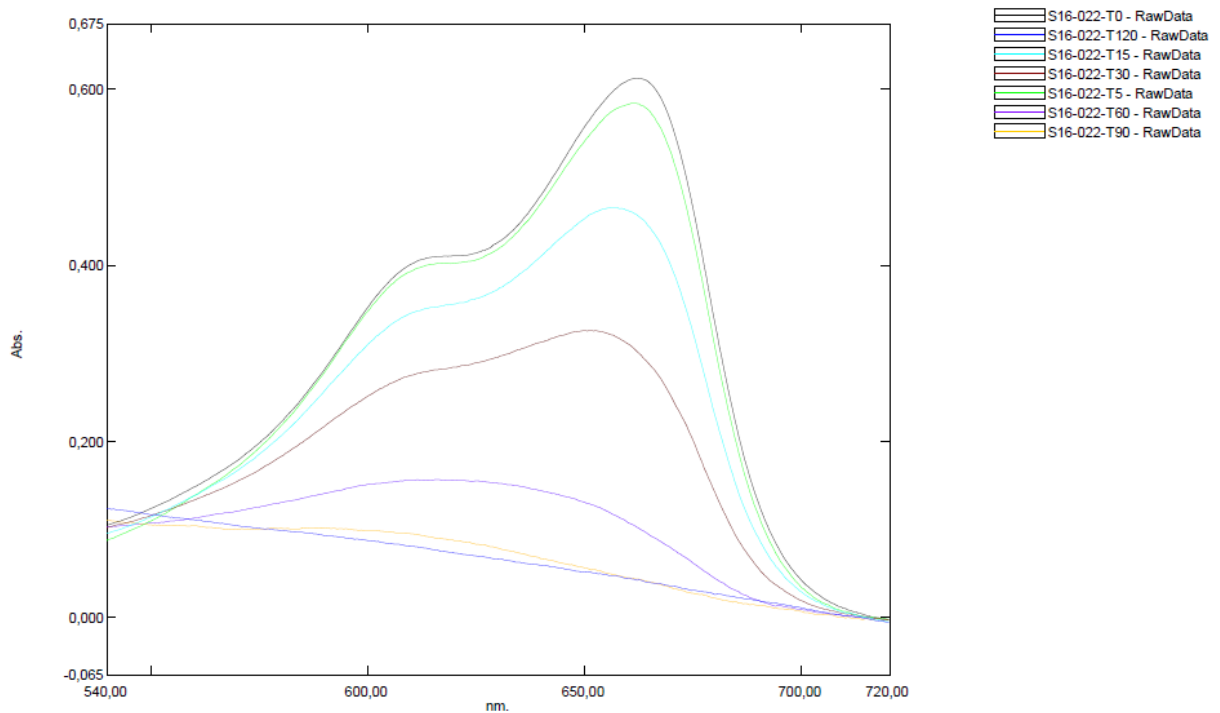


Fig. 22 – Sequential degradation of the  $-\text{NR}_2$  auxochromic groups of methylene blue

Performed photoactivity test in aqueous solution reveals effective disappearance of methylene blue absorption band within 90-120 minutes in the reported conditions, as shown in Fig. 23.



*Fig. 23 - Disappearance of the methylene blue absorption band as result of photodegradation catalyzed by Titanium dioxide*

In addition to “blue shift” phenomena, an increasing baseline value is observed at shorter wavelength relative to the increasing scattering of the solution due to aggregation of Titanium dioxide particles occurring during the test. This experimental imperfection could be overcome by centrifuging the sample before collecting the spectra, but it was observed a blue coloration in the deposited solid after centrifugation, suggesting that an amount of dye would be removed by physisorption-precipitation, so the whole suspension was analyzed. By referring to intensity of absorbance values recorded at 668 nm vs time, a kinetic curve proportional to the analyte concentration is obtained. Different catalyst effectiveness can be appreciated by comparing degradation kinetic curves obtained in the same conditions: in *Fig. 24* a comparison between synthesized Titanium dioxide and commercially available photoactive Titanium dioxide (Degussa P25) is reported. The absorbance data are elaborated and reported as  $C/C_0$  ratio related to dye concentration.

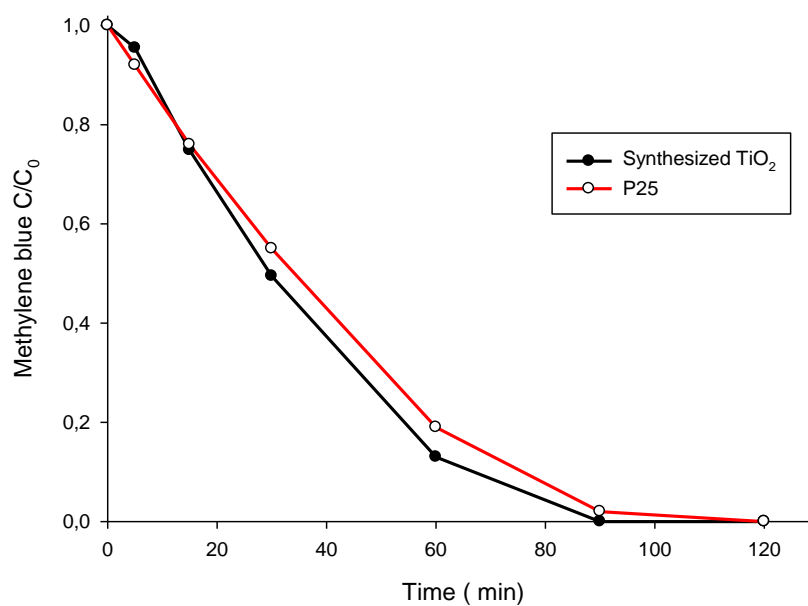


*Fig. 24 – Photodegradation of methylene blue: comparison of catalytic performances between TiO<sub>2</sub> produced by Synthesis 1 and commercially available photoactive TiO<sub>2</sub> (Degussa P25)*

In any case, Langmuir-Hinshelwood model serves as a base to describe photodegradation of organic compounds performed by Titanium dioxide [ N. T. Dung – A. Millis – I.T. Horvath ], but in particular cases, such as low concentration of analyte or Titania suspension mediated photolysis, kinetic can be satisfyingly approximated to first order [K. Kabra - I. K. Konstantinou] or pseudo-zero order [M. F. J. Dijkstra et al., 2001].

### 3.1.2- TITANIUM DIOXIDE THERMAL TREATMENT, CHARACTERIZATION

Dried Titanium dioxide have been thermally treated 1 hour at 420°C with the aim of improving photocatalytic behavior by increasing crystalline degree, as reported by many authors engaged in sol-gel synthesis [S. Sakka, 2005].

- **X-ray powder diffraction Characterization**

X ray diffraction pattern obtained by thermally treated  $\text{TiO}_2$  (Fig. 25) does not reveal changes in crystal phase composition. A slight narrowing of peaks is observed probably due to crystalline grain growth and/or to the increase of the crystalline order.

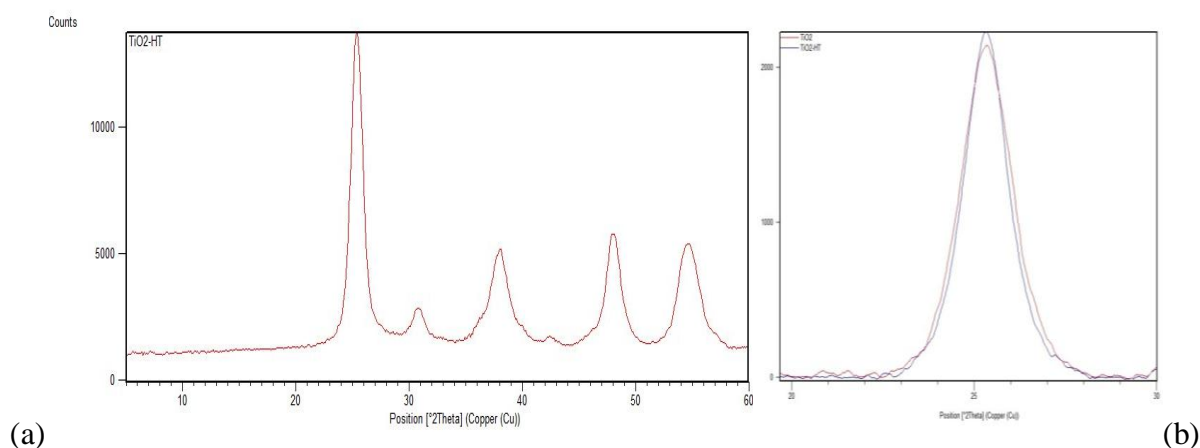
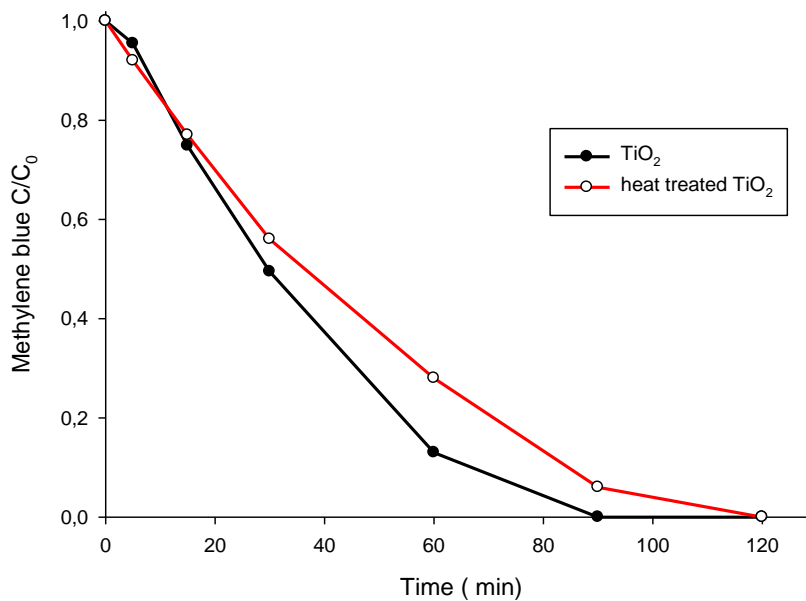


Fig. 25- Experimental X ray diffraction pattern of the thermal treated product of Synthesis 1(a), and comparison on the 101 peak ( $25.3^\circ 2\theta$ ) with untreated product of Synthesis 1

### 3.1.2.1- PHOTO ACTIVITY TEST: METHYLENE BLUE SOLUTION

Differently to previous reported results [S. Sakka, 2005], the thermal treatment resulted in a lower performance compared with the untreated sample, in the degradation of Methylene blue solution, as reported in *Fig. 26*.



*Fig. 26 – Photodegradation of methylene blue: comparison of catalytic performances between TiO<sub>2</sub> produced by Synthesis 1 and heat treated TiO<sub>2</sub> produced by Synthesis 1*

Loss of activity was possibly due to reduction of specific surface area obtained by thermal treatment; enhanced diffusion allows to re-crystallize matter arranged in less ordered motifs, contributing to lower free energy, but also provoking crystalline grain growth. It can be speculated that defective grain-border regions are responsible of local distortion to the bulk band gap, resulting in more reactive sites characterized by enhanced charge carrier transport or electron-hole pair generation efficiency.

- **BET surface area measurement**

BET surface area measurement provided a confirmation to previously reported hypothesis: the thermal treatment applied in order to enhance photocatalytic activity, resulted conversely in a loss of activity due to a reduction of -17.2 % in specific surface area, as visible in *Tab. 7*.

Multi-Point BET					
Data Reduction Parameters Data					
<u>Adsorbate</u>	Nitrogen	Temperature	77.350K	Liquid Density:	0.808 g/cc
	Molec. Wt.: 28.013	Cross Section:	16.200 Å <sup>2</sup>		
Multi-Point BET Data					
Relative Pressure [P/Po]	Volume @ STP [cc/g]	1 / [ W((Po/P) - 1) ]	Relative Pressure [P/Po]	Volume @ STP [cc/g]	1 / [ W((Po/P) - 1) ]
5.88170e-02	39.9934	1.2502e+00	2.00196e-01	52.8342	3.7906e+00
7.56160e-02	41.6844	1.5701e+00	2.22043e-01	54.7417	4.1717e+00
9.71640e-02	43.7053	1.9702e+00	2.45433e-01	57.9392	4.4917e+00
1.23210e-01	46.0762	2.4402e+00	2.73434e-01	60.2638	4.9966e+00
1.48944e-01	48.3787	2.8944e+00	3.00864e-01	63.0054	5.4649e+00
1.77320e-01	50.8476	3.3916e+00			
BET summary					
	Slope =	17.322			
	Intercept =	2.837e-01			
	Correlation coefficient, r =	0.999681			
	C constant =	62.055			
	Surface Area =	197.803 m <sup>2</sup> /g			

*Tab. 7 – Report of the BET surface area measurement of the thermal treated product of Synthesis 1*

### 3.1.3- TITANIUM DIOXIDE HETEROCOAGULATION ON SILICA, CHARACTERIZATION ( *Synthesis 2* )

To improve catalyst dispersion and maximize active surface area of Titanium dioxide nanoparticles, an heterocoagulation on silica microparticles have been performed. As reported by [P. Wilhelm et al., 2007], an heterocoagulation spontaneously occurs between TiO<sub>2</sub> and SiO<sub>2</sub> particles in a wide range of pH values, driven by electrostatic interaction taking place as a consequence of the difference in Zeta potential value. The obtained suspension appears more stable in terms of precipitation and phase separation, even after several days rest.

- **Scanning Electron Microscopy (SEM) morphological characterization**

Dried solid product have been morphologically investigated by SEM imaging, *Fig. 27*. showing fluffy aggregates with dimensions ranging between 1 and 10 micrometers.

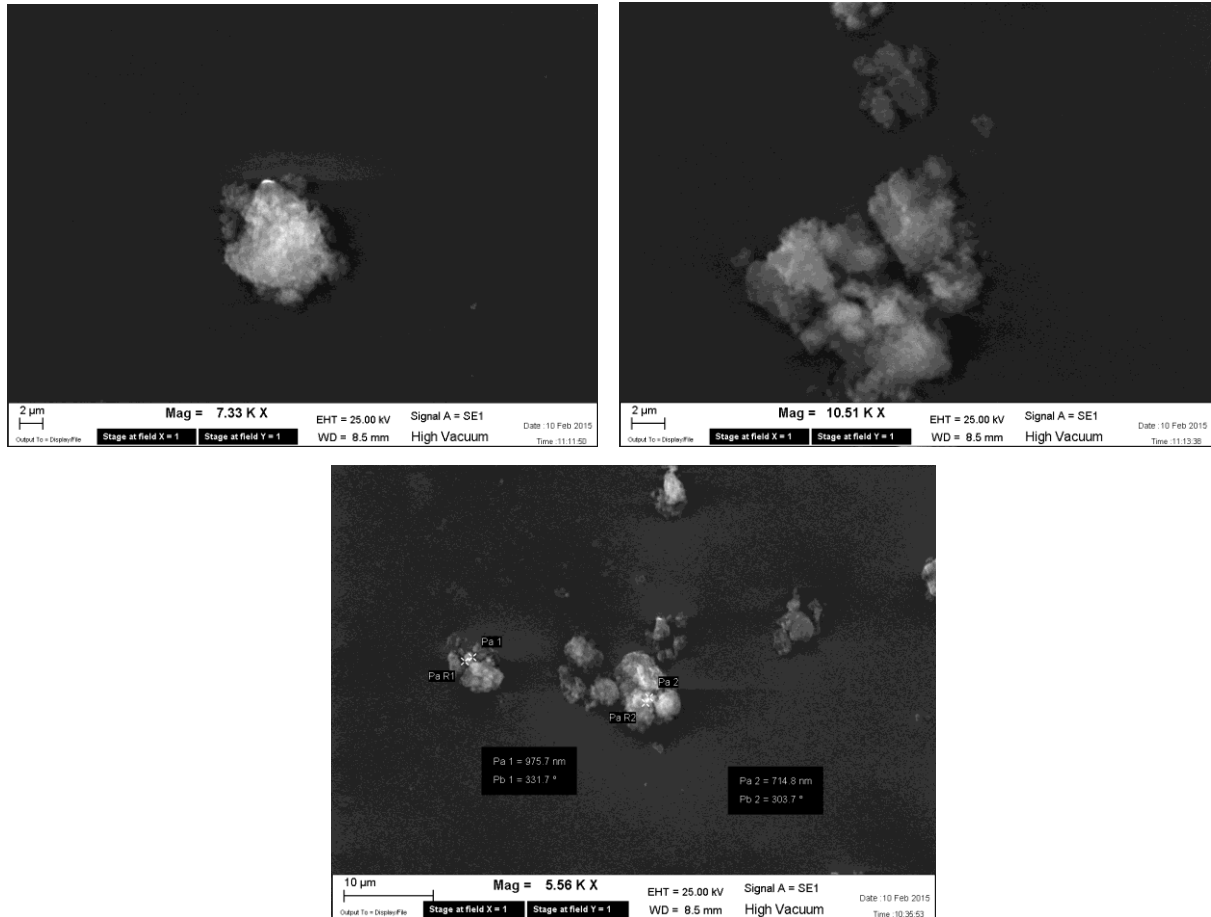


*Fig. 27 – SEM images of the dried product of Synthesis 2*

- **X-ray powder diffraction Characterization**

XRPD analysis reveals the peaks corresponding to the Anatase/Brookite phases and confirms the crystalline phase composition as visible in *Fig. 28*. Higher intensity of the baseline is due to amorphous Silica X-ray scattering

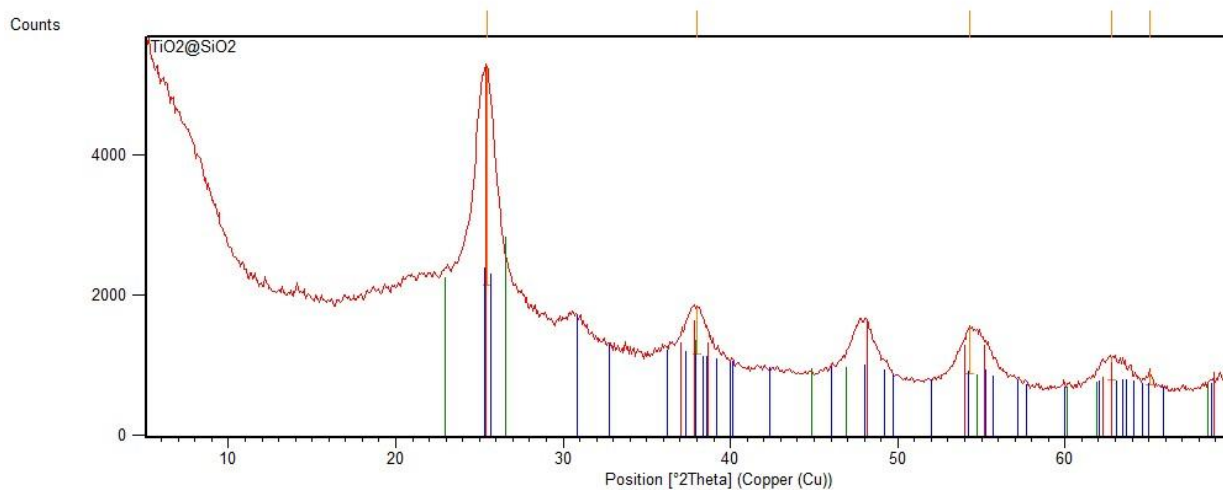


*Fig. 28 - Experimental X ray diffraction pattern of the dried product of Synthesis 2 with peak position of reference pattern*

### **3.1.3.1- PHOTO ACTIVITY TEST: METHYLENE BLUE SOLUTION**

The Photoactivity test was performed in such a way that the amount of Titanium Dioxide was the same in both suspensions. The on Methylene blue solution reveals substantial improvement shown by Titanium dioxide coated Silica particles compared to simple  $\text{TiO}_2$  suspension ( *Fig. 29*). Silica adhesion improves the catalyst dispersion and maximizes its active surface area. However, the lowering of the suspension pH value by Silica acid, may play a role in the dye oxidation kinetic. In fact, it was reported by [P. Wardman, 1989] that the redox potential of the  $\text{OH}^\cdot$  moves from +1.9 V to +2.7 V by changing the environment pH from basic to acid.

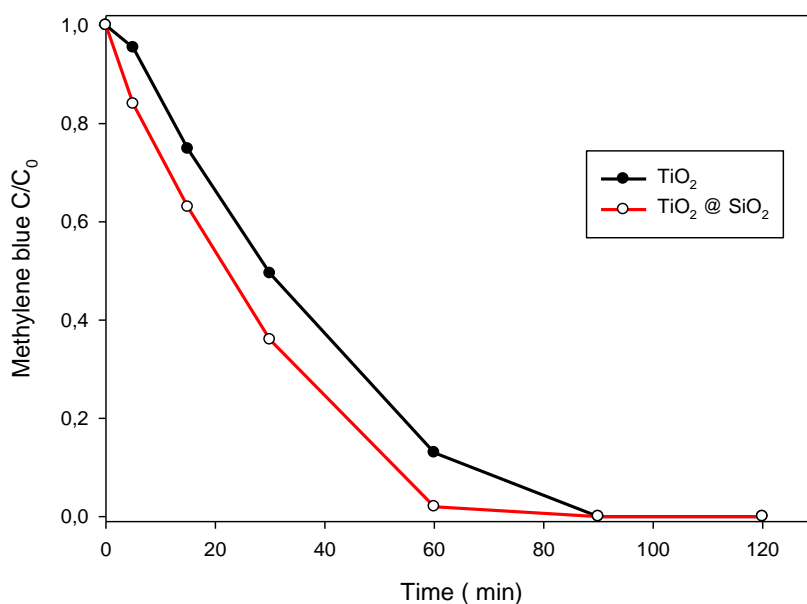
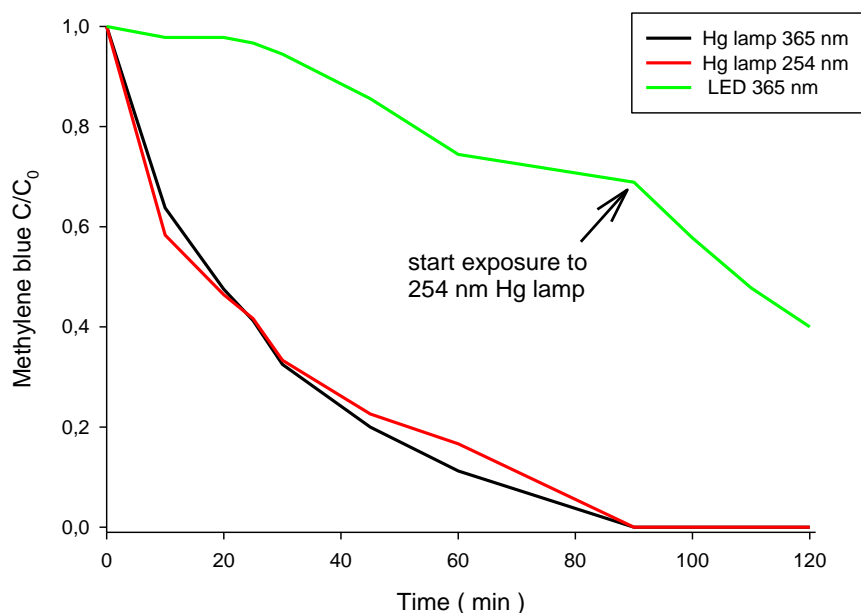


Fig. 29 – Photodegradation of methylene blue: comparison of catalytic performances between TiO<sub>2</sub> produced by Synthesis 1 and TiO<sub>2</sub> on SiO<sub>2</sub> particles produced by Synthesis 2

### 3.1.4- UV SOURCE COMPARISON

According to [J. Perkowsky et al., 2003], energy band gap in Titanium dioxide semiconductors (Anatase polymorph) lies around 3.2 eV, corresponding to an electromagnetic radiation with 388 nm wavelength. Theoretically any radiation providing at least this amount of energy and capable of being absorbed by the photocatalyst, can promote electron-hole pair generation on semiconductor surface in equal manner. As a simplification, we can assume that the amount of generated radicals should be affected only by the e-h recombination rate (intrinsic feature of all semiconductors [C. Minero, et al., 2006], number of absorbed photons and disposed surface area. However, many parameters can practically affect the observed degradation rate. To obtain a realistic reply different UV sources have been tested in analogous condition. High pressure and low pressure Hg vapor lamps ( $\lambda = 365$  nm, 254 nm, 25 Watt) are compared with a purposely built LED system (composed by 160 LEDs for a total 22.6 Watt,  $\lambda = 365$  nm). From the obtained data, reported in Fig. 30 as Methylene blue C/C<sub>0</sub> ratio along time, it is clearly visible how both Mercury vapor lamps produce comparable degradation rate of organic dye by

Titanium dioxide suspension, while LED illumination reveals less performing photoactivation. To be sure that the effect is completely attributable to the UV source, after 90 minutes the suspension revealing lower degradation rate is moved to Hg lamp exposure ( $\lambda = 254 \text{ nm}$ ), showing immediately an increment in degradation process (*Fig. 30*).



*Fig. 30 - Photodegradation of methylene blue: comparison of catalytic induction between different UV sources on  $\text{TiO}_2$  produced by Synthesis 1*

To explain the observed results, the effective emission spectra of the sources were recorded and compared (*Fig. 31*).

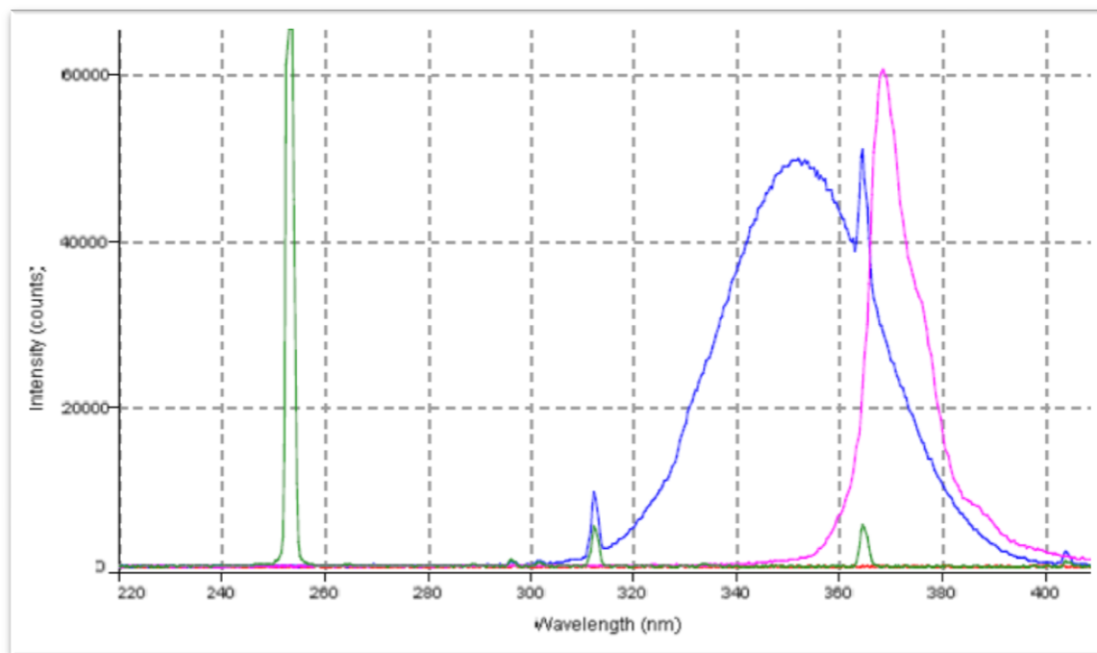


Fig. 31 – Emission spectra of different UV sources: Green line Hg low pressure lamp, blue line Hg high pressure lamp, pink line UV LEDs.

Even if the intensity values are not comparable (the spectra in Fig. 31 have been scaled to be more clearly superimposable) a neat difference is observable in terms of emission bandwidth: while low pressure Hg vapor lamp provides a narrow peak in correspondence of the nominal wavelength of 254 nm, both nominally 365 nm wavelength sources, LED system and high pressure Hg lamp, show wider emission bands, only slightly superimposable. LED system reveals the highest intensity of the band between 365-380 nm, with an effective maximum at 368 nm, while high pressure Hg lamp shows a very wide emission from 320 nm to 380 nm with two maxima at 352 nm and 365 nm. An intuitive explanation of the lower photoactivation performed by LED system is obtained by comparing its reported emission spectrum (Fig. 31) to the Titanium dioxide absorption band reported in Fig. 32, image retrieved from [N. Riaz, et al., 2014].

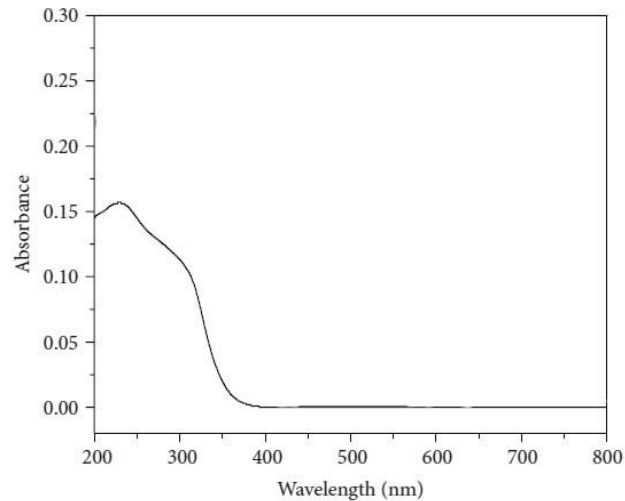


Fig. 32 – Absorption spectrum of Titanium dioxide, image retrieved from [N. Riaz, et al., 2014]

Titanium dioxide shows absorption starting from 370-350 nm ( depending on the information source ) and is clearly arguable a lack of overlap with the LED emission spectra compared to these obtained by both Hg lamp sources. In addition, UV LED system initially considered an interesting source for this kind of applications, in practice results unaffordable for several reasons: (i) UV LED system is drastically more expensive than commonly used Mercury lamps although requires less energy and maintenance, (ii) in commercially available LEDs, the shorter the wavelength, the lower the efficiency of light generation, the higher the commercial price and the difficulty to retrieve . On these bases, LED UV source was not interesting for this project.

### 3.1.5- NO<sub>x</sub> PHOTOCATALYZED ABATEMENT, STATIC CONDITIONS (Experiment 2)

Nitrous oxides removal can be obtained by photoinduced oxidation process catalyzed by Titanium dioxide in his photoactive polymorph. The surface electron-hole generation phenomena related to the absorption of proper energy photons ( energy higher or equal to semiconductor bandgap ) performed by the catalyst, results in generating a cascade of radical species capable of nonspecific oxidation towards many molecules. In particular, the main species produced and involved in oxidative processes are hydroxyl radical and superoxide ions [J. Angelo, et al., 2013]. Valence band holes can in fact react with water molecules adsorbed on the semiconductor's surface resulting in the formation of hydroxyl radical, meanwhile electrons promoted to the conduction band are able to reduce oxygen molecules to superoxide ions:

- $SC ( h_{VB}^+ ) + H_2O_{ads} \rightarrow SC + OH^*_{ads} + H^+$
- $SC ( e_{CB}^- ) + O_{2\ ads} \rightarrow SC + O_2^{\cdot -}$

Oxidation of NO<sub>x</sub> resulting in nitrates and Nitric acid formation can occur in gas phase by reaction with desorbed diffusing radicals or directly on catalyst surface involving an adsorption step of the analyte [J.S. Dalton et al., 2002].

- $NO_{g,ads} + 2OH^*_{g,ads} \rightarrow NO_{2\ g,ads} + H_2O_{g,ads}$
- $NO_{2\ g,ads} + OH^*_{g,ads} \rightarrow NO_3^- + H^+$
- $NOx_{g,ads} + O_2^{\cdot -} \rightarrow NO_3^-$

#### 3.1.5.1- STATIC REACTOR - BLANK MEASUREMENT

In order to evaluate the performances of synthesized Titanium dioxide particles on Nitrous oxides removal from gas mixture, heterogeneous catalysis test have been performed. Initial tests in static gas conditions were performed within a sealed chamber. The NO<sub>x</sub> concentration was monitored along time under UV exposure and in presence/absence of the titanium dioxide catalyst . (for an accurate description see the experimental section ).

Deep UV radiation are capable of Ozone generation by environmental Oxygen bond homolysis and also gaseous NO<sub>2</sub> can absorb deep UV radiations and convert to photolytic products [D. Fowler, et al. 1998]. In order to separate and evaluate the single role of different mechanisms contributing to NO<sub>x</sub> scavenging from the system, UV induced degradation in absence of any catalyst have been measured. Data obtained are reported in *Fig. 33* as normalized concentration percentage vs time.

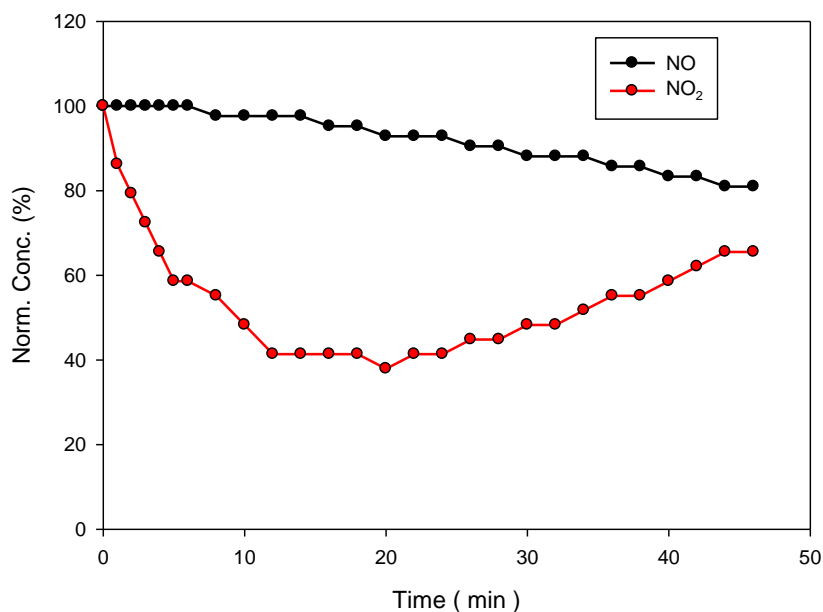


*Fig. 33 –Concentration variations of NO and NO<sub>2</sub> within a sealed chamber vs time of irradiation with 254 nm UV lamp in absence of catalyst. Concentrations are reported normalized and expressed as percentage.*

The data confirms the existence of a degradation phenomenon performed by low pressure Hg vapor lamp UV radiation ( $\lambda = 254 \text{ nm}$ ) on gaseous NO<sub>x</sub>. As shown by *Fig. 33*, NO<sub>2</sub> concentration quickly drop by photolytic processes, while NO start to decrease after a delay of time, related to Ozone formation. After approximately 15-20 minutes, the oxidative reaction occurring between NO and O<sub>3</sub> became predominant determining an increase in NO<sub>2</sub> concentration. This increase appears more pronounced respect to the NO scavenging since the normalization of the concentration values masks the difference in concentration between NO<sub>2</sub> and NO. In fact, the NO<sub>2</sub> concentration is more than one order of magnitude lower than NO one (see Experimental section). On the basis of the obtained results, all successive tests and prototypes involves the use of the low pressure Hg vapor lamp ( $\lambda = 254 \text{ nm}$ ) as UV source

instead of high pressure one ( $\lambda = 365$  nm) since the removal rate of the analyte is enhanced in the first case by the ozone generation process. Anyway in the first set of subsequently reported tests, involving static reactor setup, the single role of catalyst have been evaluated by subtracting the recorded UV contribution, considered as a “blank”.

### 3.1.5.2- STATIC REACTOR - CATALYST EFFECTIVENESS EVALUATION

After the instrumental layout have been set for static test blank, effective tests on Titanium dioxide catalyst have been performed. As described in detail in the experimental section, a stainless steel net basket surrounding the UV lamp is used as catalyst support. The net basket is soaked in the titania hydro-alcoholic suspension obtained via sol-gel synthesis, without the addition of adhesive or linker. After that the UV source is turned on the NO<sub>x</sub> concentrations is monitored for 130 minutes; data obtained are reported in *Fig. 34* as normalized concentration percentage.

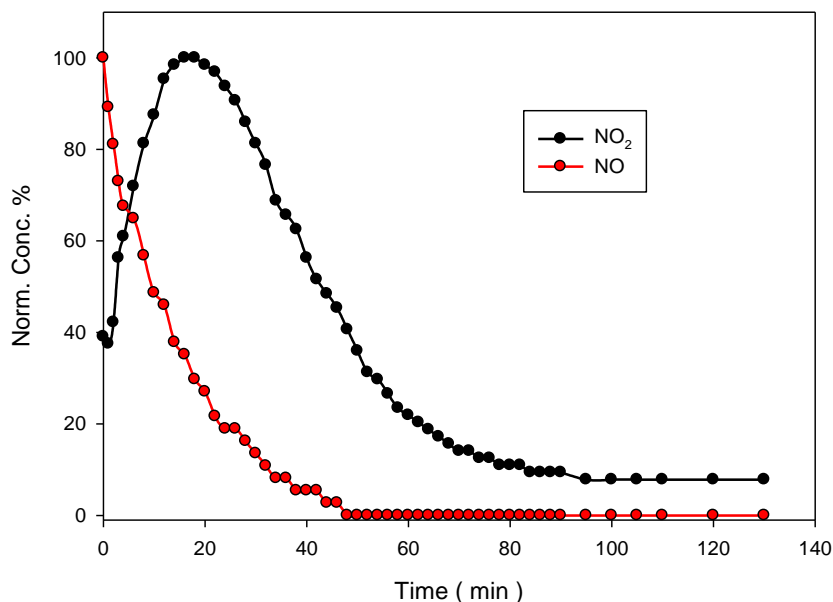


*Fig. 34 - Concentration variations of NO and NO<sub>2</sub> within a sealed chamber vs time of irradiation with 254 nm UV lamp in presence of TiO<sub>2</sub> catalyst obtained by Synthesis 1. Concentrations are reported normalized and expressed as percentage.*

After UV source activation ( time = 0 ), NO concentration drops very fast , reaching half of the initial concentration after 8 minutes and continues to decrease following a first order exponential decay, as expected. Meanwhile, the NO<sub>2</sub> concentration increases in agreement with the NO oxidation process. After 20 minutes, NO concentration is below 20% , and NO<sub>2</sub> formation rate, the predominant process so far, became less relevant compared to NO<sub>2</sub> further oxidation to nitrates or nitric acid ( dependently on the radical specie involved ). After 22 minutes NO<sub>2</sub> oxidation processes become predominant and the analyte concentration start decreasing reaching a constant value after 90 minutes. Although the absolute value is not zero, we can assume that NO<sub>2</sub> removal is almost complete. The NO<sub>2</sub> final concentration value is in fact not far from background value, and is enhanced by data normalization, as clearly visible in Fig.35 where effective concentration data are reported.

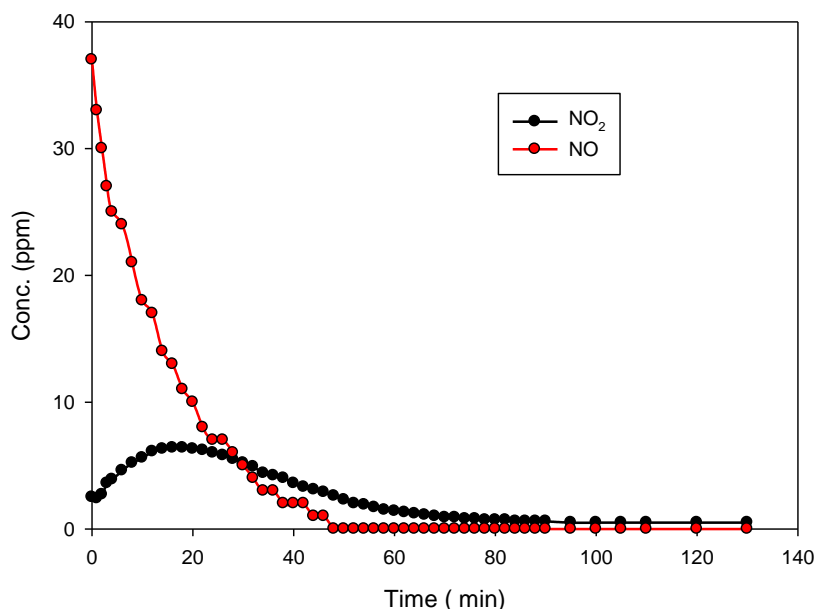
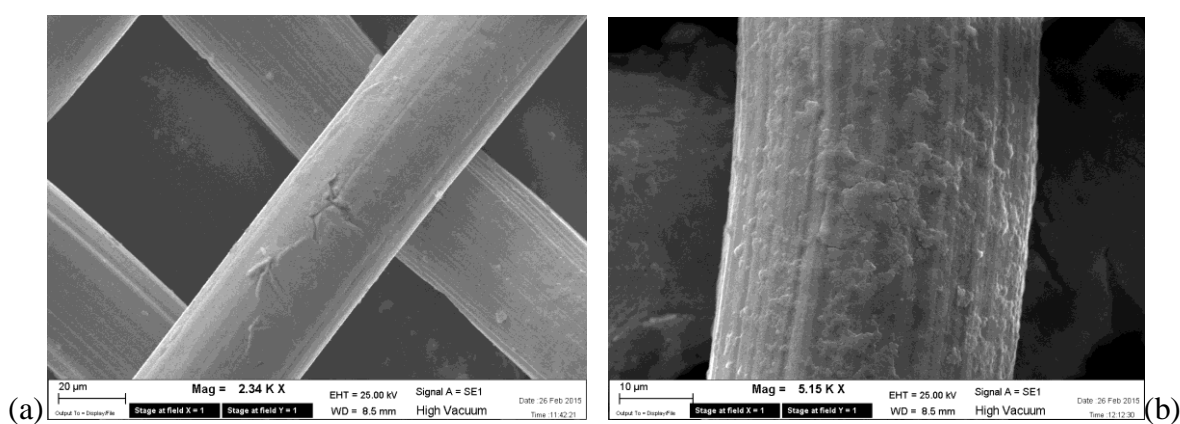


Fig. 35 - Concentration variations of NO and NO<sub>2</sub> within a sealed chamber vs time of irradiation with 254 nm UV lamp in presence of TiO<sub>2</sub> catalyst obtained by Synthesis 1. Effective concentrations are reported.

### 3.1.5.3- SILANE/SILICA SUPPORT COATING (*Synthesis 3*)

Catalyst support is then improved by a Silane / amorphous silica coating as described in experimental section in order to enhance catalyst performances by optimizing adhesion and increasing surface area. [P. Wilhelm et al., 2007]. SEM images comparing uncoated vs coated steel net are reported in *Fig. 36* . It is possible to see the catalyst adhering to the metal wires creating a rough surface.



*Fig 36– SEM images of untreated steel net (a) and Titanium dioxide-Silica adhesion on Silane/Silica coated steel net (b)*

The Titanium dioxide nanoparticles deposited on the coated support have been tested in analogous conditions of static NO<sub>x</sub> scavenging and the results are reported in *Fig. 37*.

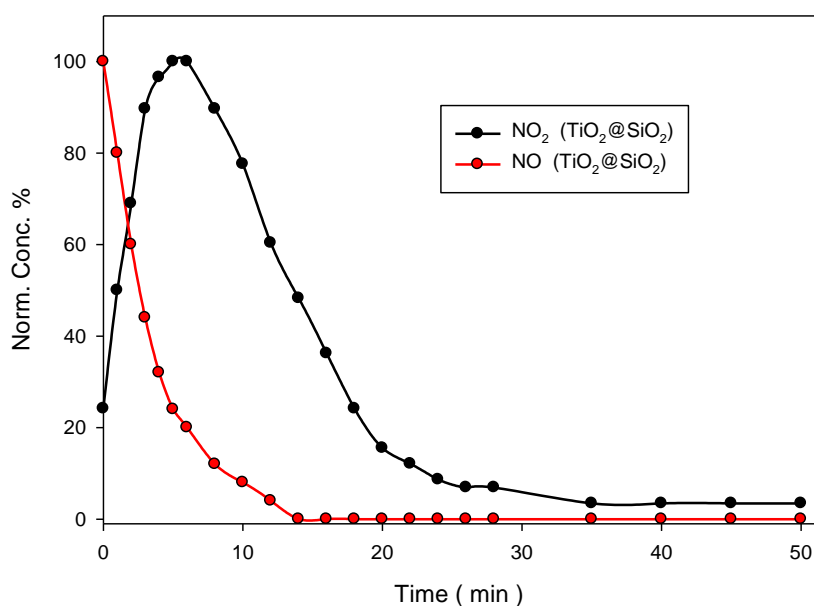


Fig. 37- Concentration variations of NO and NO<sub>2</sub> within a sealed chamber vs time of irradiation with 254 nm UV lamp in presence of TiO<sub>2</sub> catalyst obtained by Synthesis 3. Concentrations are reported normalized and expressed as percentage.

Comparing these results to those obtained by the same Titanium dioxide simply deposited on support surface a comparable behavior is shown, but a relevant increase in the catalytic performances can be clearly appreciated. The half-time for gaseous NO is now reached in less than 3 minutes, and the total disappearance of the analyte is recorded in the 14 minutes range. Also NO<sub>2</sub> increase and subsequent removal is performed in relevantly faster times compared to previously reported catalytic system. A comparison between the two data set is proposed in Fig. 38 in terms of total NO<sub>x</sub> normalized concentration and in Fig. 39 by comparing singular analytes trends.

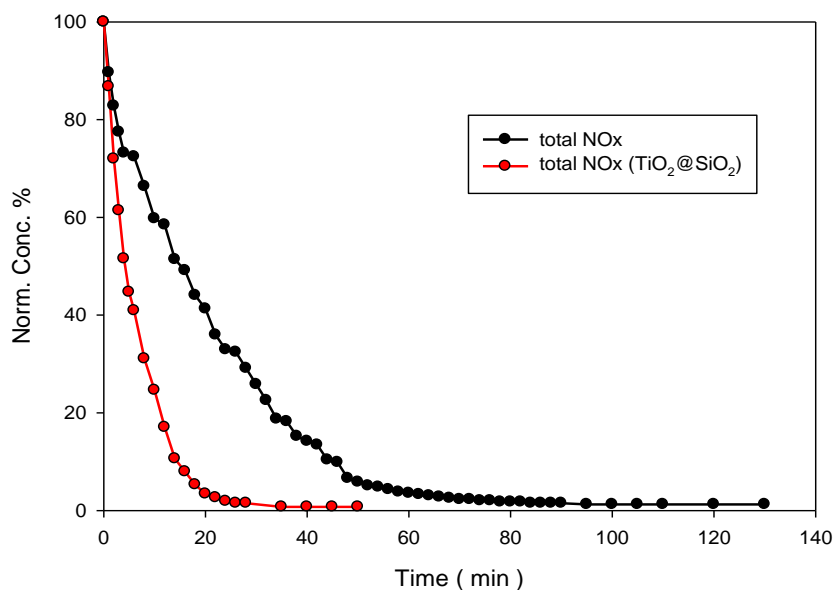


Fig. 38- Concentration variations of total NOx within a sealed chamber vs time of irradiation with 254 nm UV lamp. Comparison of catalytic performances between TiO<sub>2</sub> produced by Synthesis 1 and catalyst produced by Synthesis 3. Concentrations are reported normalized and expressed as percentage.

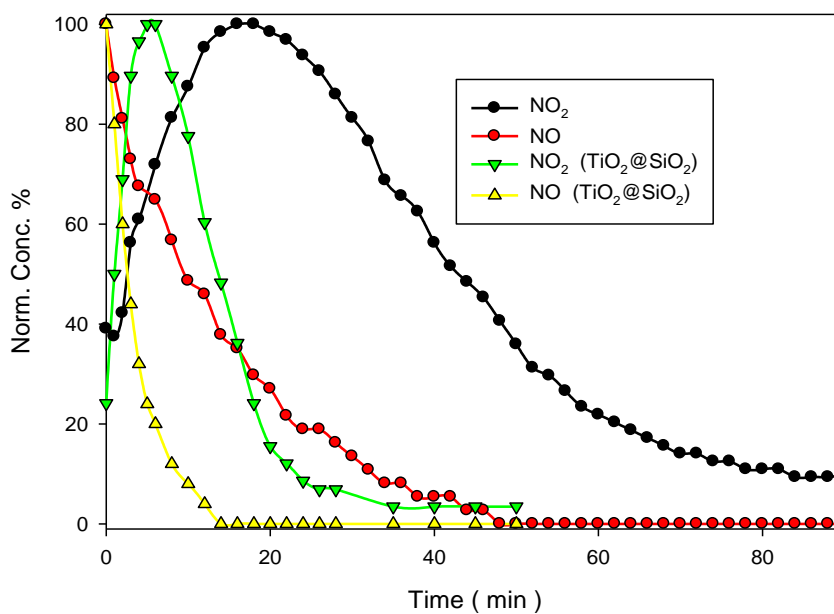


Fig. 39- Concentration variations of NO and NO<sub>2</sub> within a sealed chamber vs time of irradiation with 254 nm UV lamp. Comparison of catalytic performances between TiO<sub>2</sub> produced by Synthesis 1 and catalyst produced by Synthesis 3. Concentrations are reported normalized and expressed as percentage.

### 3.1.6- NO<sub>x</sub> PHOTOCATALYZED ABATEMENT, FLUXING CONDITIONS (Experiment 3)

After demonstrating the catalyst effectiveness on NO<sub>x</sub> scavenging and the important role of Titanium dioxide adhesion on amorphous Silica in order to improve heterogeneous catalysis, the successive step in approaching the real working conditions of the catalytic system is to perform an abatement test in fluxing conditions. A reactor have been built by scale-replicating the real abatement tower existing in the plant, added with a catalytic tube (Fig. 40) designed and prepared following the results obtained under static conditions. The details are reported in experimental section, and SEM images of supported catalyst are reported below, in Fig. 41.

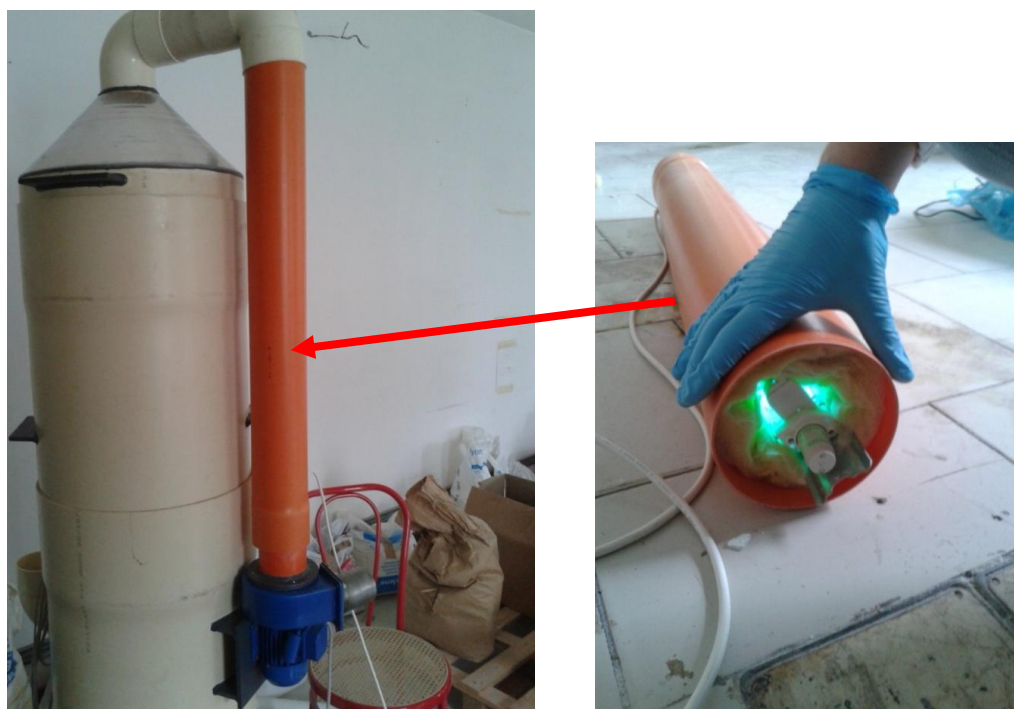
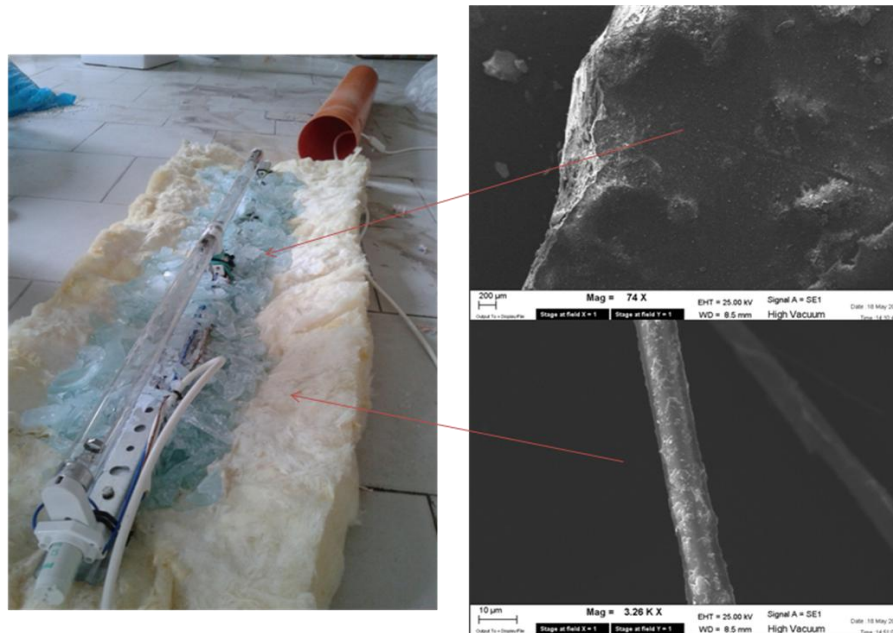


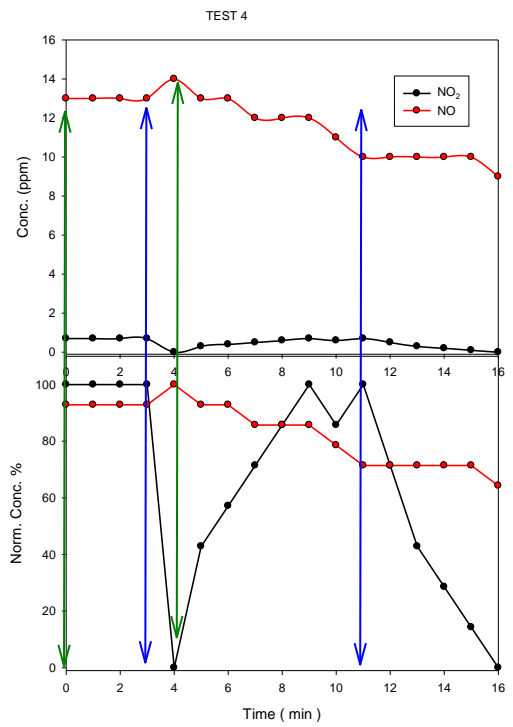
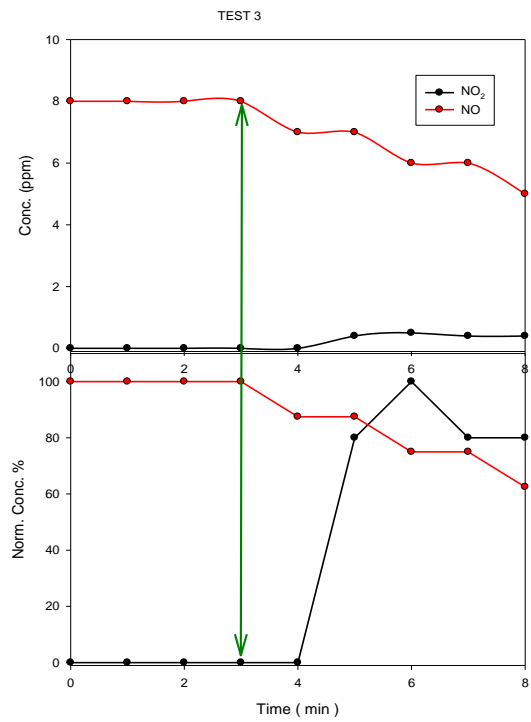
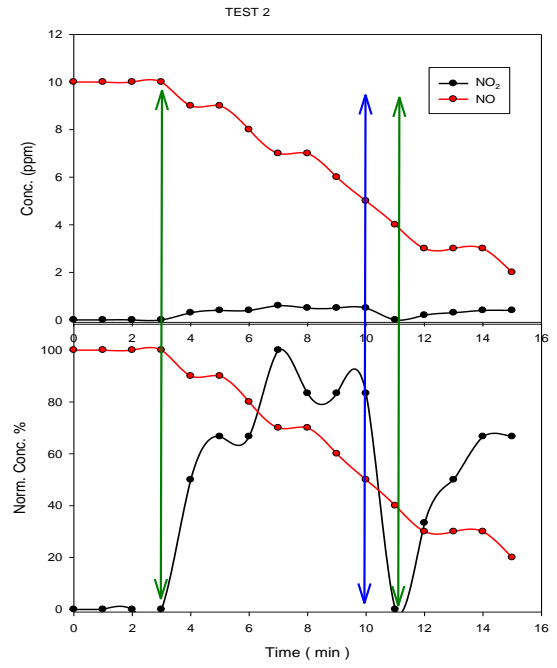
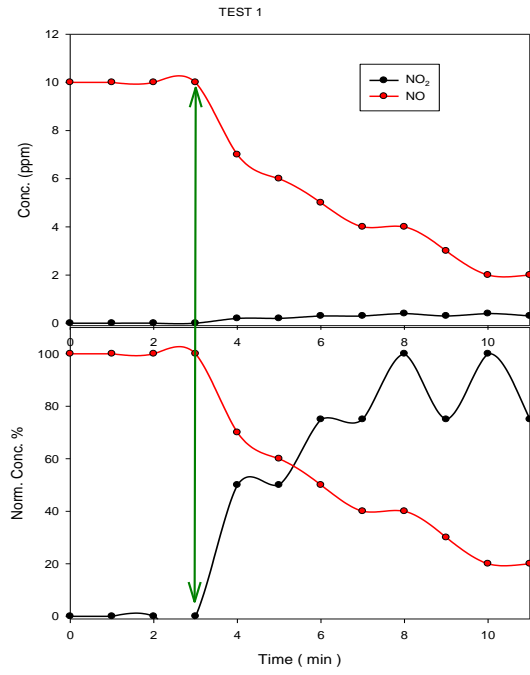
Fig. 40 – Pictures of the prototype and the catalytic pipe



*Fig. 41 – Inner catalytic section composition and SEM images of Titanium dioxide catalyst adhesion of glass pieces and glass wool fibers.*

The tests performed consisted in blowing NO<sub>x</sub> gaseous solution into the prototype air intake ( directly from the cylinder ) while the electric powered fan was providing a constant air flux within the reactor. After reaching a constant value of NO<sub>x</sub> concentration ( detected at the prototype exhaust pipe ), UV source is turned on, and the expected variation in gas composition recorded as a function of time. Also reverse test have been performed by turning off the UV source after reaching a plateau value in NO<sub>x</sub> amount in order to gain a confirmation of the effect of working system on gas composition.

Unfortunately a relevant problem occurred, affecting data reproducibility and reliability: because of the gas mix cylinder's scarce capacity and low concentration, coupled with the input pipe diameter ( 130 mm ) and the strong suction, a relevant amount of environmental air is drawn and mixed to the NO<sub>x</sub> solution, giving an exit top concentration of total NO<sub>x</sub> of only 14 ppm. The reproducibility of data was very low since during the tests the NO<sub>x</sub> concentration tended to decrease and after only five set of test the NO<sub>x</sub> mixture pressure was over. Data obtained are reported in *Fig. 42*.



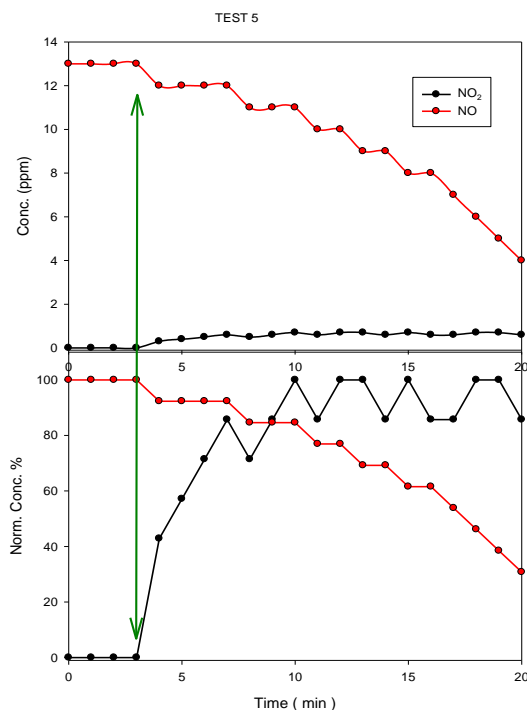


*Fig. 42- Concentration variations of NO and NO<sub>2</sub> recorded at the prototype's exhaust in response of activation/deactivation of the 254 nm UV lamp. NO and NO<sub>2</sub> concentrations are reported both as ppm concentration and normalized percentage. Green arrows indicates UV turning on, blue arrows indicates UV turning off. Five tests have been performed.*

At a first analysis it wasn't possible to achieve the desired information from this experiment, but a trend analysis in response to UV source input can anyway provide useful information. NO<sub>2</sub> concentration responded as predicted to UV source activation/deactivation: starting from a value proximal to zero in absence of UV light, quickly increase as the source was activated reaching in few minutes a plateau value and disappeared as the source was turned off again (see TEST 2,4). NO concentration values instead, gave more troubled response to experimental conditions: starting from a constant value ( reached after some minutes of equilibration ) NO quickly shows a predicted decrease as the UV source was turned on, accompanied by NO<sub>2</sub> concentration rise, but any return to the initial concentration wasn't observable as the UV source was deactivated and a continuous decrease was observed. The unique exception is observed in TEST 4, where the initial equilibration and the starting point was involving UV source turned on, and after its deactivation a weak increase in NO concentration was recorded. To explain these results it was initially hypothesized that the radical species responsible for NO depletion could persist within the reactor pipe after the source deactivation. By accurate data treatment of recorded delay

between UV activation and changing in gaseous composition it was possible to estimate the flow in 8.5-10.0 m<sup>3</sup>/hour, and the travelling time of gaseous species through the pipe section containing the catalyst between 5 and 7 seconds.

Since it seems unlikely that radical species can survive in relevant concentration in a similar range of time, the NO depletion can be more easily correlated to the pressure weakening within the cylinder. Furthermore it was estimated a value of abatement percentage performed by the catalytic system on test conditions of:

- NO = -21 % w/v
- NO<sub>2</sub> = -72 % w/v
- NO<sub>x</sub> (Mean value on homogeneous total composition) = -46%

Anyway data obtained in this set of tests shown strong oscillation due to the low NO<sub>x</sub> concentration reached in working condition in addition to the low reproducibility and stability of the experimental parameters. Furthermore the concentrations value reached and gas composition was not truly representative of the effective output of the plant process on which the photocatalytic process have to be applied.

### **3.1.7- NO<sub>x</sub> PHOTOCATALYZED ABATEMENT, FLUXING CONDITIONS** *(Experiment 4)*

Keeping in mind the data obtained and problems found in the testing phase of catalytic reactor, it was decided to modify the prototype and test it directly on the effective plant emissions. Technical details about the reactor upgrade are reported in experimental section, but the main improvements consisted in (i) an increase of the exchange catalytic surface; (ii) an increase of the UV source power; (iii) the deposition of Titanium dioxide catalyst by the heterocoagulation process on a new substrate constituted by glass pieces coming from scrap recycling path.

This last choice was inspired to one of this thesis's focal points, i.e. to obtain practical effectiveness in working application by the most affordable, sustainable and environmentally compatible chemical approach. On this basis, scrap glass become an high value solid support for

catalyst having a very low cost it provides good stability and chemical inertia, easy functionalization process and appreciable surface area ( estimated in  $6330 \text{ cm}^2 / \text{Kg}$  ). Moreover, the good refractive index value can contribute to enhance Titanium dioxide particles irradiation. Glass fiber wool adopted as support for previous prototype step was meanwhile abandoned; surely offering better surface area, it could provoke problems due to environmental release of health hazardous fibrous material.

Modified prototype was directly connected to the plant's exhaust chimney, the fan turned on and the effective gas mix produced by anodizing process let flow by, while instant analysis of gas was performed at the exit pipe of prototype. A blank sample curve have been collected with the UV source deactivated (*Fig.43*).

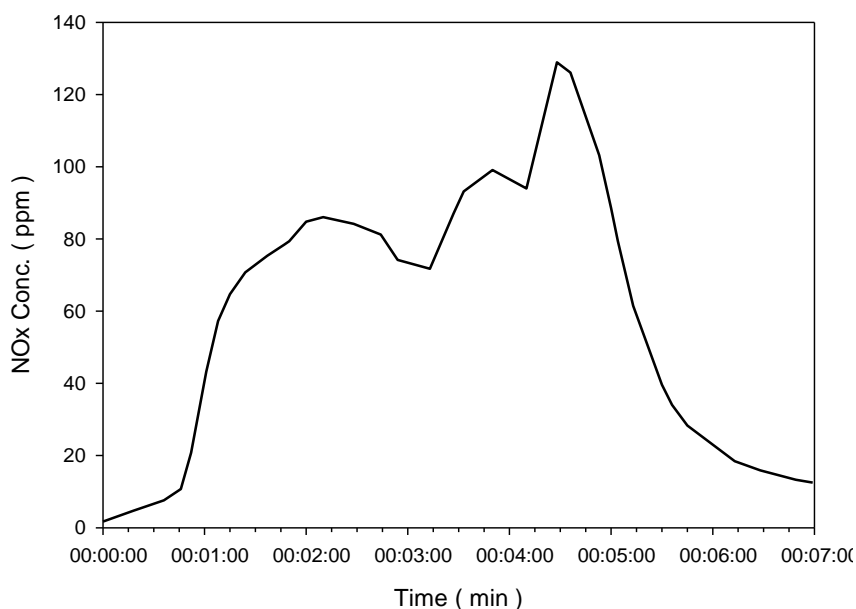


*Fig. 43 – Plant's NOx emission profile, blank curve*

The plant's production step involved in NOx formation consist in electrochemical passivation of materials within a bath containing both Sulfuric, Phosphoric and Nitric acids. The overall soaking takes four minutes, and the emission profile have been reconstructed in *Fig. 43* . A delay time is observable between the immersion procedure beginning ( time = 00.00 ) and the rise in NOx concentration due to the path within the suction system, but after that a maximum is reached at time 02:00, relatable to immersion completeness. The NOx concentration remains

at this point almost constant until a second stronger peak is reached at time 05:00, in correspondence to the extraction of material from the acidic bath. After that concentration falls out to lower values, but almost half an hour is needed to return to background level near to zero. After recording the blank emission profile, the analysis is repeated with UV source turned ON; results are reported in Fig.44 compared with blank measurement.

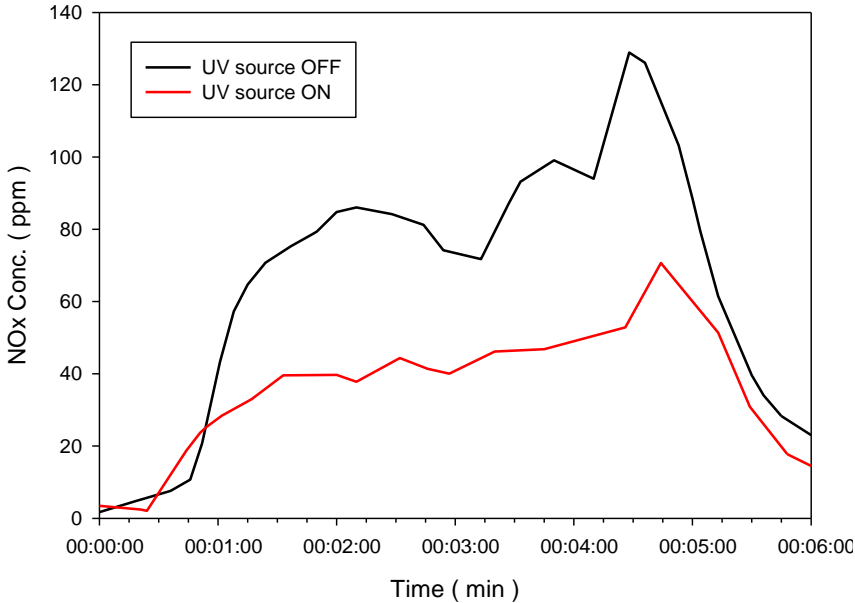


Fig. 44 - Plant's NOx emission profiles, comparison between blank emission ( black line ) and emission with working prototype ( red line )

It is clearly observable a neat reduction in NOx concentration along all test lapse, while the emission profile appears preserved except for the initial maximum, which appeared replaced by a smooth increase. Different approaches can be chosen to analyze data, i.e. by calculating the mean concentration value or comparing peak intensities or referring to total NOx emission, calculated by integrating the area below curves. The results are reported in Tab 8.

	Mean NOx conc. value (ppm)	Peak intensity (ppm)	Total NOx emission area below curve ( mg·min·m <sup>-3</sup> )
UV source OFF	60.56	128.9	23768
UV source ON	32.27	70.7	13224
% Difference	-46.7 %	-45.2 %	-44.4 %

*Tab. 8 - Plant's NOx emissions, comparison between blank and emission with working prototype. Data are reported as mean concentration, peak intensity, total emission and percentage reduction of each.*

The strong NOx abatement recorded on the whole emission profile also confirms the extrapolated value from previous fluxing tests. Despite encouraging results achieved, it was not possible to confirm data because of problems emerging from prototype handcrafted setup. In short time after the first set of measurement, acidic vapors fluxing through the system began to damage exposed electrical wiring, making UV source out of use. Also have to be mentioned that suction power performed by prototype fan revealed to be scarcely adequate to compete with the depression generated by the plant's suction system, providing low fluxing of gas through the photoreactor, potentially overestimating abatement.

### **3.1.8- NOx PHOTOCATALYZED ABATEMENT, FLUXING CONDITIONS** *(Experiment 5)*

In order to get closer to a pilot plant configuration and overcome emerged problems, a new improved prototype was built. The catalyst displacement, UV irradiation and flow were enhanced as described in experimental section.

After the connection of the prototype to the plant's exhaust chimney, abatement tests were performed. The outcoming nitrous gases from the prototype have been sampled and analyzed following the official methods reported in "estensione del decreto ministeriale 25-08-2000 all.4 comma 2 D.M. 12-07-1990" ( this method is used to verify the emission limit observance according to legislation ). A Blank test is performed with deactivated UV source, then the sampling procedure is repeated three times turning on respectively:

1. 10 UV lamps active on 10 catalytic floors;
2. 20 UV lamps active on 20 catalytic floors,
3. 30 UV lamps on 20 catalytic floors.

These variations of experimental conditions were applied to evaluate the influence of doubling the catalyst surface (1 vs 2) and increasing of irradiation intensity (2 vs 3).

The sampled solutions have been analyzed by ionic chromatography, and the results of 30 minutes sampling during each four plant's production cycles, are reported in *Tab. 9*. The nitrates amount is directly correlated to the NO<sub>x</sub> concentration in the gas phase.

	<b>Nitrates amount (mg/Nm<sup>3</sup>)</b>	<b>% Difference</b>
<b>Blank</b>	<b>17.10</b>	<b>-</b>
<b>10 UV lamp on 10 catalytic floors</b>	<b>14.80</b>	<b>-13.6 %</b>
<b>20 UV lamp on 20 catalytic floors</b>	<b>9.97</b>	<b>- 41.8 %</b>
<b>30 UV lamp on 20 catalytic floors</b>	<b>9.71</b>	<b>- 43.3 %</b>

*Tab. 9 – Nitrates concentration in samples relative to different prototype working conditions (10 UV lamps active on 10 catalytic floors, 20 UV lamps active on 20 catalytic floors, 30 UV lamps on 20 catalytic floors)*

Data obtained with the described setup are surely well representative of real working conditions. Data analysis reveals the expected increasing abatement as the number of catalytic floors is doubled since it provide an higher amount of radicals and increases the interaction time between them and the fluxing analytes. A furthermore increase in radiation intensity determines the reaching of a plateau value. This phenomenon is explainable invoking a catalyst saturation in which the further increase of the excited states population determines an increase in electron-hole recombination rate, which is in competition with radical generations. As the two processes

rate approaches each other, a limit value in catalytic efficiency is reached independently from the radiation intensity [ A. Fujishima, et al.,2000 ].

A more detailed analysis on emission profile was performed by instantaneous monitoring analyte concentration *vs* time, by a different method based on electrochemical cell analyzer. As preliminary test, a blank profile with UV lamp off is recorded , followed by activating 10 UV lamps on 10 catalytic floors and 20 UV lamps on 10 catalytic floors. NOx total emission profiles recorded are reported in *Fig. 45*. It should be underlined that differently from the previous test, 20 lamps are displaced on 10 catalytic floors allowing the evaluation of the radiation intensity doubling. The abatement amount have been then calculated as total emitted NOx, by integrating the area below curves (*Tab.10* and *Fig.46*)

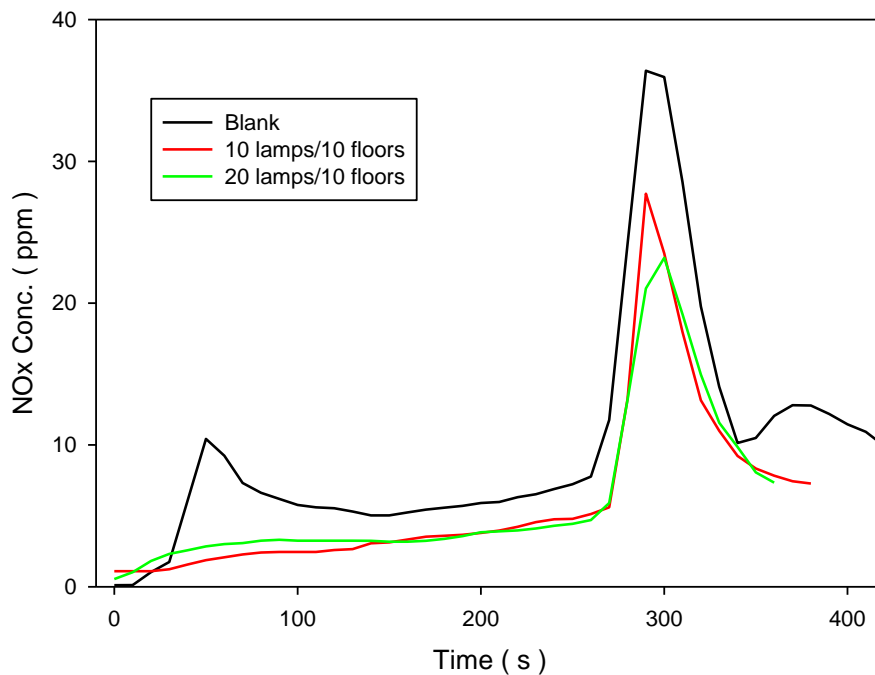
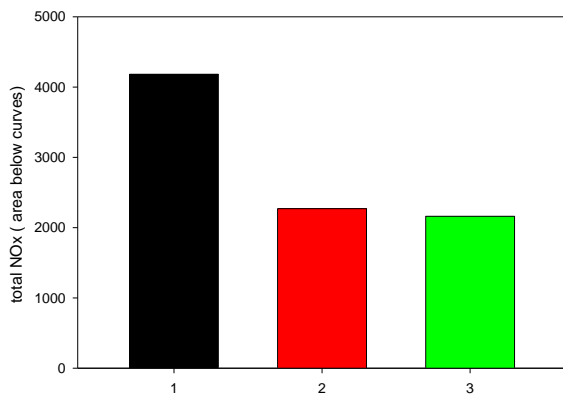


*Fig. 45 - NOx total emission profiles. Comparison between blank emission, and two different prototype's working conditions (10 UV lamps on 10 catalytic floors and 20 UV lamps on 10 catalytic floors)*



	<b>Total NOx emission area below curve ( mg·min·m<sup>-3</sup> )</b>	<b>% Difference</b>
<b>Blank</b>	<b>4181.7</b>	<b>-</b>
<b>10 lamps on 10 floors</b>	<b>2269.6</b>	<b>-45.7 %</b>
<b>20 lamps on 10 floors</b>	<b>2161.9</b>	<b>-48.3 %</b>

Fig. 46, Tab.10 – Total emitted NOx, comparison between blank emission, and two different prototype’s working conditions (10 UV lamps on 10 catalytic floors and 20 UV lamps on 10 catalytic floors)

A relevant abatement of the total NOx emission value compared to the blank test, is observed when the UV sources are activated, while a negligible enhancement of abatement is obtained by doubling the number of lamps, i.e. the radiation intensity. This observation can be again justified by a saturation of the catalyst.

Further investigations have been done on emission composition: analysis of Nitrogen monoxide and dioxide contribution to the total NOx emission reveals that the main component of the pollutant exhaust gases is NO<sub>2</sub>, as shown in Fig. 47.

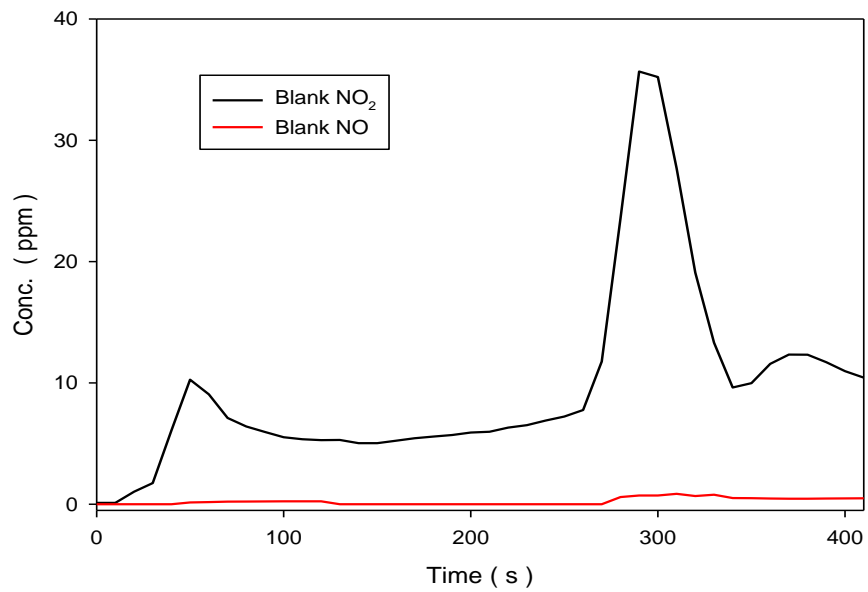


Fig. 47 - Nitrogen monoxide and dioxide contribution to the total NOx emission

Therefore, almost the completeness of measured abatement involves NO<sub>2</sub> analyte, while NO is playing a minor role; anyway the single NO profile was recorded and reported in Fig. 48.

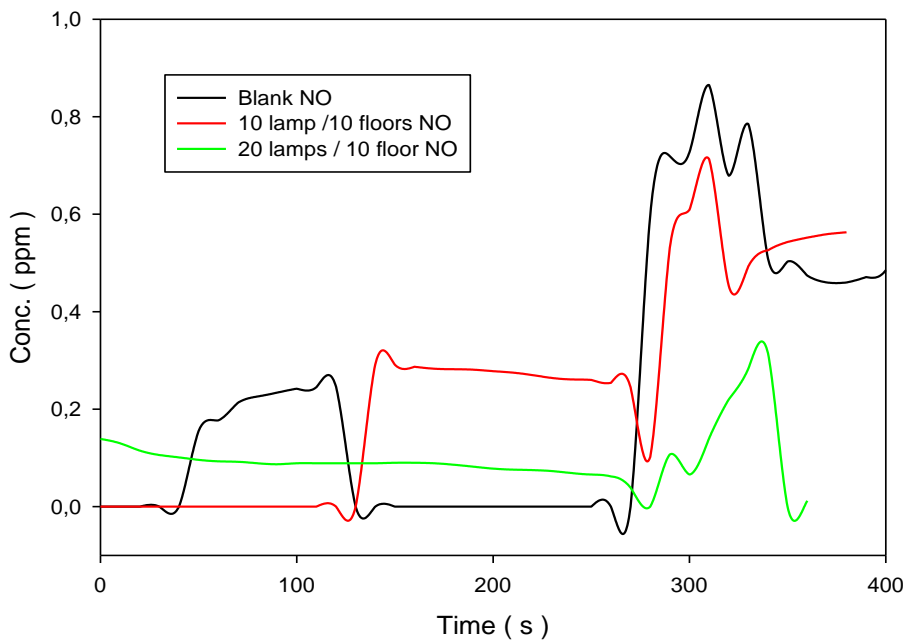
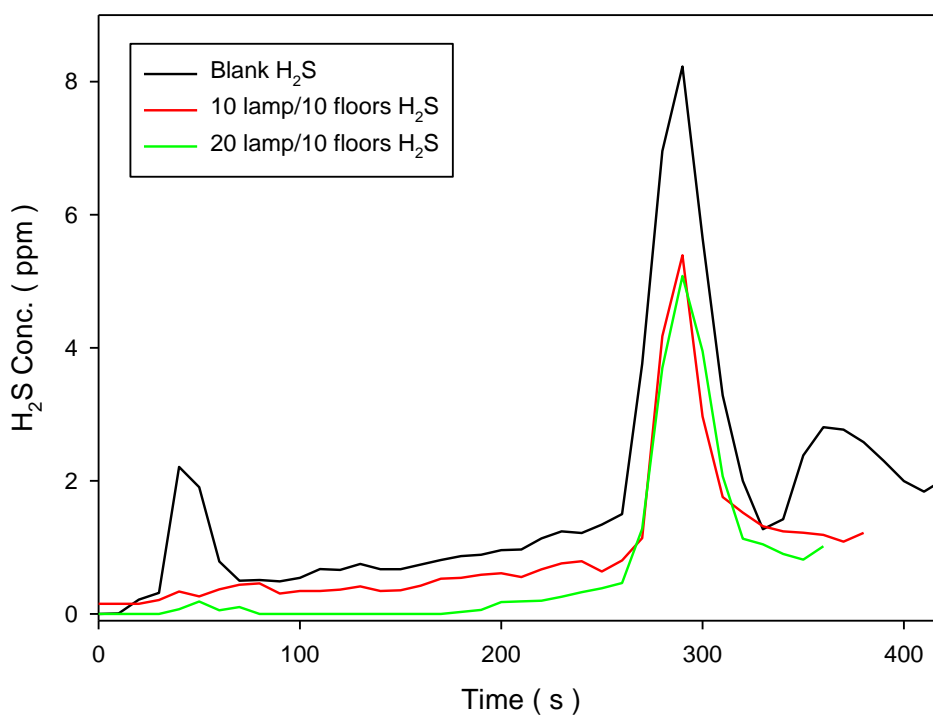


Fig. 48 - NO emission profiles. Comparison between blank emission, and two different prototype's working conditions (10 UV lamps on 10 catalytic floors and 20 UV lamps on 10 catalytic floors)

The measurement accuracy is quite affected by the low concentration values of the analytes, not far from the instrument's limit of detection. The unique appreciable phenomenon is the intensity decrease of the peak corresponding to the material extraction from acidic bath, around 300 s.

By deeply analyzing the emission composition, a third pollutant agent Hydrogen disulfide, appears in relevant concentration in correspondence of plant's production cycles. Performed tests shows the effectiveness, even higher than for NO<sub>x</sub> substrates, of the photocatalytic system also on the abatement of this compound. Emission profiles are reported in *Fig. 49*, total emission reduction data are reported in *Fig.50* and *Tab. 11*.



*Fig. 49 – H<sub>2</sub>S total emission profiles. Comparison between blank emission, and two different prototype's working conditions (10 UV lamps on 10 catalytic floors and 20 UV lamps on 10 catalytic floors)*

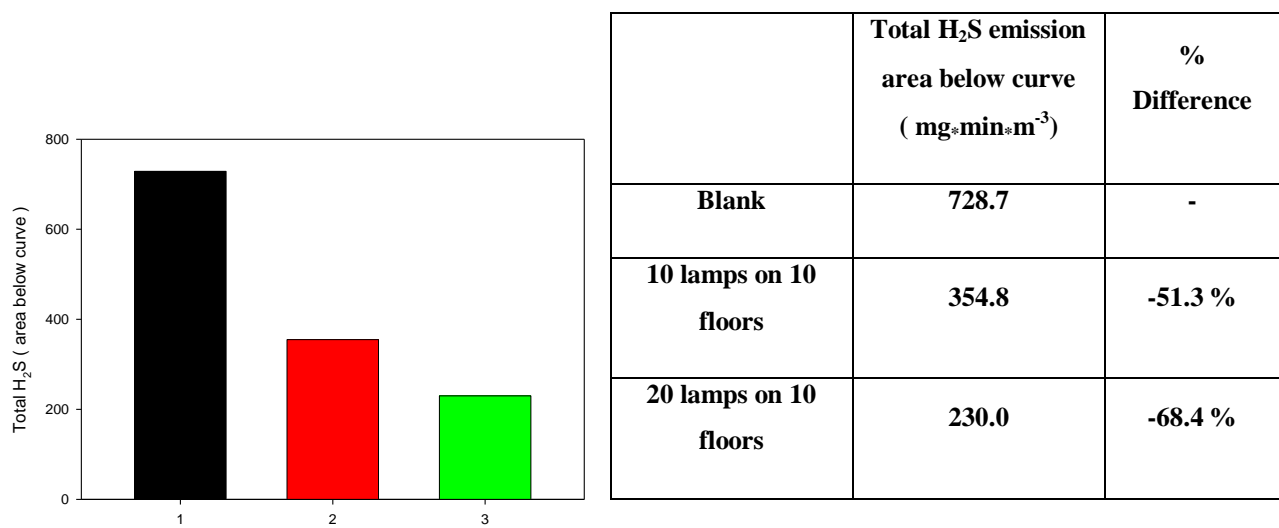


Fig. 50, Tab.11 – Total emitted H<sub>2</sub>S, comparison between blank emission, and two different prototype's working conditions (10 UV lamps on 10 catalytic floors and 20 UV lamps on 10 catalytic floors)

In this case, the increase of the radiation intensity lead to a significant contribution in the H<sub>2</sub>S abatement. This observation is not in agreement with NO<sub>x</sub> abatement results and introduce the possibility of different mechanisms involved in H<sub>2</sub>S scavenging in the case of a catalyst saturation.

### 3.1.9- PHOTOVOLTAIC PANELS COATING (*Experiment 6*)

The photocatalytic properties of Titanium dioxide previously demonstrated, have been also applied in energy harvesting field. By spray deposition of a suspension of synthesized Titanium dioxide nanoparticles, it was possible to generate radical species directly on the Silica panel's surface by sunlight activation. Through the generated radicals or directly via surface reaction with electrons and holes, a relevant reduction of deposited organic pollutant can be achieved, avoiding the loss of transmittance of the external glass covered by environmental carbonic matter and the subsequent significant decrease in panel's efficiency [J. K. Kaldellis, 2010]. Concentration and dispersion of solid Titanium dioxide particles have been tuned and the optimal application volume was determined in 5 to 10 ml of suspension per square meter, avoiding the creation an opaque scattering layer. The adhesion of nanoparticles on Silica glass surface is achieved by electrostatic attraction occurring between Titanium dioxide and Silicon dioxide at various pH, driven by opposite zeta potential values [P. Wilhelm et al., 2007]. Performed tests, described in experimental section, allowed to obtain average data related to effective efficiency gain shown by Titanium dioxide treated panels, covering one year in time. In particular two application conditions are compared: spraying after panel cleaning *vs* spraying directly on dirty panels. Data have been obtained as amount of energy produced by each panel string ( composed by 23 panels ) and compared to those obtained by reference untreated strings. Data are reported in *Tab. 12* And *Fig. 51*.

<b>Monthly kWh string production</b>	<b>String A)- Treated, Not cleaned (kWh)</b>	<b>String B)- Not cleaned (kWh)</b>	<b>String C)- Treated, Cleaned (kWh)</b>	<b>String D)- Cleaned (kWh)</b>	<b>Ratio A/B*100</b>	<b>Ratio C/D *100</b>
<b>Jan*</b>	289.01	296.80	293.02	298.81	-2.62	-1.94
<b>Feb</b>	499.60	498.98	518.72	510.22	0.12	1.67
<b>Mar</b>	698.32	694.61	721.90	707.89	0.53	1.98
<b>Apr</b>	861.56	852.38	890.80	867.32	1.08	2.71
<b>May</b>	849.80	835.85	873.66	796.80	1.67	9.65 (§)
<b>Jun</b>	956.20	943.52	972.65	949.31	1.34	2.46
<b>Jul</b>	1003.34	983.50	1023.24	997.80	2.02	2.55
<b>Aug</b>	876.48	864.037	888.10	856.40	1.44	3.70
<b>Sep</b>	673.58	669.41	685.03	667.69	0.62	2.60
<b>Oct</b>	523.02	446.62	477.85	462.34	17.11 (§)	3.35
<b>Nov</b>	178.64	335.79	346.73	333.52	-46.80 (§)	3.96
<b>Dec</b>	143.72	147.14	151.02	145.90	-2.32	3.51
<b>Jan</b>	312.37	325.73	334.17	319.00	-4.10	4.76
					<b>average</b>	<b>average</b>
* treatment data Jan, 28th				(§)=excluded data	-2.27	3.02

*Tab. 12 - Monthly string production (kWh) report for treated and untreated strings, are also reported the energy production ratios between the treated strings on the corresponding references, and relative average values.*

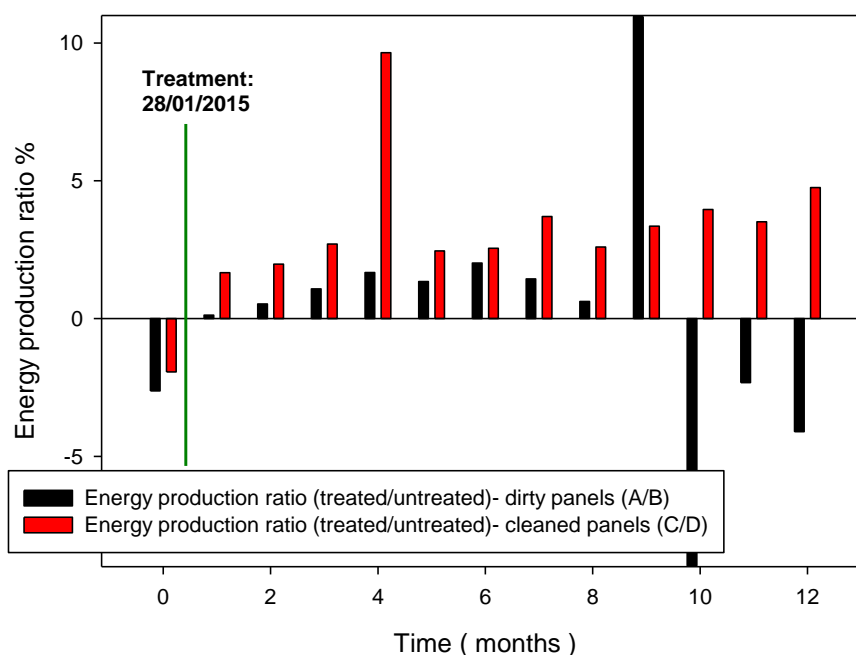


*Fig. 51 - Monthly energy production ratios between the treated strings on the corresponding references; red data are relative to the strings cleaned before  $TiO_2$  application; black data are relative to dirt strings.*

The results clearly reveal an immediate enhancement in energy production for the treated panels, A and C, compared to the untreated ones B and D. However, the gain obtained by the treated dirty panels increases for approximately 4-5 months, then starts to decrease and disappears within 8-10 months (average gain + 1.10% until September). The measurements made in October and November for dirty panels were affected by technical problems leading to unreliable data, as clearly visible in *Fig. 51*. Instead, the treatment of previously cleaned panels, results in a still growing gain after one year from the application, with an average value of +3.02%. It should be mentioned that treated strings, A and C, have been specifically chosen on the basis of their lower performances due to their intrinsic features, with respect to B and D used as reference. In fact it is clearly visible that energy production ratio before treatment had negative values (*Fig. 51*). We have no average data referred to long period before spray application, but assuming January production data as representative, the effective energy production gain can be estimated in:

- + 3.72 % for dirty treated panels ( for 7 months after application )
- + 4.96 % for clean treated panels ( after 12 months after application still growing )

The different behavior observed for dirty or cleaned treated panels can be easily explained considering that the sprayed suspension on dirty surfaces resulted in coagulation of a certain amount of Titanium dioxide nanocrystals on dust particles, slowly removed by weathering. Conversely, spray application performed on freshly cleaned Silica surface allowed to obtain weathering stable adhesion of the photocatalyst, comparable to those obtained in laboratory and previously described for many Silica supports [P. Wilhelm et al., 2007]. Therefore, Titanium dioxide coated panels maintained a constantly clean and transparent external Silica glass, while untreated reference panels began accumulating carbonic matter, as visible in *Fig. 52*, resulting in a decreasing of energy production.

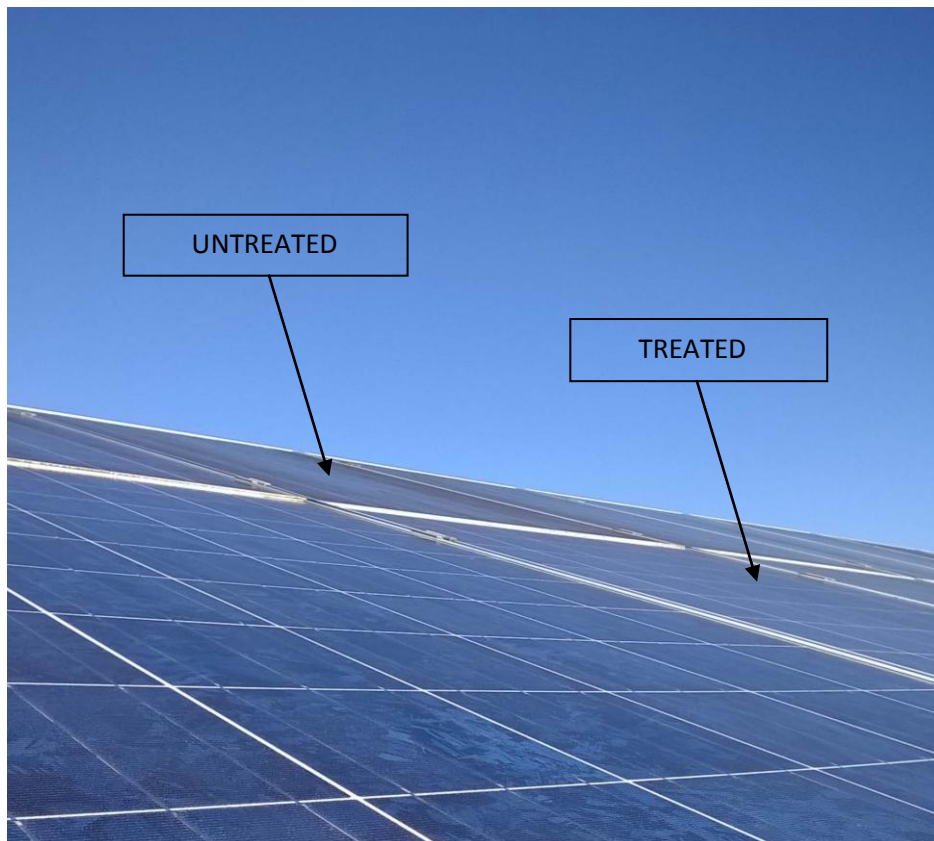


*Fig. 52 – Picture of treated and untreated panels, it is possible to see a dark halo on the untreated panel surface, while treated panels appears clean*

Despite at sea level the ultraviolet radiation represent only 2-3 % of total solar emission spectrum, the continuity of irradiation, also present in cloudy days, can guarantee sufficient radical photogeneration. By taking advantage of wavelength that in each case wouldn't be converted by panels, a relevant increase in performances can be achieved with minimal complexity of application process and environmental outgo ( example of energy production profile of treated and untreated string and hourly insolation recorded in May, 31, 2015 reported in Fig. 53).

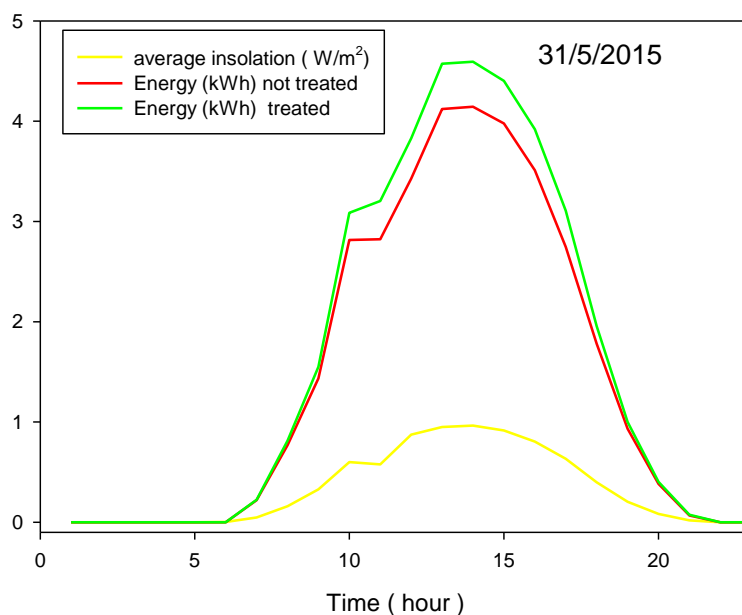


Fig. 53 - Energy production profile of treated and untreated string and hourly insolation recorded in May, 31, 2015

Although [J. K. Kaldellis et al., 2010] reported that efficiency loss due to environmental pollution can reach peaks of -6/7 % in heavily contaminated areas, the technical staff working on the photovoltaic field reported that periodic cleaning procedure of panels could practically determine a maximum of +3 % gain in efficiency, lasting no more than 2 months. Further improvements reached by Titanium dioxide application are not simply explainable by ensuring optical transmission. A further hypothesis have been made about the presence of a secondary phenomenon capable of enhance solar panels efficiency: the Near Infrared ( NIR ) backscattering reflectance. [Skoplaki et al., 2009] reported a formalization of panels efficiency in relation to working temperature:

$$\eta_c = \eta_{ref}[1 - \beta_{ref}(T_c - T_{ref})]$$

Where:

$\eta_c$  = efficiency

$\eta_{ref}$  = intrinsic efficiency of panel ( constant)

$\beta_{ref}$  = temperature coefficient ( constant )

$T_{ref}$  = 25°C

$T_c$  = working temperature

On this basis, the reported observed efficiency loss is about -0.4 % /C° in working conditions. Due to his elevate optical refractive index, Titanium dioxide is already largely used in Infrared reflective coatings ( usually paints containing crystalline Rutile form ) which can find applications such as thermal insulation in warmer regions. This kind of products anyway tends to create an opaque layer, which doesn't allow the visible light transmission. However [V. Fang et al., 2013] reported that Near Infrared reflectivity for inorganic pigments not only depends on the optical refractive index, but also on geometric data such as mean particle size, size distribution, and shape. A comparison between the NIR reflectance properties of nanocrystalline metal oxides and their macrocrystalline analogs shows that nanocrystalline matter is more reflective compared to the bulk oxides due to backscattering reflectance phenomenon shown in *Fig. 54*, also occurring in light transmitting materials.

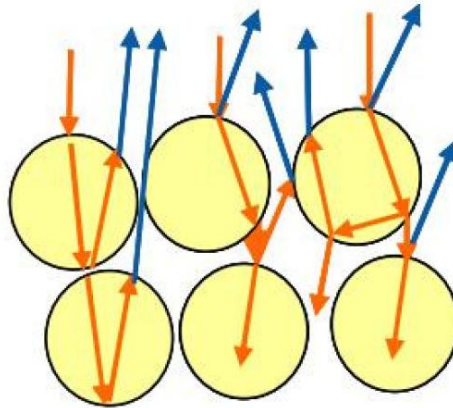


*Fig. 54 – Representation of the backscattering reflectance phenomenon produced by nanoparticles*

In addition, [V. Fang et al., 2013] reported a diffuse reflectance from 49 % to 45 % in the entire NIR range ( 700-2500 nm ) for Titanium dioxide nanoparticles in a layered structure showing minimal transmittance loss on visible light.

In conclusion, it is possible to hypothesize that beside self-cleaning properties shown by Titanium dioxide application on panels, also backscattering reflectance phenomenon take place in small extent, providing a further efficiency increase by lowering working temperature of Silicon photovoltaic junction. This hypothesis have to be demonstrated by measuring effective working temperature difference between treated and untreated panels, and by Infrared total reflectance measurements on Titanium dioxide covered glasses.

## 3.2- CALCIUM PHOSPHATES NANO-MICRO PARTICLES

### 3.2.1- CHARACTERIZATION OF CALCIUM PHOSPHATES

#### 3.2.1.1- HYDROXYAPATITE CHARACTERIZATION (*Synthesis 4*)

Hydroxyapatite suspension obtained by the neutralization synthesis (*Synthesis 4*) described in Experimental section, appears as a bright white dense liquid, quite stable to sedimentation, with a dry solid residue measured in 6.7 % weight. Suspension and solid phase have been characterized in order to evaluate the chemical-physical parameters.

- **X-ray powder diffraction Characterization**

X-ray diffraction pattern obtained by the dried Calcium Phosphate ( *Fig. 55* ) reveals peaks confirming the crystalline features of the solid product.

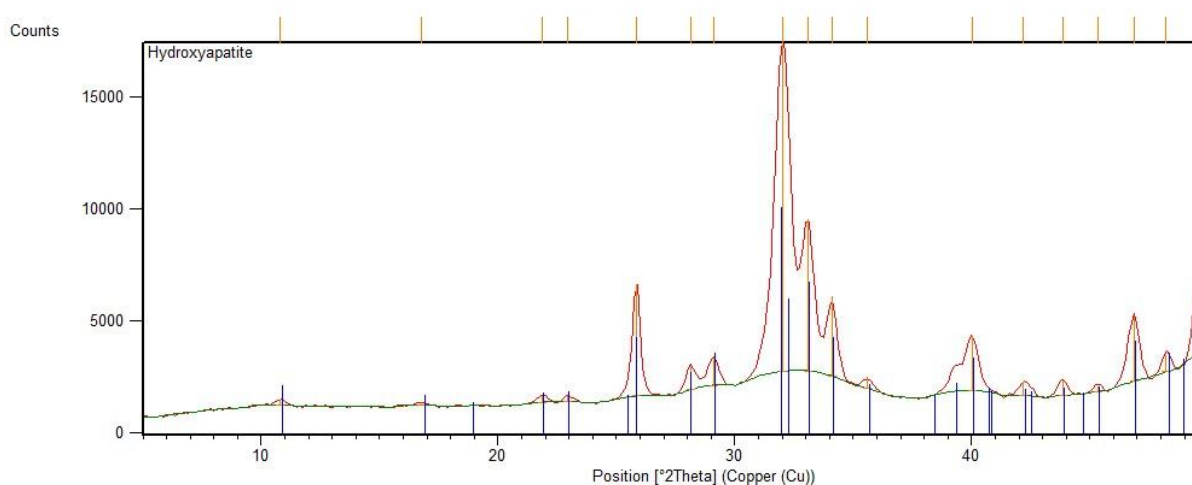


*Fig. 55 – Experimental X ray diffraction pattern of the dried product of Synthesis 4 with peak position of reference pattern.*

By comparing reflection peaks position and relative intensity to ICSD database it was possible to identify the crystalline Hydroxylapatite as a single constituent. (reference ICSD codes: 01-086-0740). It is noticeable that all peaks appears quite broadened possibly for the small

dimensions of diffracting crystallites, characterized by a higher ratio of less-ordered and defective border matter to well crystalline bulk. By referring to Sherrer's equation it was possible to calculate an approximate dimension of diffracting crystallites. However, this last formula can underestimate the particle size calculated value since it consider the crystallites dimensions as unique contribution to the peak broadening. The shape factor is assumed equal to 0.9 commonly used as a mean value assigned to unknown shaped crystallites.

CRYSTAL SIZE ( <i>Sherrer formula</i> )		
Wavelength Cu Ka ( $\text{\AA}$ )	1.541874	
Shape factor	0.9	
Bragg's angle ( $2\theta$ °)	32.025	
Amp. $1/2 h$ ( $2\theta$ °)	0.492	
Crystallite size approx. (nm)		33.6

*Tab. 13 - Parameters and crystal size calculation of the dried product of Synthesis 4 with Sherrer's formula*

- **Scanning Electron Microscopy (SEM) morphological characterization**

Dried Hydroxyapatite powders have been morphologically investigated by SEM imaging. Obtained images are reported ( *Fig. 56* ). Fluffy aggregates of various dimensions are visible, also under 1  $\mu\text{m}$  in size. Little dimensions, surface roughness and apparent low compactness of the material seems promising about its surface area-related properties.

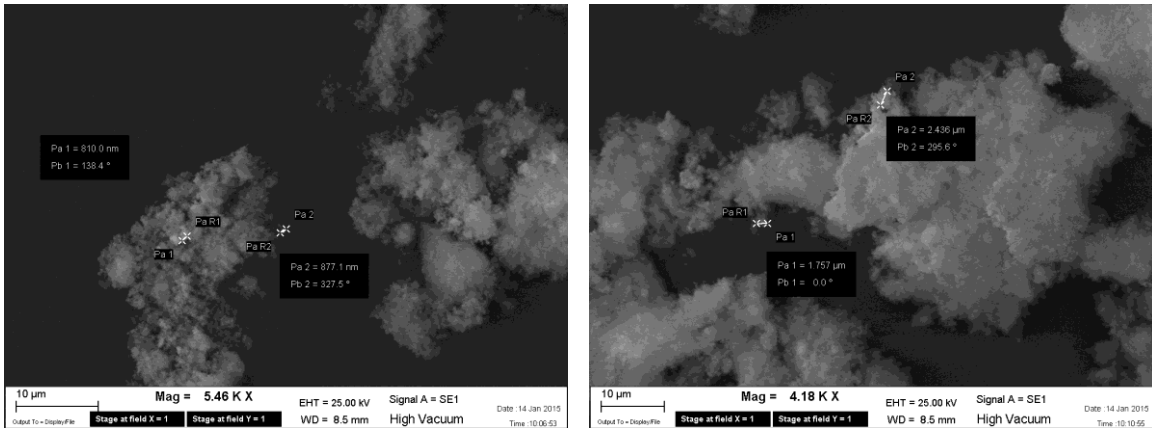


Fig. 56 – SEM images of the dried product of Synthesis 4

- **DLS size measurement**

Since a strong aggregation have been observed in dried samples, DLS measurement have been performed to achieve information about the aggregation state on liquid suspension without applying a forced drying.

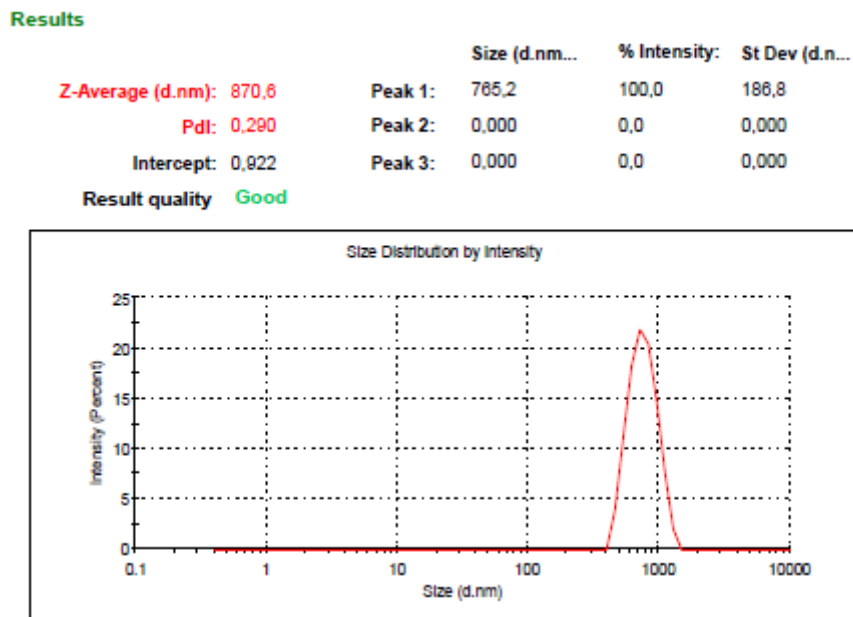


Fig. 57 – DLS size measurement report of the product of Synthesis 4 dispersed in water

The results indicates the presence of sub-micrometric particles in suspension, with an average diameter of 870 nm and a peak value of 752 nm, showing a quite limited size distribution ( poly dispersion index= 0.29 ).

- **BET surface area measurement**

Results, reported in *Tab. 14*, shows a noticeable value of 105.9 m<sup>2</sup>/g for the specific surface area. The data is accompanied by quality analysis parameters indicating a very good linearity of experimental points and the correct response of sample to the technique. C constant value gives an indication of the force of the adsorbent/adsorbate interactions. Despite this parameter cannot be used to calculate quantitatively adsorption Enthalpy, it can give anyway further information. In fact, C constant values higher than 200 may indicate the presence of porosity in the sample [ISO 9277, 2010].

<b>Multi-Point BET</b>					
<b>Data Reduction Parameters Data</b>					
<u>Adsorbate</u>	Nitrogen	Temperature	77.350K	Liquid Density:	0.808 g/cc
	Molec. Wt.: 28.013	Cross Section:	16.200 Å <sup>2</sup>		
<b>Multi-Point BET Data</b>					
Relative Pressure [P/Po]	Volume @ STP [cc/g]	1 / [ W((Po/P) - 1) ]	Relative Pressure [P/Po]	Volume @ STP [cc/g]	1 / [ W((Po/P) - 1) ]
7.77720e-02	25.4550	2.6507e+00	1.99279e-01	30.2905	6.5739e+00
8.42530e-02	25.7363	2.8603e+00	2.22206e-01	31.1762	7.3319e+00
1.04583e-01	26.6067	3.5123e+00	2.48632e-01	32.2253	8.2160e+00
1.29004e-01	27.5914	4.2950e+00	2.73579e-01	33.2625	9.0592e+00
1.48282e-01	28.3698	4.9101e+00	2.97118e-01	34.2154	9.8850e+00
1.76899e-01	29.4841	5.8322e+00			
<b>BET summary</b>					
	Slope =	32.834			
	Intercept =	6.546e-02			
	Correlation coefficient, r =	0.999914			
	C constant =	502.565			
	Surface Area =	105.855 m <sup>2</sup> /g			

*Tab. 14 – Report of the BET surface area measurement of the dried product of Synthesis 4*

### 3.2.1.2- BRUSHITE CHARACTERIZATION (*Synthesis 5*)

Brushite suspension obtained by reported synthesis ( *Synthesis 5-9* ) appears as a white liquid, not stable to sedimentation, which occurs in few minutes. Suspension and solid phase have been characterized in order to evaluate chemical-physical parameters

- **X-ray powder diffraction Characterization**

X ray diffraction pattern obtained from dried Calcium Phosphate ( Fig. 58 ) reveals peaks confirming crystalline features of the solid product.

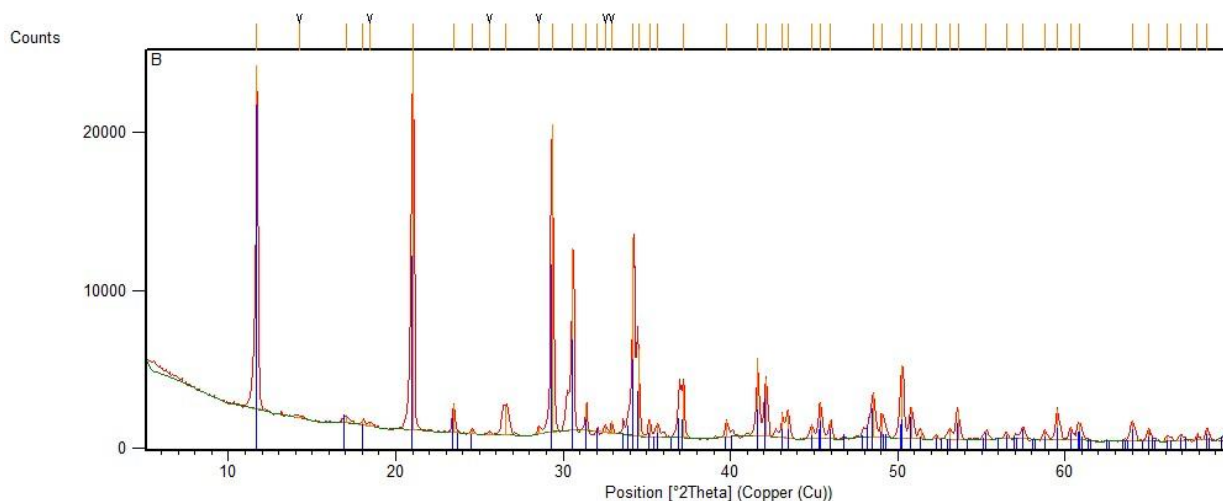


*Fig. 58 – Experimental X ray diffraction pattern of the dried product of Synthesis 5 with peak position of reference pattern.*

By comparing the reflection peak position and relative intensity to ICSD database it was possible to identify crystalline Brushite as a single constituent (reference ICSD codes: 01-072-1240 ) apart from residual peaks attributable to Quartz sample holder. It is noticeable that all peaks appears sharp and narrow, suggesting the presence of large crystalline domains.

- **Scanning Electron Microscopy (SEM) morphological characterization**

SEM images ( *Fig. 59* ) confirmed the large dimensions of crystals composing the solid powder estimated as ranging between 20  $\mu\text{m}$  to 50  $\mu\text{m}$ .

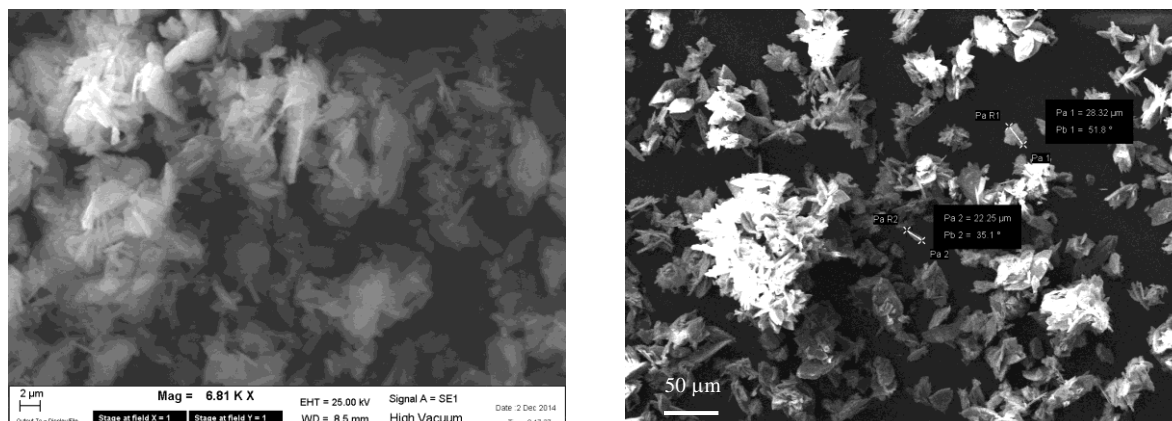


*Fig. 59* – SEM images of the dried product of Synthesis 5

Characterization analysis reveals that this product is not interesting for our applications, due to its average size and crystalline features.

### 3.2.1.3- BRUSHITE CHARACTERIZATION (*Synthesis 6* )

- **X-ray powder diffraction Characterization**

X ray diffraction pattern obtained from dried Calcium Phosphate ( *Fig. 60* ) reveals to be poorly crystalline Hydroxylapatite instead of desired Brushite phase. Reference Hydroxylapatite peaks are reported for comparison (ICSD codes: 01-086-0740 ).

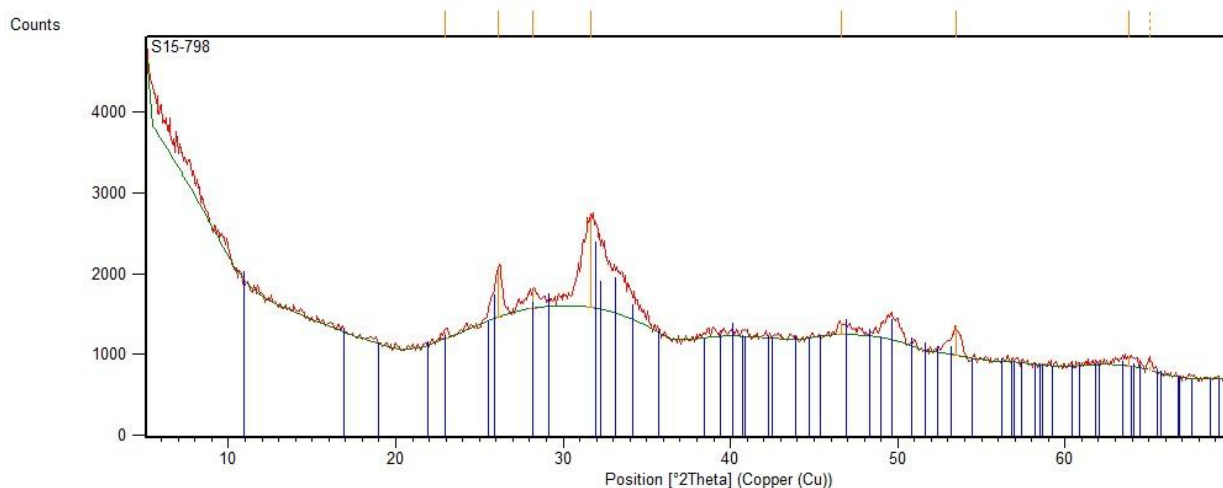


Fig. 60 – Experimental X ray diffraction pattern of the dried product of Synthesis 6 with peak position of reference pattern.

Even if potentially interesting in bone regenerative fields, this product have been considered not suitable for the purposes of this thesis work.

- **Scanning Electron Microscopy (SEM) morphological characterization**

SEM images obtained by dried product of *Synthesis 6* reveals much interesting aggregates of sub-micrometric particles. Aggregates shows variable dimensions from 1  $\mu\text{m}$  to 20  $\mu\text{m}$ , but it is not possible to define the dimensions of the particles composing them.

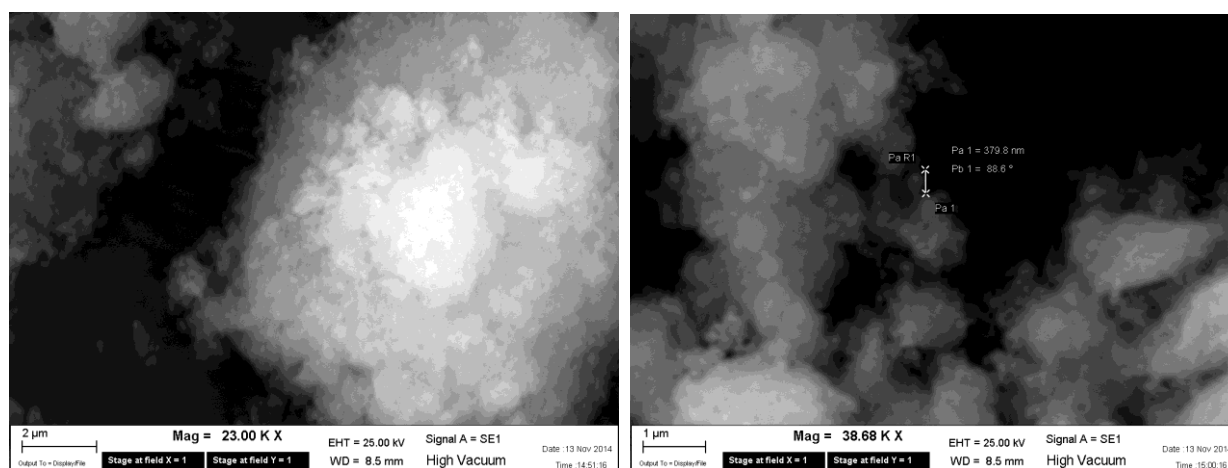


Fig. 61 – SEM images of the dried product of Synthesis 6

### 3.2.1.4- BRUSHITE CHARACTERIZATION (*Synthesis 7* )

Obtaining sub-micrometric Brushite crystals in easy experimental conditions without adding capping or stabilizing agents reveals to be quite challenging. An attempt to promote the crystallization of Brushite phase is made by modifying the synthesis reported in [Patent WO 2005/082780 MENARINI] through the addition of Magnesium 1/3 molar ratio in respect to Calcium, even if Hydroxyapatite formation should be favoured by the pH range of reaction mixture. The  $Mg^{++}$  ion is known to compete for  $Ca^{++}$  sites in apatitic structure, and at high concentrations, this process destabilizes the growing apatitic phase, leading to precipitation of Brushite.

- **X-ray powder diffraction Characterization**

X ray diffraction pattern obtained by dried Calcium Phosphate ( *Fig. 62* ) reveals sharp crystalline peaks. By comparing reflection peaks position and relative intensity to ICSD database it was possible to identify crystalline Brushite as main constituent, but residue analysis shows a minor presence of Hydroxyapatite. It is also visible a strong intensity enhancement of peak appearing at  $2\Theta = 11.6^\circ$  , corresponding to the (020) plane reflection. Enhancement of this reflection compared to other peaks may indicate a preferential axis growth of crystals in reported conditions.

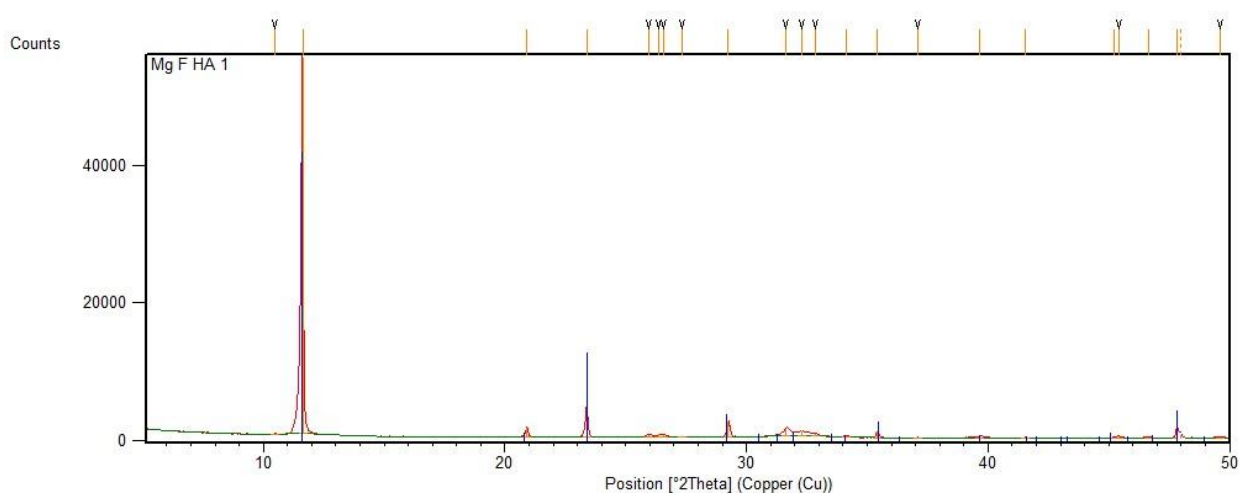


*Fig. 62– Experimental X ray diffraction pattern of the dried product of Synthesis 7 with peak position of reference pattern.*

- **Scanning Electron Microscopy (SEM) morphological characterization**

SEM images obtained from dried sample ( reported in *Fig. 63* ) reveals large scale-shaped crystals, showing average face dimension in the 10 micrometer scale. This product have been considered not interesting for the purposes of this thesis work.

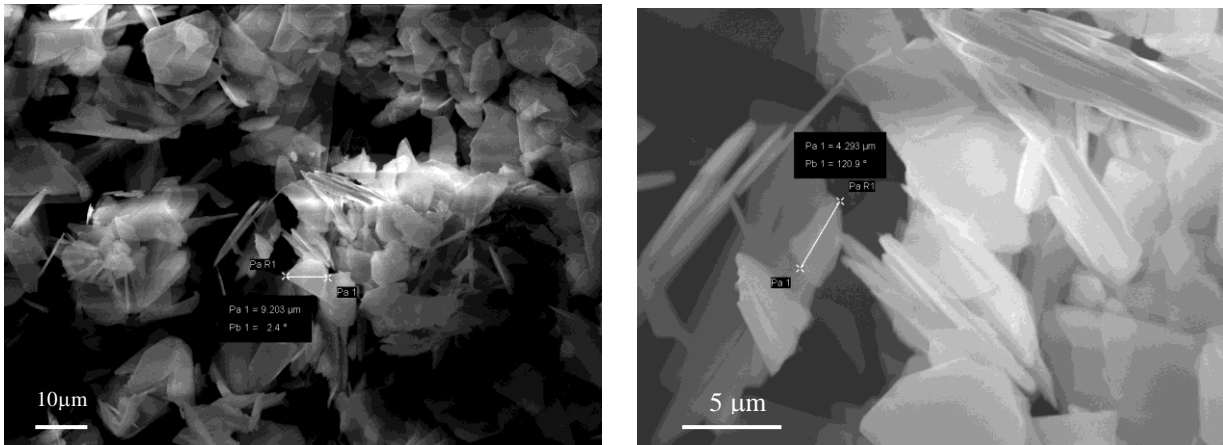


*Fig. 63 – SEM images of the dried product of Synthesis 7*

### 3.2.1.5- BRUSHITE CHARACTERIZATION (*Synthesis 8* )

- **X-ray powder diffraction Characterization**

X ray diffraction pattern obtained by dried Calcium Phosphate ( *Fig. 64* ) confirms the only presence of crystalline Brushite (reference ICSD codes: 01-072-1240 ), apart from residual peaks attributable to Quartz sample holder.

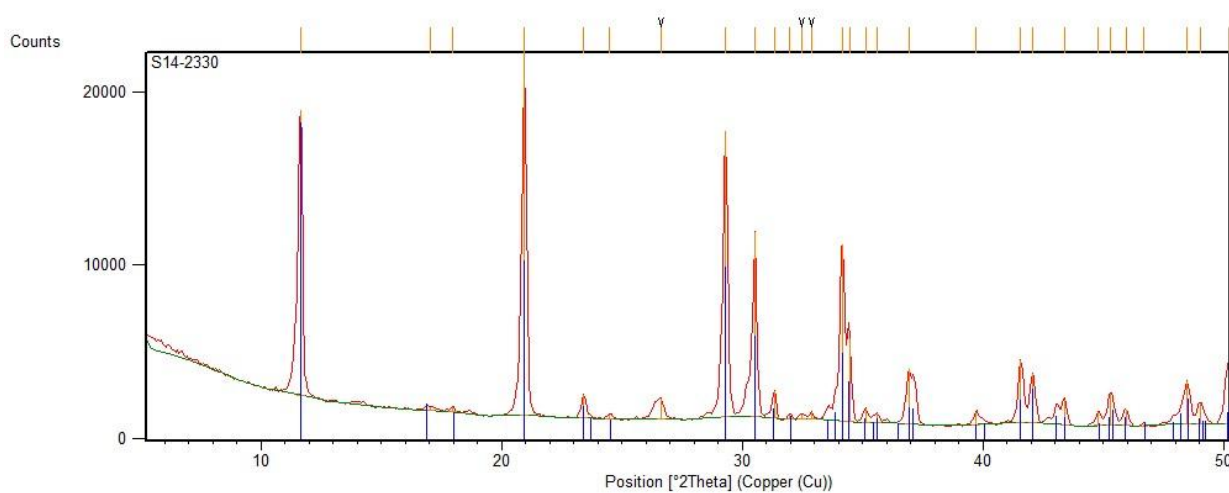


*Fig. 64 – Experimental X ray diffraction pattern of the dried product of Synthesis 8 with peak position of reference pattern.*

- **Scanning Electron Microscopy (SEM) morphological characterization**

SEM images ( reported in *Fig. 65* ) shows the presence of fluffy aggregates of sub-micrometric particles ranging from 100 to 700 nm. Particle matter seems to have crystalline sharp shapes, but instrument resolution doesn't allow to acquire defined images.

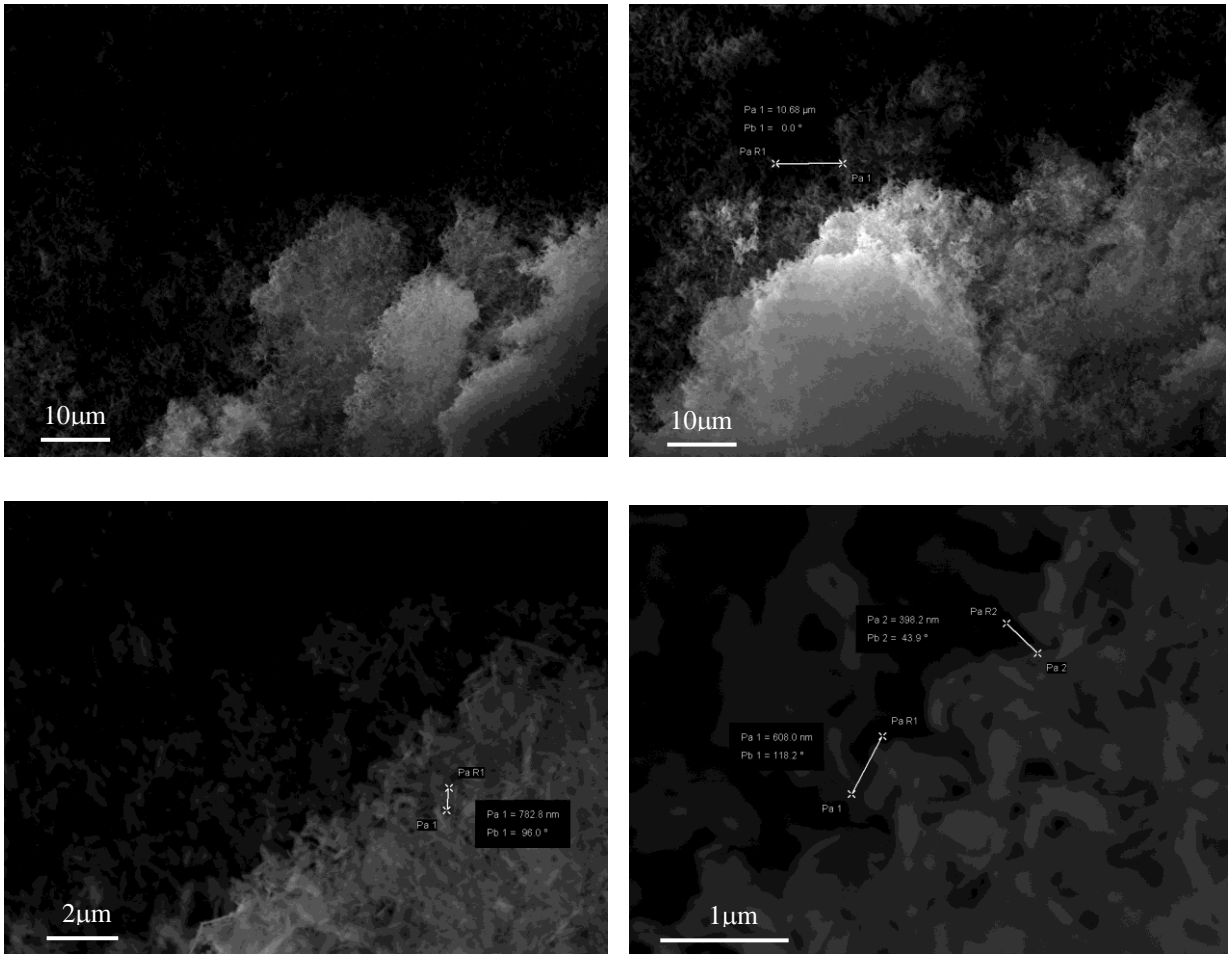


*Fig. 65 – SEM images of the dried product of Synthesis 8*

In any case morphology shown by obtained Brushite crystals indicates a probable high surface area and seems interesting for the purposes of this thesis work.

- **DLS size measurement**

Even if affected by strong precipitation phenomena, determining a low quality of the results, DLS measurement provided a confirmation of particles average sizes observed in SEM images. The data are reported in *Fig. 66* and indicate the presence in solution of two main populations of particles with hydrodynamic diameters of 317.3 nm and 809.3 nm, respectively.

## Results

	Size (d.nm)	% Intensity	St Dev (d.nm)	
Z-Average (d.nm):	1157	Peak 1: 317,3	62,0	43,28
PdI: 0,707	Peak 2: 809,3	33,9	107,2	
Intercept: 0,966	Peak 3: 1315	4,1	137,7	

Result quality Refer to quality report

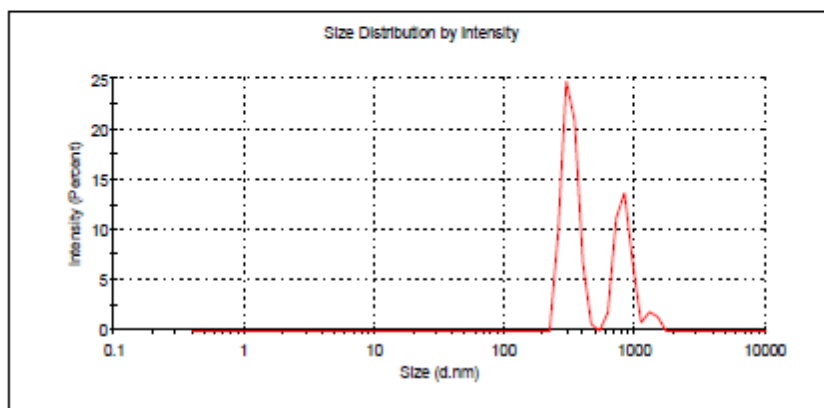


Fig. 66 – DLS size measurement report of the product of Synthesis 8 dispersed in water

### 3.2.1.6- BRUSHITE CHARACTERIZATION (*Synthesis 9* )

*Synthesis 9* have been performed as part of a work concerning the use of Hydroxylapatite as consolidative material in conservation of cultural heritage [Sassoni et al., submitted ]. Hydroxylapatite is formed by a metathesis reaction between  $\text{CaCO}_3$  contained in Marble and  $(\text{NH}_4)_2\text{HPO}_4$  delivered as injectable water solution. By delivering  $\text{KH}_2\text{PO}_4$ , the formation of Brushite instead of Hydroxylapatite have been tested in order to produce Calcium phosphates stable in a wider pH range with respect to hydroxyapatite.

#### • X-ray powder diffraction Characterization

X ray diffraction pattern obtained by dried powders ( reported if *Fig. 67* ) reveals the effective formation of Brushite crystal phase. Peaks attributable to unreacted Mg containing  $\text{CaCO}_3$ , ( Marble ) and  $\text{CaO}$  , approximately 5 % w/w, are also present, whereas any peak related to unreacted  $\text{KH}_2\text{PO}_4$  could be observed (reference ICSD codes: 01-072-1240 for Brushite, 01-089-1306 for  $\text{CaCO}_3$ , Mg, 00-048-1467 for  $\text{CaO}$  ).

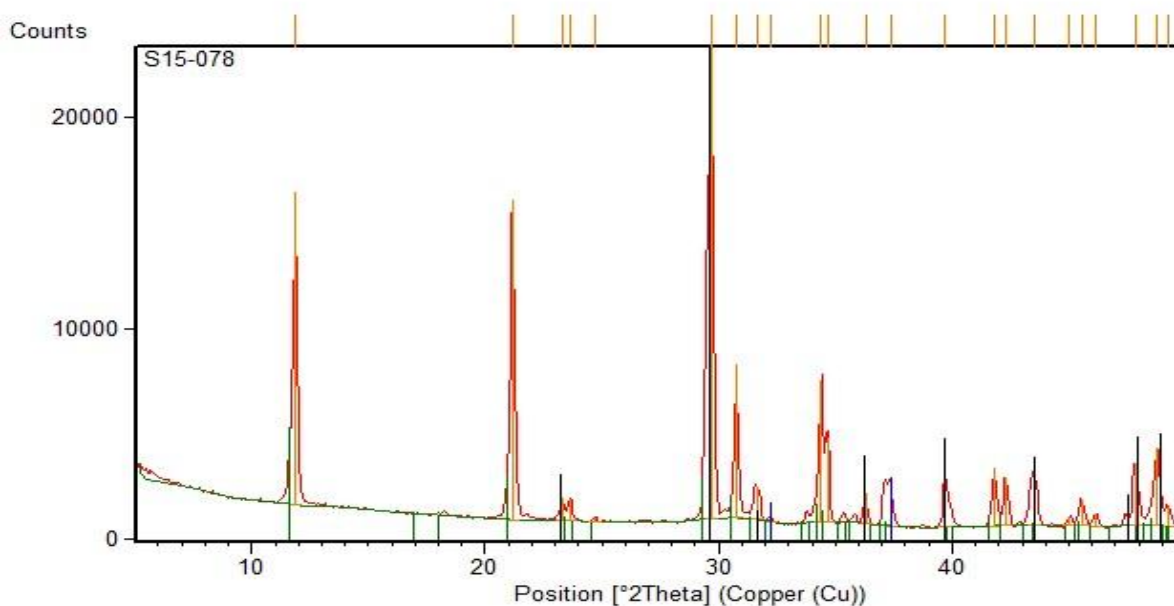


Fig. 67 – Experimental X ray diffraction pattern of the dried product of Synthesis 9 with peak position of reference pattern.

### 3.2.1.7- MONETITE CHARACTERIZATION (*Synthesis 10* )

Monetite suspension obtained by reported synthesis ( *Synthesis 10-12* ) appears as a white liquid, not stable to sedimentation, which occurs in few minutes. Suspension and solid phase have been characterized in order to evaluate chemical-physical parameters.

- **X-ray powder diffraction Characterization**

X ray diffraction pattern produced by dried powders ( reported if *Fig.68* ) confirms the effective formation of Monetite as unique crystalline phase. Peaks appear quite broadened suggesting the presence of small diffracting crystallites ( reference ICSD codes:01-071-1759 ).

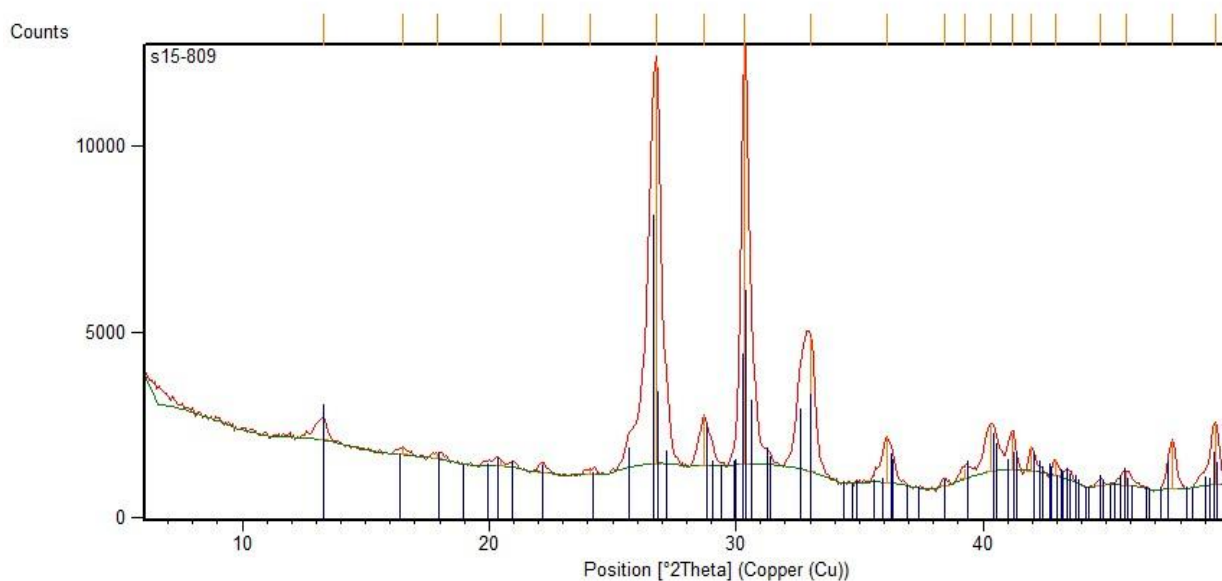


Fig. 68 – Experimental X ray diffraction pattern of the dried product of Synthesis 10 with peak position of reference pattern.

- **Scanning Electron Microscopy (SEM) morphological characterization**

SEM images ( reported in Fig. 69 ) shows micrometric aggregates of smal needle-like particles, with the length of approximately 1  $\mu\text{m}$ . Morphology and dimensions shown by obtained Monetite are interesting for the purposes or applications of this thesis work.

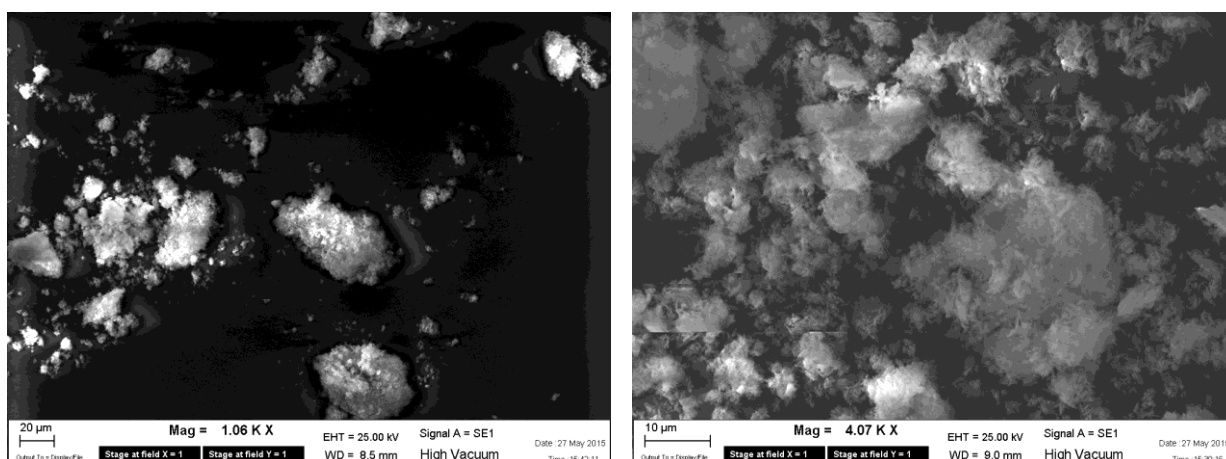


Fig. 69 – SEM images of the dried product of Synthesis 10

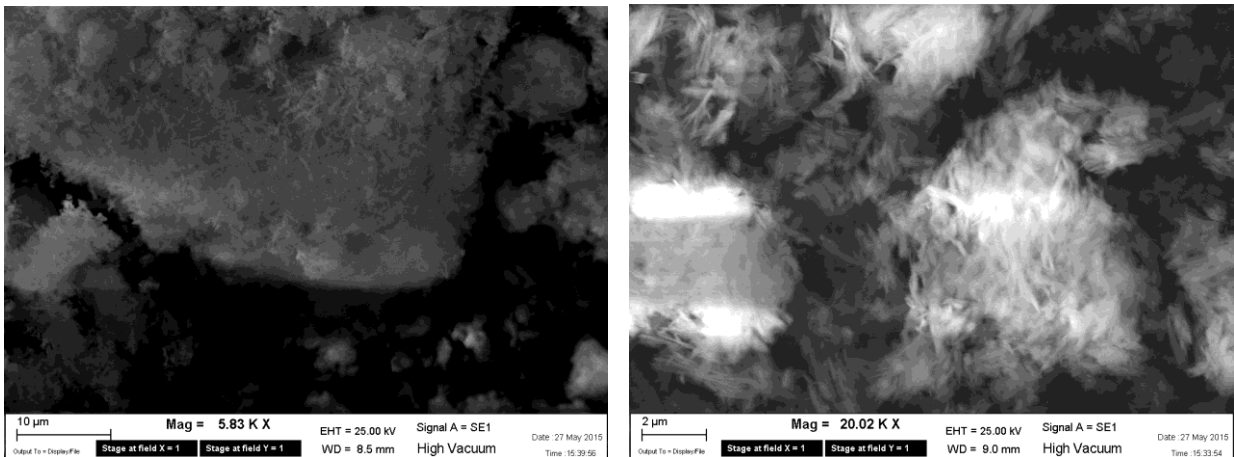


Fig. 69 – SEM images of the dried product of Synthesis 10

- **DLS size measurement**

Fast precipitation phenomenon occurring in Monetite suspension determined a failure in DLS measurements.

### 3.2.1.8- MONETITE CHARACTERIZATION ( *Synthesis 11* )

- **X-ray powder diffraction Characterization**

X ray diffraction pattern produced by dried powders ( reported if *Fig.70* ) confirms the effective formation of Monetite as unique crystalline phase ( reference ICSD codes:01-071-1759 ).

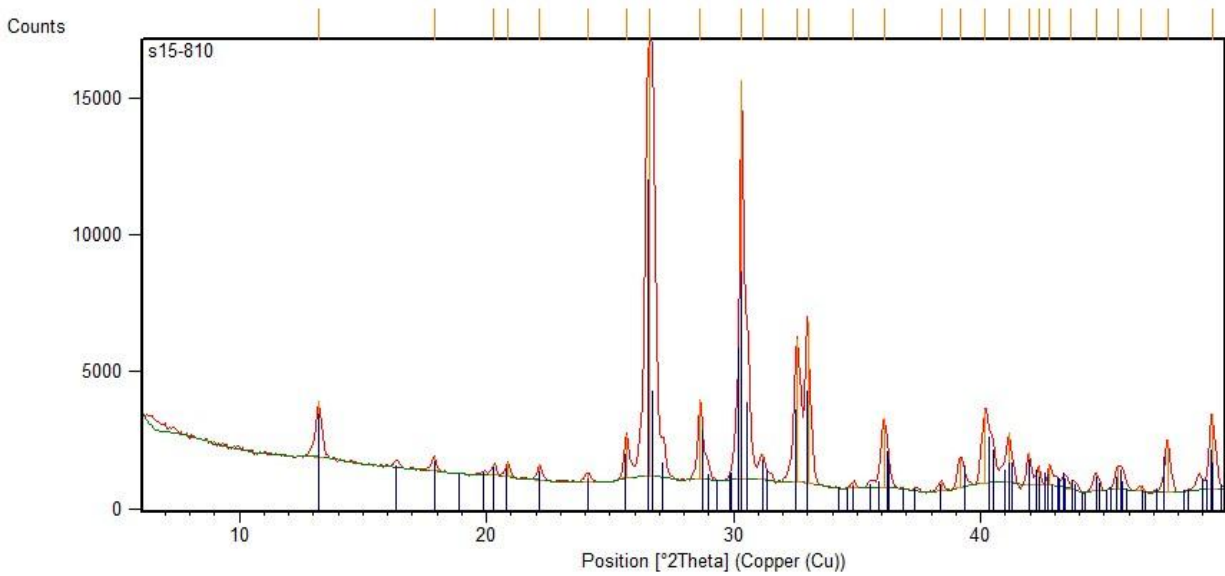


Fig. 70– Experimental X ray diffraction pattern of the dried product of Synthesis 11 with peak position of reference pattern.

- **Scanning Electron Microscopy (SEM) morphological characterization**

SEM images ( reported in Fig.71 ) shows micrometric aggregates of small irregular particles with dimensions below 1  $\mu\text{m}$ . Morphology and dimensions shown by obtained Monetite are interesting for the purposes of this thesis work.

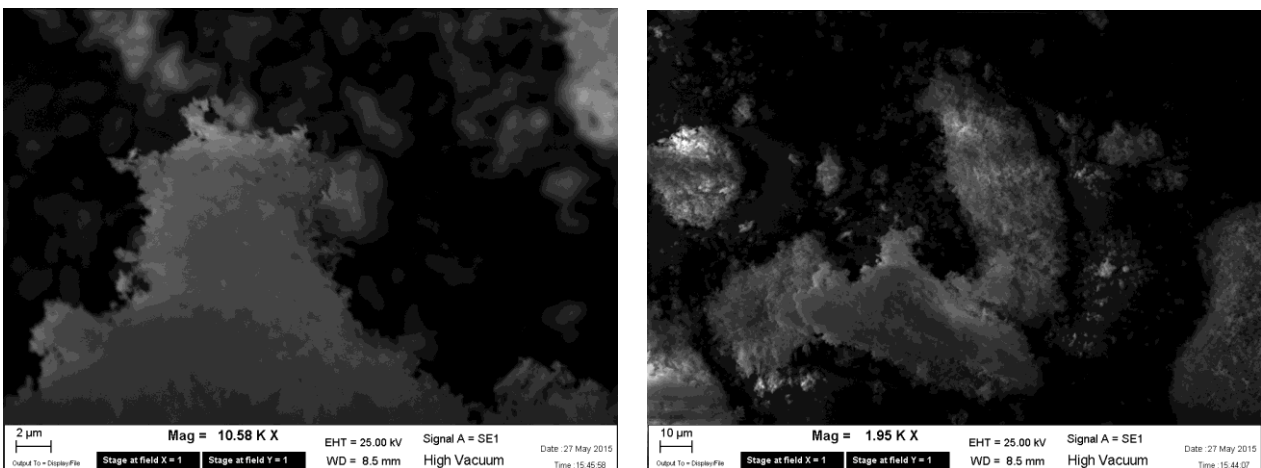


Fig. 71 – SEM images of the dried product of Synthesis 11

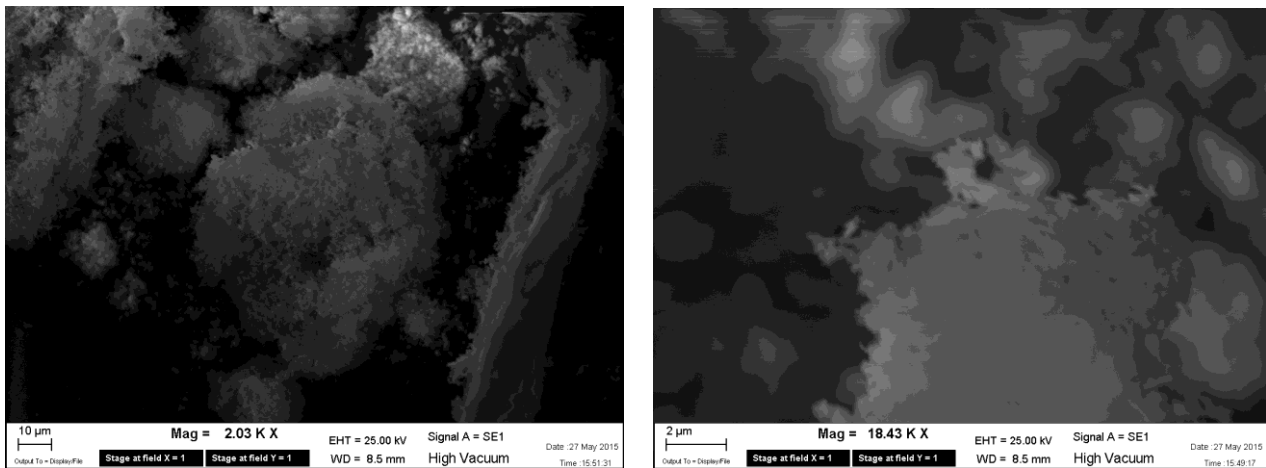


Fig. 71 – SEM images of the dried product of Synthesis 11

- **DLS size measurement**

Again, precipitation phenomena occurring in Monetite suspension determined a failure in DLS measurements.

### 3.2.1.9- MONETITE CHARACTERIZATION ( *Synthesis 12* )

- **X-ray powder diffraction Characterization**

X ray diffraction pattern obtained by dried powders ( reported if *Fig.72* ) confirms the effective formation of Monetite as a single crystalline phase ( reference ICSD codes:01-071-1759 ).

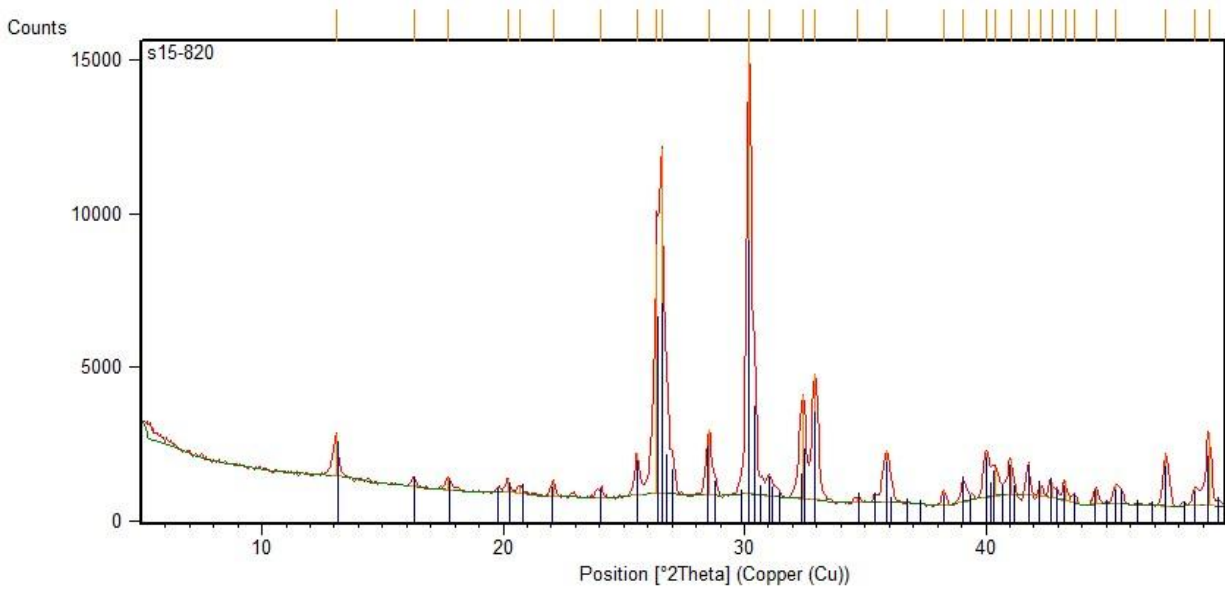


Fig. 72 – Experimental X ray diffraction pattern of the dried product of Synthesis 12 with peak position of reference pattern.

- **Scanning Electron Microscopy (SEM) morphological characterization**

SEM images ( reported in Fig. 73 ) shows rounded aggregates with dimensions ranging between 1 and 10  $\mu\text{m}$  . From the observation, it is not possible to identify regular small particles like in previous Monetite synthesis. Morphology and dimensions shown by obtained Monetite are anyway interesting.

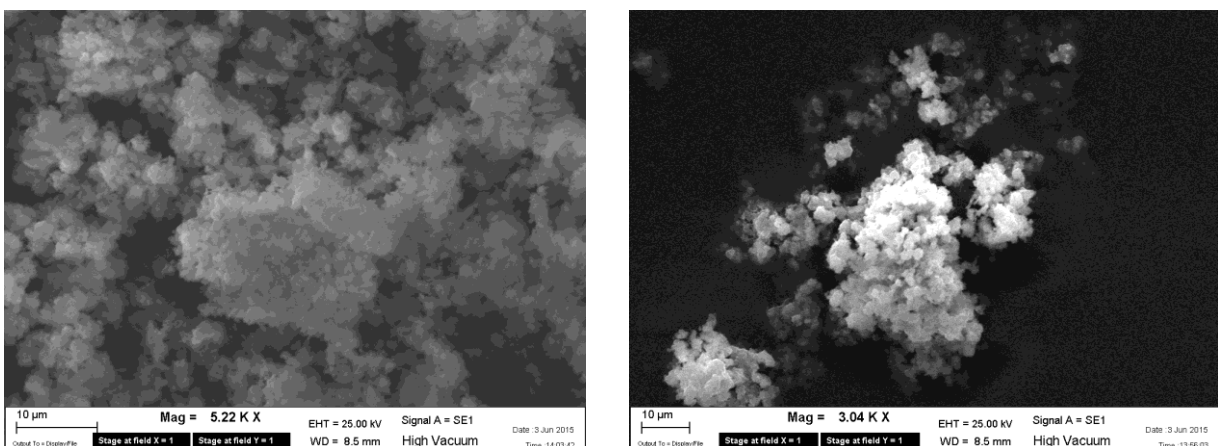


Fig. 73 – SEM images of the dried product of Synthesis 12

### 3.2.1.10- $\beta$ -TRICALCIUM PHOSPHATE CHARACTERIZATION ( *Synthesis 13-14* )

Both solid state synthesis produced white powder samples having an almost identical morphology and a superimposable XRPD pattern. Therefore only the data obtained from *synthesis 14* are reported.

- **X-ray powder diffraction Characterization**

X ray diffraction pattern obtained by grounded powders ( reported if *Fig.74* ) confirms the effective formation of  $\beta$ -Tricalcium phosphate as main constituent phase. Residual analysis shows the presence of Dicalcium Phosphate as secondary phase, estimated in 10-15 % weight by RIR evaluation.  $\beta$ -Tricalcium phosphate peaks well match the calculated profile of both pure and Mg substituted Tricalcium phosphate (reference ICSD codes: 01-077-0692 for  $\beta$ -Tricalcium phosphate, 01-071-2123 for Dicalcium phosphate ).

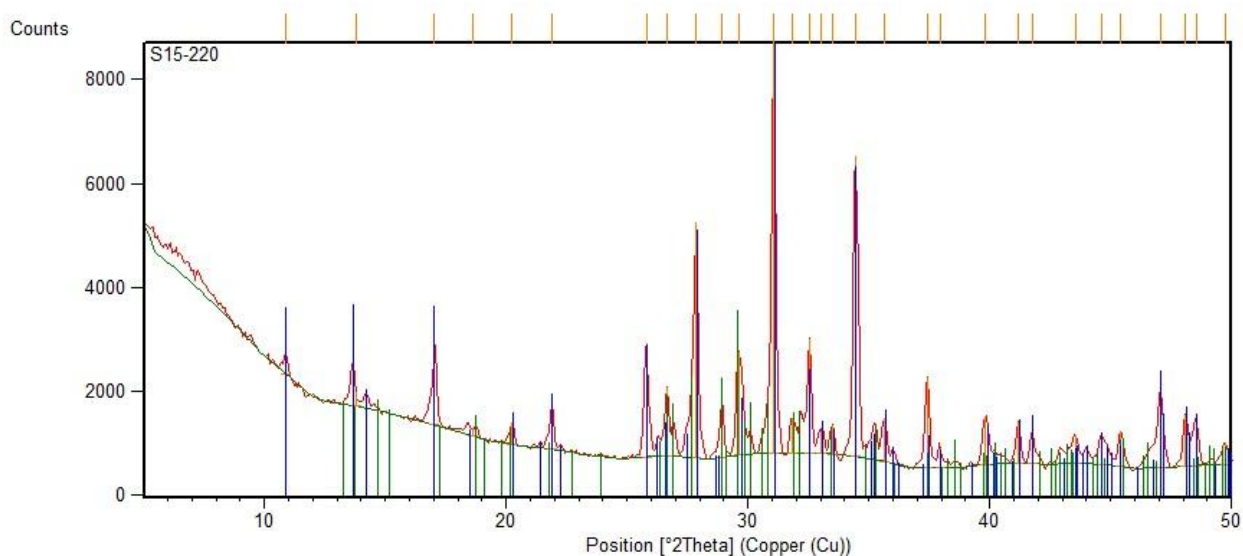


*Fig. 74 – Experimental X ray diffraction pattern of the dried product of Synthesis 14 with peak position of reference patterns.*

- **Scanning Electron Microscopy (SEM) morphological characterization**

SEM images ( reported in *Fig.75* ) reveals large particles over 20  $\mu\text{m}$  in size. Particle's surface shows smaller crystalline structures resulting from solid state reaction grain growth process.

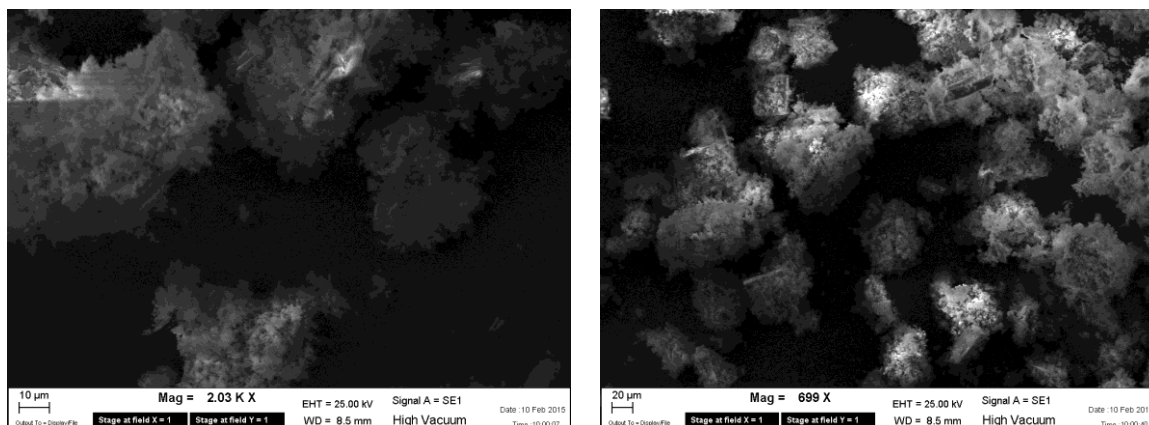


*Fig. 75 – SEM images of the dried product of Synthesis 14*

- **ICP-OES Quantitative analysis**

By ICP-OES measurement, Magnesium content have been determined in Mg-substituted sample. After washing the powder with water to remove soluble salts and dry again, the analysis revealed a Magnesium content within the sample of 0.68 % w/w. By considering the molar masses and stoichiometry, Magnesium resulted to be 2.97 % in moles with respect to Calcium, defining an average stoichiometry expressed by:  $\text{Ca}_{2.91}\text{Mg}_{0.09}(\text{PO}_4)_2$ .

### 3.2.1.11- BIOMIMETIC POROUS SCAFFOLD CHARACTERIZATION (*Synthesis 15*)

Hydroxyapatite/Tricalcium phosphate biphasic ceramics have been widely studied as biomaterials for many implantological applications due to their optimal biocompatibility/bioabsorbability features [S. E. Lobo, et al. 2010]. An attempt to one-step synthesis of solid scaffold by biomimetic approach is performed in synthesis 15 and 16, with the aim of obtaining HA/TCP(Mg) phase mixture and porous complex morphologies to improve cells attachments.

#### • X-ray powder diffraction Characterization

X ray diffraction pattern obtained by grounded powders ( reported if *Fig.76* ) confirms the presence of crystalline  $\beta$ -Tricalcium phosphate. As expected, part of  $\beta$ -TCP phase thermally converted in Calcium deficient apatitic structure [Y. M. Kong et al, 2008], resulting in an HA/TCP biphasic ceramic. Composition have been approximately determined by RIR method and consist of 50 % w/w Hydroxyapatite, 50% w/w  $\beta$ -Tricalcium phosphate ( reference ICSD codes: 01-077-0692 for  $\beta$ -Tricalcium phosphate, 01-086-0740 for Hydroxyapatite ).

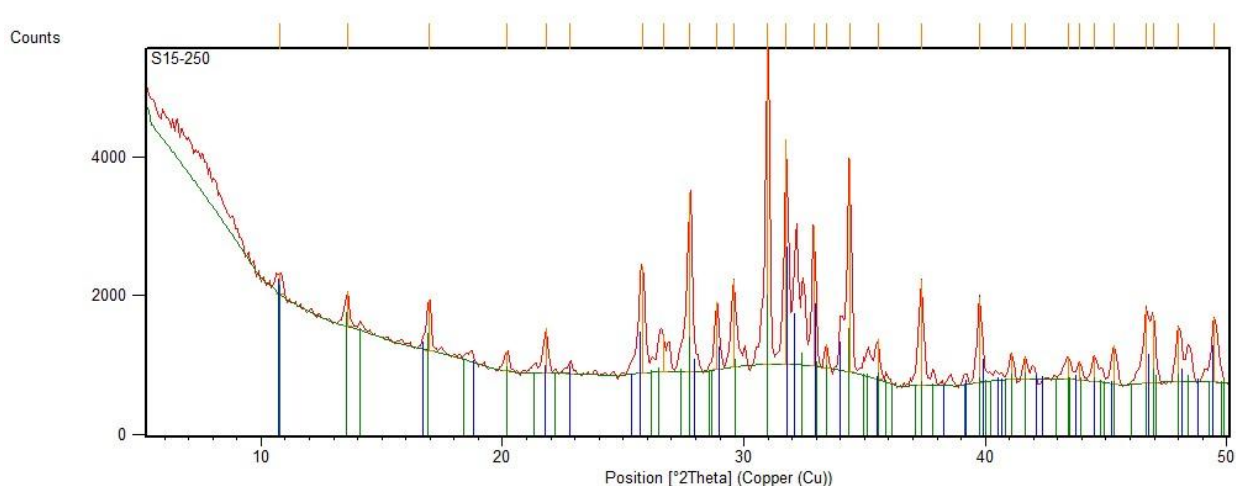


*Fig. 76 – Experimental X ray diffraction pattern of the product of Synthesis 15 with peak position of reference patterns.*

- **Scanning Electron Microscopy (SEM) morphological characterization**

SEM images ( reported in *Fig. 77* ) shows that the microstructure of the sponge *Euspongia officinalis* is maintained in the inorganic scaffold. Mesopores and fibrous hierarchical structures appears covered on the surface by crystalline structures arising from solid state reaction grain growth process.

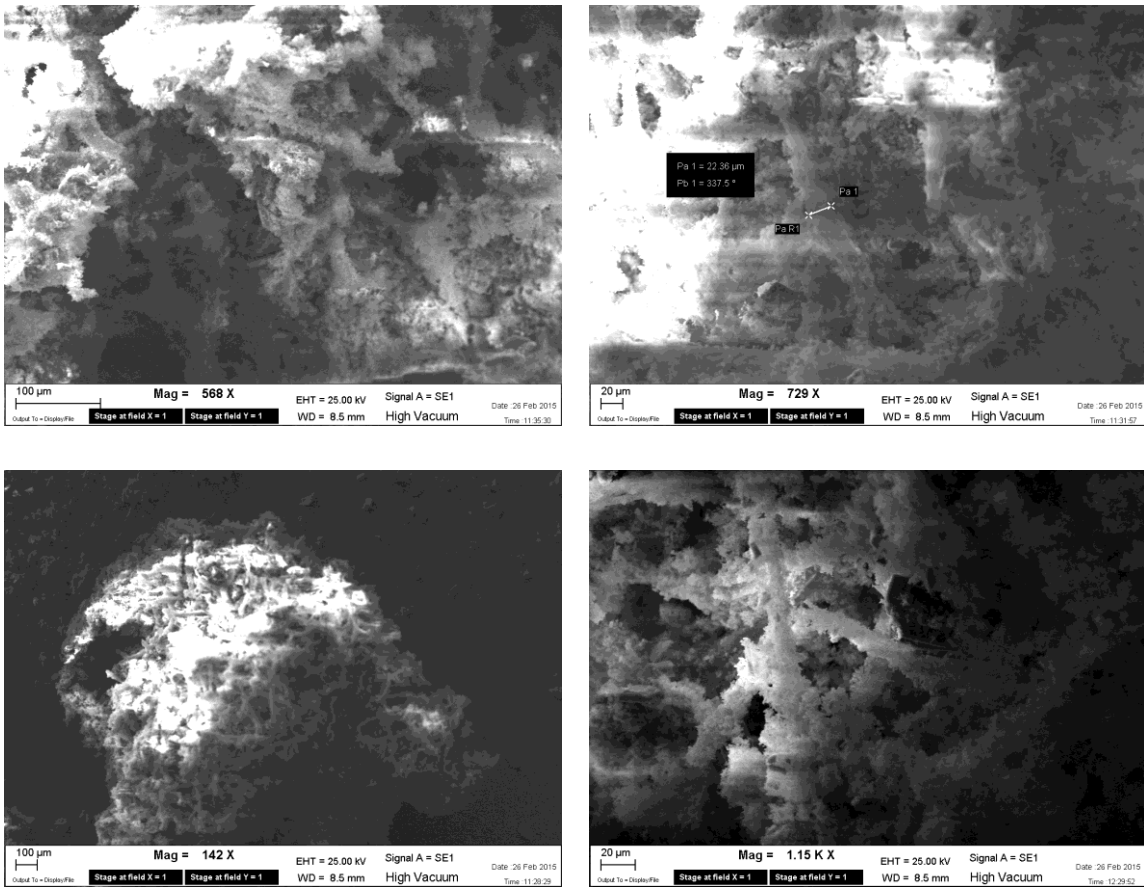


*Fig. 77 – SEM images of the microstructures of the sponge Euspongia officinalis, maintained in the product of Synthesis 15*

Unfortunately, the solidity of the sample was insufficient for practical applications.

### 3.2.1.12- BIOMIMETIC POROUS SCAFFOLD CHARACTERIZATION

(*Synthesis 16* )

- **X-ray powder diffraction Characterization**

X-ray diffraction pattern obtained from the grounded powders ( reported if *Fig.78* ) revealed the presence of three main crystalline phases:  $\beta$ -Tricalcium phosphate, Hydroxylapatite and a relevant amount of Calcium oxide, suggesting that no complete conversion of reactants into TCP occurred. The weight composition of the mixture approximately estimated by RIR method, consists of 45 % w/w Hydroxyapatite, 35 % w/w  $\beta$ -Tricalcium phosphate and 20 % w/w Calcium oxide ( reference ICSD codes: 01-077-0692 for  $\beta$ -Tricalcium phosphate, 01-086-0740 for Hydroxyapatite, 00-048-1467 for Calcium oxide).

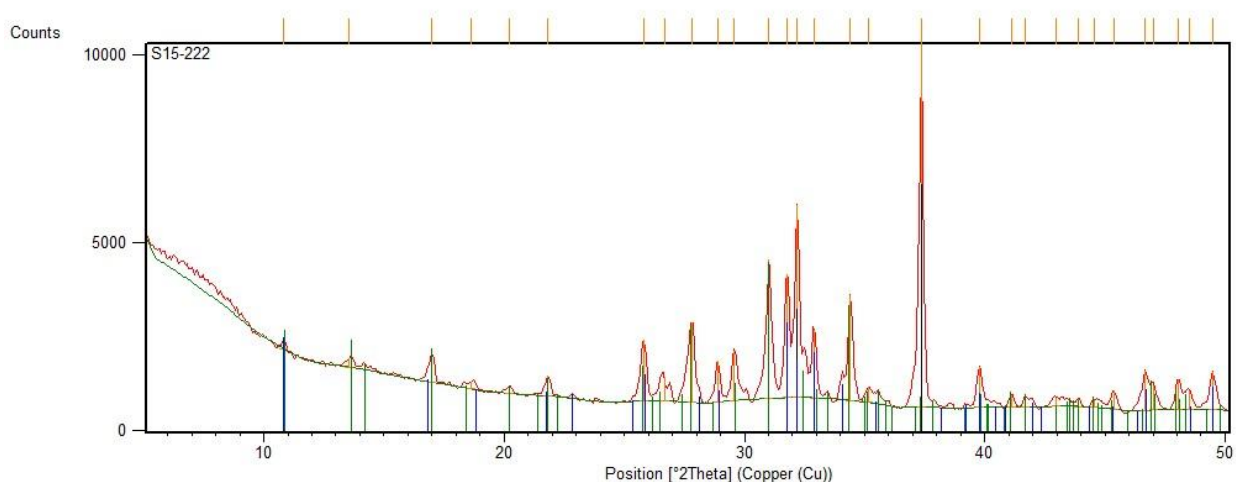


*Fig. 78 – Experimental X ray diffraction pattern of the product of Synthesis 16 with peak position of reference patterns.*

- **Scanning Electron Microscopy (SEM) morphological characterization**

SEM images ( reported in *Fig. 79* ) shows that the microstructure of the sponge *Euspongia officinalis* is maintained in the inorganic scaffold. Mesoporous cavities and fibrous hierarchical structures appears perfectly defined in this sample, also characterized by a higher solidity with respect to the *Synthesis 15* product. On the other hand the not negligible Calcium oxide content is surely incompatible with cell colonization .

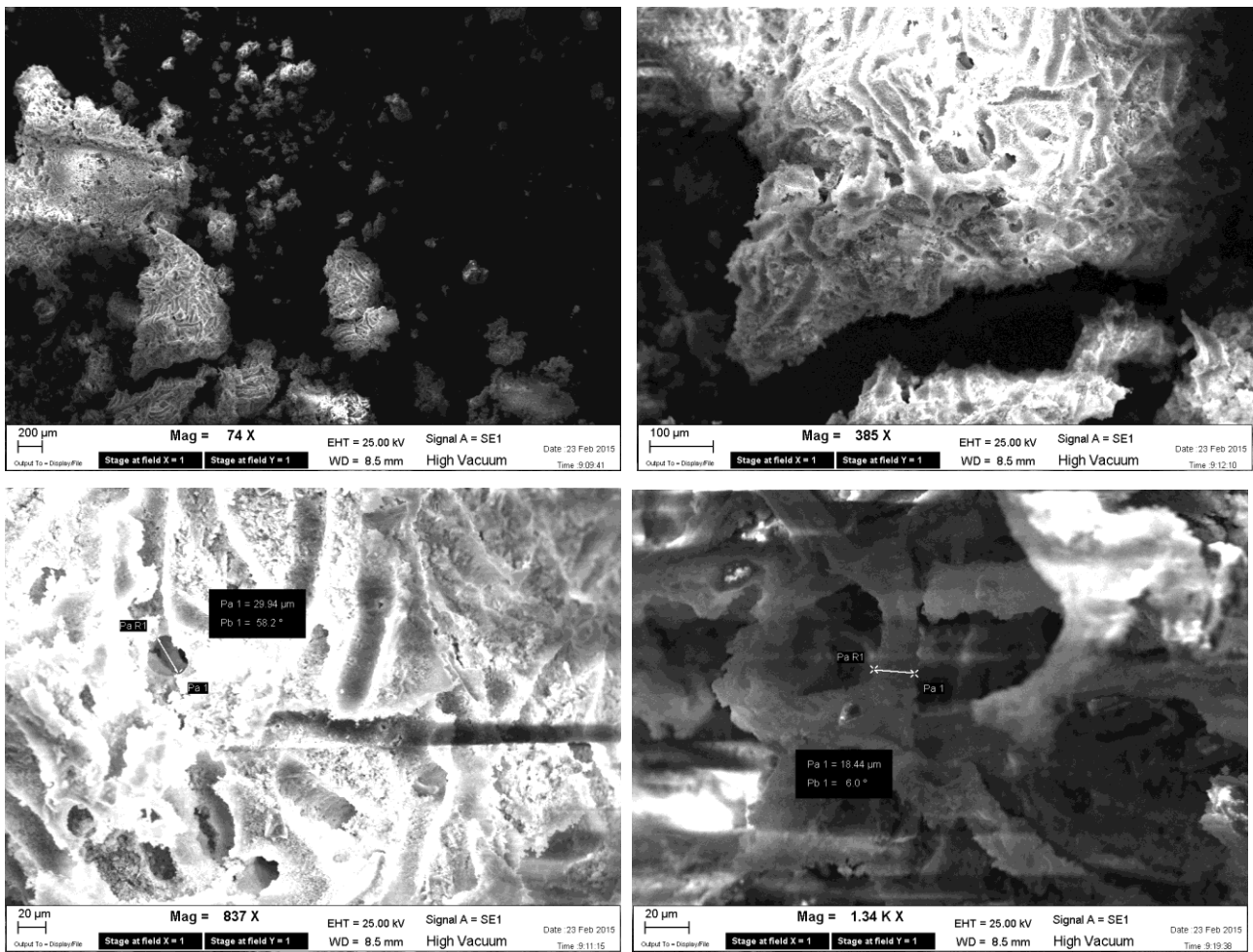


Fig. 79 – SEM images of the microstructures of the sponge *Euspongia officinalis*, perfectly maintained in the product of Synthesis 16

### 3.2.2- CALCIUM PHOSPHATES FOR BIOMEDICAL DRUG DELIVERY

#### 3.2.2.1- ANTICANCER Pt COMPLEXES PHYSISORPTION ON

#### HYDROXYAPATITE ( *Synthesis 17- 18* )

Surface physisorption properties of synthesized Hydroxyapatite have been tested on two different square- planar Platinum complexes, EP230 (Kiteplatin) and SMF30, known to be anticancer drugs [N. Margiotta et al., 2012]. Complexes brief description is reported in Experimental section.

These Platinum complexes have been tested in Colo-rectal cancer treatments, but also in *in situ* treatments for bone tumors: by functionalization with bis-phosphonate groups and adsorption on Hydroxyapatite nanocrystals, a Calcium phosphate based bone filler providing controlled release of drugs have been prepared [Iafisco et al., 2009]. It is reported that the critical step in drug release is the Phosphonate-Platinum bond cleavage and complex release in its active form, i.e with two Chlorine atoms coming from the physiological environment bound to Platinum. Taking inspiration from this work a simplified system have been tested for local controlled delivery of Platinum based drugs, directly in its active form. The anticancer complexes have been adsorbed directly on Hydroxyapatite nanocrystals surface (obtained by *Synthesis 4* ) within a phosphate buffer solution. Filtered and dried solid product have been used to prepare a locally injectable suspension with the aim to obtain a fast release of the drugs selectively focused on tumoral tissue surrounding environment, driven by pH falls which is known to be characteristic of cancer cells [A.L. Hashim et al., 2011].

- **ICP-OES Quantitative analysis**

Adsorption of anticancer drug described in experimental section have been monitored by determining Platinum concentration within buffer solution along time. Results are reported in *Fig. 80*, showing the decrease of Platinum concentration for both complexes *vs* time.

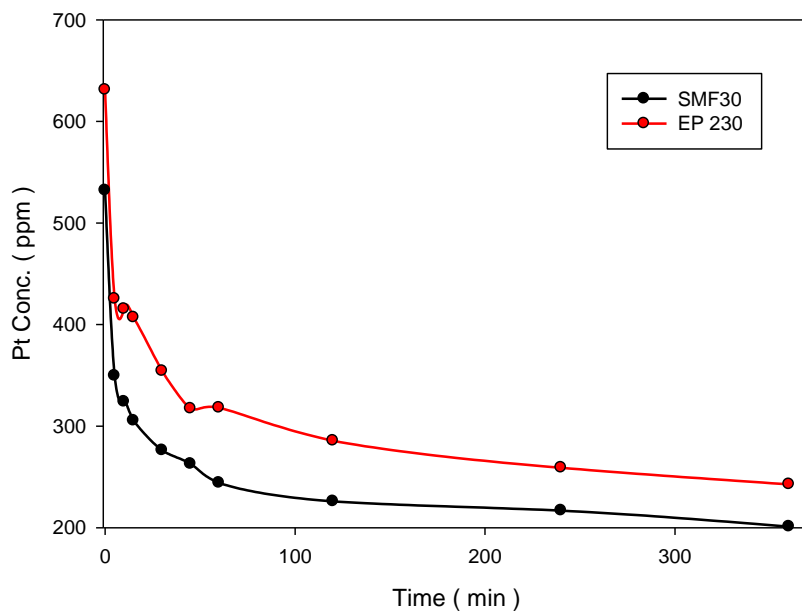


Fig. 80 - Decrease of Platinum concentration in the buffer solution vs time for SMF30 and EP230, due to complexes adsorption on Hydroxyapatite surface

The results expressed as adsorption percentage on total disposable drug are reported in Fig. 81.

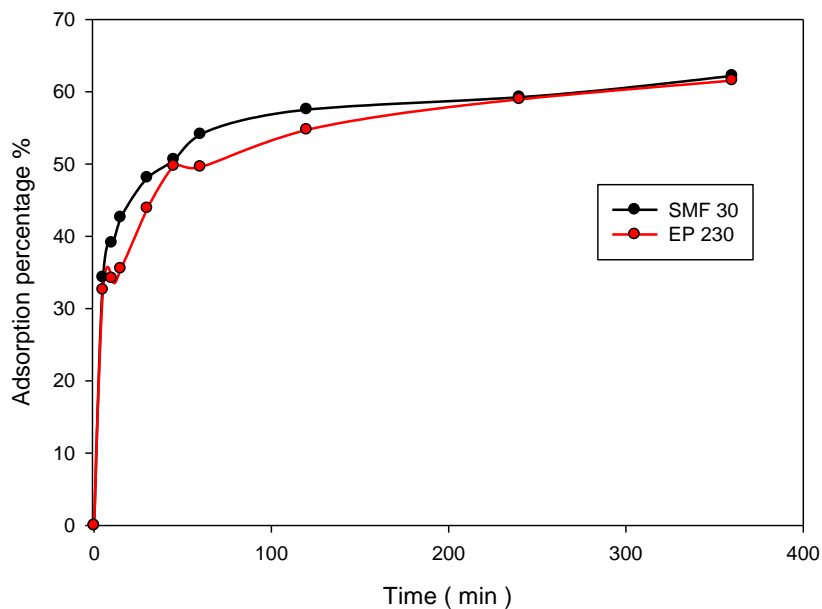


Fig. 81 - Adsorption percentage of total disposable drug vs time for SMF30 and EP230.

For both Platinum complexes the adsorption percentage reach the plateau value of about 60% within 120 minutes, independently by drug water solubility. This suggests that the adsorption process is uniquely affected by the surface area of the Hydroxyapatite carrier, estimated in about  $1 \text{ m}^2$  in the reported conditions.

- **Scanning Electron Microscopy (SEM) morphological characterization**

In Fig. 82 SEM images of dried Hydroxyapatite aggregates after Pt complexes adsorption are reported. No effect on aggregates morphology is observed.

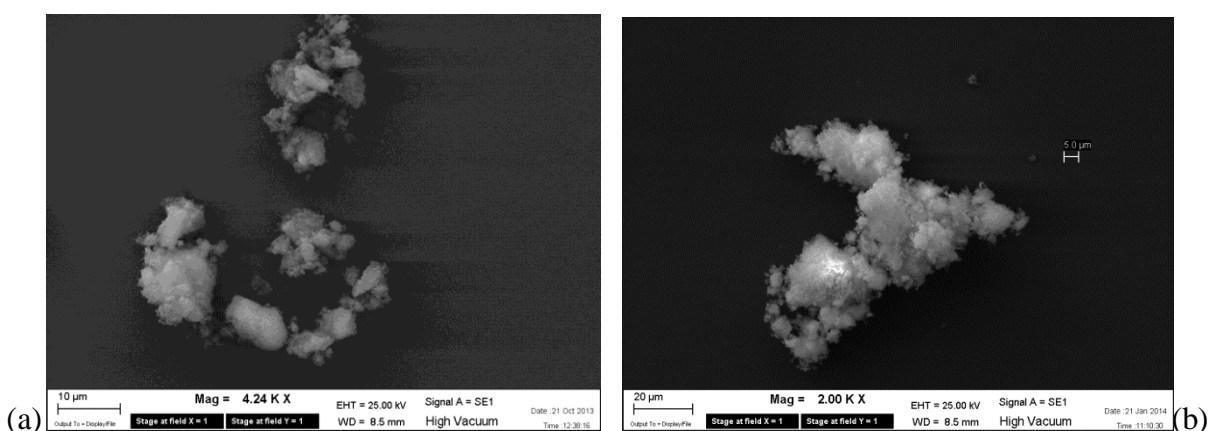


Fig. 82 – SEM images of the dried product of Synthesis 17(a), and of the pure hydroxyapatite obtained by Synthesis 4(b). Differences in aggregates morphology are not visible

EDS microanalysis performed on aggregates reveals the characteristic emission peaks of Platinum, confirming presence of the drug on the dried powders Fig. 83.

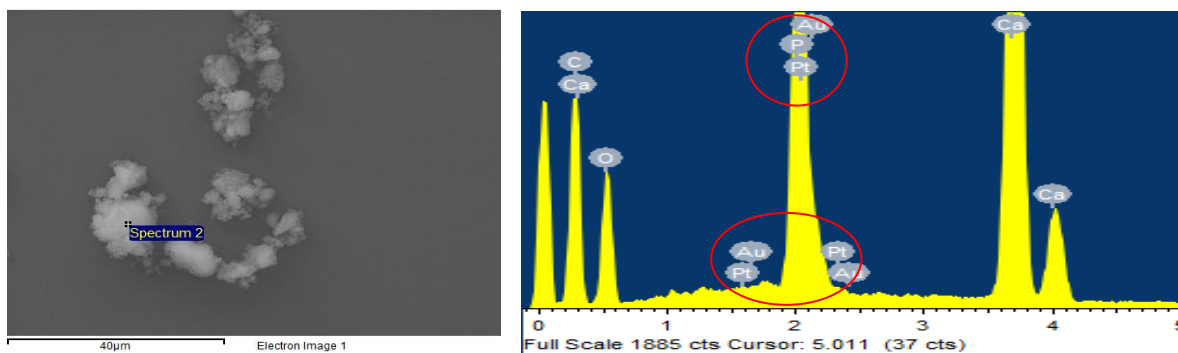
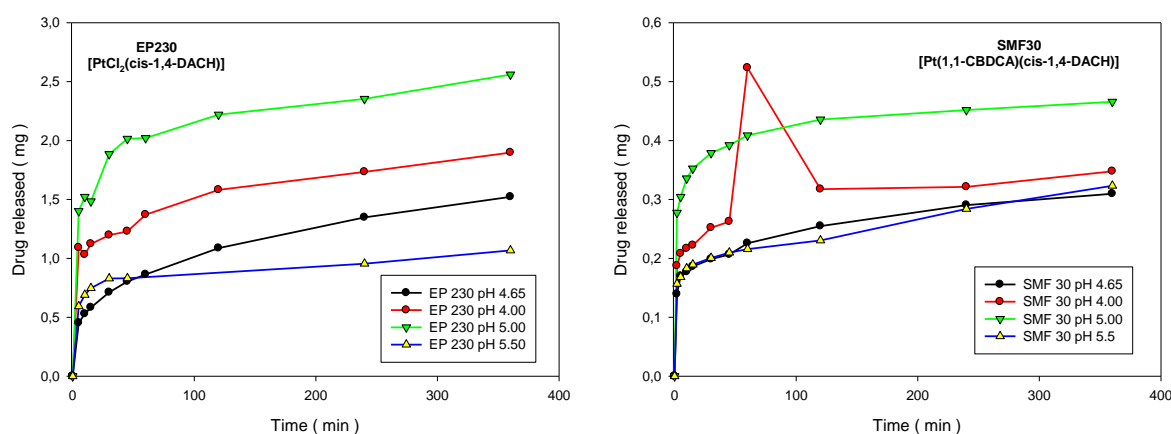


Fig. 83 – SEM images of the dried product of Synthesis 17 and relative EDS spectrum revealing the presence of Platinum by its characteristic emission peaks.

### 3.2.2.2- ANTICANCER Pt COMPLEXES RELEASE FROM HYDROXYAPATITE (Experiment 7)

- ICP-OES Quantitative analysis

Release kinetic of Platinum complexes from Hydroxyapatite surface have been monitored at four different pH values within Citrate buffer solutions. The drug Released amount have been followed by determining the Platinum concentration within the buffer solution along time via ICP-OES analysis. The results are reported in *Fig. 84* as milligrams of released complexes in solution.



*Fig. 84* – Drugs release from hydroxyapatite at different pH. Data reported as milligrams of released complexes in solution.

The results expressed as release percentage on total adsorbed drug at various pH are reported in Fig. 85.

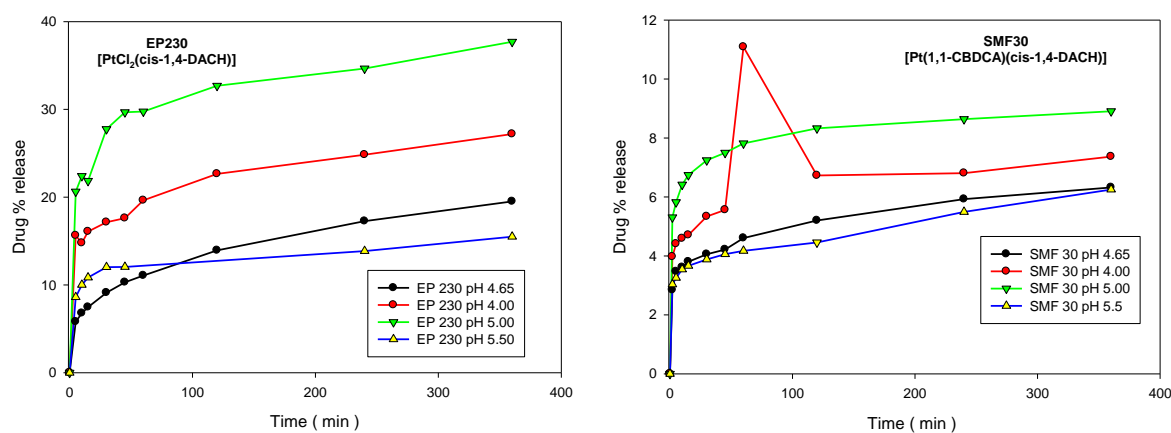


Fig. 85 – Drugs release from hydroxyapatite at different pH. Data reported as released percentage on total disposable (adsorbed) drug

In all cases, a fast release of Platinum complexes is observed and the highest release for both complexes is obtained at pH 5.0. The differences between plateau values for the same drug are probably due to the variation of complex solubility at the test pH. The different solubility between anticancer drugs, 2 mg/mL in water for EP230 and 1 mg/mL for SMF30, determines the significant higher amount of released EP230 compared to SMF30. Further investigation on possible modification of the released drug were not necessary since no others reaction occurs apart physisorption on Calcium phosphate surface.

### **3.2.3- CALCIUM PHOSPHATES FOR PHYTOTHERAPICAL DRUG DELIVERY**

#### **3.2.3.1- PHYTOTHERAPIC DRUGS DELIVERY TEST (*Experiment 8*)**

Phytotherapies using Calcium phosphates have been tested and compared with representative commercial products as reported in experimental section. Copper ions and Sulfur have been chosen because of their effectiveness in common mildew and bacterial plant's diseases treatment, which determined an historical massive use. After one month test, results reported in *Tab.15*, *Tab.16*, *Tab.17* are obtained. The effectiveness have been evaluated by carefully inspecting leaves, bunches and floral buttons. For each part the percentage values of incidence (percentage of affected parts) and severity (percentage of coverage by symptoms) are reported. Results obtained in Downey mildew treatment (*Tab. 15*), shows that Copper sulfate on Hydroxyapatite suspension is capable of significant healing on plant's leaves after 9 applications, comparable to 9 applications of the commercial product. A lower number of applications give appreciable results compared to the untreated reference, but not comparable to 9 applications of the commercial product. The healing effect on bunches is lower, and in any case comparable to applications of the commercial product. The total administered Copper is anyway drastically lower than 9 applications of the commercial product (recommended dosage).

<i>Downy mildew (Peronospora)</i>	dose	Application n°	Administered Cu (g)	Leaves-incidence (%)	Leaves-severity (%)	Bunches-incidence (%)	Bunches-severity (%)
<b>Untreated Reference</b>	-	-	-	<b>100</b>	<b>69.1</b>	<b>100</b>	<b>55.6</b>
<b>CuSO<sub>4</sub>/HA suspension</b>	<b>5.0 l</b>	<b>6</b>	<b>1500</b>	<b>51.3</b>	<b>7.8</b>	<b>93.0</b>	<b>30.9</b>
<b>CuSO<sub>4</sub>/HA suspension</b>	<b>5.0 l</b>	<b>9</b>	<b>2250</b>	<b>38.8</b>	<b>5.6</b>	<b>90.0</b>	<b>24.1</b>
<b>Purchased product (CuSO<sub>4</sub> based)</b>	<b>500 g</b>	<b>9</b>	<b>9600</b>	<b>32.5</b>	<b>4.2</b>	<b>46.5</b>	<b>5.2</b>

*Tab. 15 – Phytoterapic effect evaluation in Downey mildew treatment. Comparison between different applications of Copper sulfate on Hydroxyapatite suspension and a commercial product.*

Results obtained in Powdery mildew treatment ( *Tab. 16* ), shows that Sulfur on Brushite suspension is capable of relevant healing on plant's bunches, comparable to the commercial product. Even if the incidence of symptoms remains a little higher than in the case on the commercial product application, the total administered Sulfur is drastically lower.

<i>Powdery mildew (Oidio)</i>	dose	Application n°	Administered S (g)	Bunches-incidence 15 days (%)	Bunches-severity 15 days (%)	Bunches-incidence 30 days (%)	Bunches-severity 30 days (%)
<b>Untreated Reference</b>	-	-	-	<b>88.0</b>	<b>21.1</b>	<b>98.5</b>	<b>63.7</b>
<b>S/CaHPO<sub>4</sub> *2H<sub>2</sub>O suspension</b>	<b>2.5 l</b>	<b>7</b>	<b>7000</b>	<b>16.0</b>	<b>0.8</b>	<b>79.0</b>	<b>14.5</b>
<b>Purchased product (S based)</b>	<b>5 kg</b>	<b>7</b>	<b>28000</b>	<b>6.5</b>	<b>0.4</b>	<b>67.5</b>	<b>5.1</b>

*Tab. 16 – Phytoterapic effect evaluation in Powdery mildew treatment. Comparison between application of Sulfur on Brushite suspension and a commercial product.*

Results obtained in Kiwi Psa treatment ( *Tab. 17* ), shows that Copper sulfate on Hydroxyapatite suspension is perfectly comparable to the commercial product in terms of healing effectiveness. Even if the incidence of symptoms on floral buttons remains a little higher than in the case on the commercial product application, the total administered Copper is significantly lower.

<i>Kiwi Psa</i>	dose	Application n°	Administered Cu (g)	Floral buttons-incidence (%)	Leaves-incidence (%)	Leaves-severity (%)
<b>Untreated Reference</b>	-	-	-	<b>28.3</b>	<b>32.3</b>	<b>3.9</b>
<b>CuSO<sub>4</sub>/HA suspension</b>	<b>11</b>	<b>6</b>	<b>1116</b>	<b>6.0</b>	<b>8.8</b>	<b>0.8</b>
<b>Purchased product (CuSO<sub>4</sub> based)</b>	<b>0.41</b>	<b>6</b>	<b>1845</b>	<b>2.3</b>	<b>8.0</b>	<b>1.1</b>

*Tab. 17 – Phytoterapic effect evaluation in Kiwi Psa treatment. Comparison between application of Copper sulfate on Hydroxyapatite suspension and a commercial product.*

The most relevant result achieved in these experiments is the obtainment of therapy effectiveness comparable to commercially available products, by administrating a significantly lower dosage of active principles ( -75 % in test against *Peronospora* and *Oidio* ). It is well known that an excess in the usage of these compounds determines phytotoxicity causing various environmental troubles, as soil contamination and pollution of groundwater aquifers. For these reasons the phytotherapic use of Copper ions and Sulfur is nowadays allowed in organic agriculture, but subject to restrictions ( 6 kg/ha/year in the case of Copper ) [CE 889/2008 - 01/01/2009]. By stabilizing these elements on scarcely soluble Calcium phosphate's surface, rain washout is reduced resulting in a longer time availability of active principles in affected sites and consequent reduction of the required dosages. These results show that it is possible to reduce the agriculture's environmental impact while maintaining the organic agriculture requirements and minimizing the production loss.

## 4- CONCLUSIONS AND PERSPECTIVES

In this thesis, the synthesis of nano-micro particles of crystalline inorganic materials and four different applications involving their use, are presented. Inorganic particles have been synthesized following two main criteria: i) the chemical-physical properties of the product have been optimized for the practical application. Therefore, particular attention is given to the particle's dimensions, specific surface area and crystalline phase; ii) both the synthesis and application should be based on a simple procedure, environmental low impact, economical affordability. The synthesis are developed and performed in non-hazardous solvents commonly used in cosmetic and food industry. The use of reaction additives, such as surfactants, stabilizers, capping agents was limited, while the applied reaction conditions are mild and safe, as proposed by the "green chemistry" principles.

In particular, Titanium dioxide nanoparticles have been synthesized by sol-gel hydrolysis/polycondensation reaction of Titanium(IV) isopropoxide in an isopropyl alcohol/water solution. The crystalline composition have been determined by X-ray powder diffraction and corresponds to a polymorphs mixture of 97.7 % w/w Anatase and 2.3 % w/w Brookite with particle dimensions ranging between 10 and 30 nm and a relevant specific surface area of 239.3 m<sup>2</sup>/g. The isopropyl alcohol contained in the solvent mixture act as a capping agent stabilizing the forming nanometric particles, and play also a role in the suspension stability, promoting the particles dispersion and reducing agglomeration. For this reason Titanium dioxide was maintained and also applied as a suspension in the mother solution. Photocatalytic activity tests under UV irradiation were performed both in solution and toward gaseous analytes. Synthesized Titanium dioxide reveals good photocatalytic properties directly as synthesized, without needing further thermal treatment, commonly performed to enhance photoactivity [S. Sakka, 2005]. On the contrary, thermal treatment determined a reduction of photocatalytic activity due to a decrease of the specific surface area.

Photoactive Titanium dioxide have been used for NO<sub>x</sub> pollutants abatement on waste gases produced by a working plant. Preliminary laboratory tests allowed to optimize the application parameters of Titanium dioxide photocatalyzed radical generation to the real conditions. After verifying the catalyst effectiveness on NO<sub>x</sub> removal, a series of evolving prototypes have been realized and tested on field. Also prototypes development took into account environmental impact,

working simplicity and economical affordability. The field tests of the prototypes gave relevant results in term of abatement estimated up to 48% for total NO<sub>x</sub> and 68% for H<sub>2</sub>S, depending on the experimental setup. Variations of the experimental conditions shown that the catalyst exposed area and the analytes/catalyst contact time strongly affect pollutants abatement, while the increase of the irradiation intensity resulted in a catalyst saturation without relevant photoreaction enhancement. Further developments for this project may regard an optimization of the system flow dynamics in order to increase analytes crossing time of catalytic section, and a long period evaluation on catalyst stability and performance maintenance.

In a second application, photoactive Titanium dioxide suspension have been deposited as self-cleaning coating on photovoltaic Silicon panels. By the photoinduced degradation of organic pollutant matter deposited on panel glass surface, the panel loss of transmittance resulting in a decrease of energy production, is avoided. Easy spray application of the catalyst suspension on 46 panels gave surprising results after 1 year long field test, both in terms of effectiveness and weathering stability. In fact, treated panels revealed a mean production gain of +4.96 % compared to untreated reference, still growing after 12 months from application. Unexpected performances lead to hypothesize the presence of a secondary contribution to the production gain: Titanium dioxide nanoparticles may produce a near infrared backscattering effect on panel surface, allowing a lower working temperature of the panel itself. The confirmation of this phenomenon can be obtained by NIR total reflectance measurements. If confirmed, Infrared reflectance may become a key point for further developments.

Crystalline calcium phosphate nano and micro particles, in particular Hydroxyapatite, Brushite, Monetite and Mg-doped  $\beta$ -Tricalcium phosphate have been synthesized, in order to obtain stable and biocompatible inorganic particles suitable for different applications, independently on the environment pH. Two applications of the synthesized Calcium phosphates are reported, both based on the drug delivery concept.

Hydroxyapatite crystals obtained by neutralization reaction appear as fluffy aggregates both in dried conditions and aqueous suspension. The crystal dimension were estimated around 34 nm and the specific surface area was 105.9 m<sup>2</sup>/g. Two Platinum square-planar complexes, already studied as anticancer treatments [*N. Margiotta et al., 2012*] have been loaded on synthesized Hydroxyapatite nanocrystals surface by physisorption. Hydroxyapatite was taken directly by the synthesis mother solution, without drying the solid phase, in order to minimize aggregation of the particles. Drug adsorption have been monitored, showing a fast interaction and reaching a plateau in 120 minutes.

The plateau value was almost equal for both drugs demonstrating that the adsorption is not affected by the different drug solubility, but it is probably related to the Hydroxyapatite surface area. Drug release by dried solid Hydroxyapatite have been monitored in buffer solutions at four different pH values. Fast release is observed within buffer solutions, but differently from the adsorption the amount of released drug was dependent by the environment pH and the drug solubility in water. Hydroxyapatite nanocrystals are able to adsorb and retain on their surface the Platinum complexes, and release them in response to a pH variation. This is interesting for the preparation of a locally injectable suspension of drug charged Hydroxyapatite particles. The release of drug in proximity of cancerous cells, will be driven by the low pH which is known to be characteristic of these cells [A.L. Hashim et al., 2011].

At last, the drug carrier concept kept from biomedical field was addressed to the agriculture. Phytotherapies active elements have been loaded by physisorption on Calcium phosphates particles surface. In particular, Copper sulfate have been charged on Hydroxyapatite nanocrystals (previously described ) and colloidal Sulfur on Brushite microcrystals obtained by *Synthesis 8*. The prepared suspension have been diluted and administered by spray application on cultivations suffering from plant diseases. After one month the effectiveness of the treatment has been evaluated in comparison with a commercial product and an untreated reference. In all the cases, the suspension gave results in terms of healing comparable to the commercial product. The main difference is the total amount of administered phytotherapeutic element, which is drastically lower (-75 % in test against *Peronospora* and *Oidio* ). In fact, scarcely soluble Calcium phosphate particles stabilizes the active principles on their surface, so the rain washout is reduced resulting in a longer availability of active principles in affected sites. The importance of such a result is given by both the opportunity to reduce soil contamination and the capability of minimize the production loss respecting the limits imposed to phytotherapeutic element use in organic agriculture.

In conclusion, the results obtained in this thesis show how the modulation of surface properties of inorganic particles synthesized by following the requirements of simple procedure, environmental low impact and economical affordability, can be crucial in different practical applications.

## 5- BIBLIOGRAPHY

- *J. Angelo, L. Andrade, L. Madeira, A. Mendes, J. Environ. Management, 129, 2013, 522-539*
- *J. Boczkowski, S. Lanone, Rev. Franc. Allerg., vol. 50, 3, 2010, 214-216*
- *M. C. Canela, R. M. Alberici, W. F. Jardim, J. Photochem. Photobiol. A: Chemistry, 112, 1998, 73-80*
- CE 889/2008 - 01/01/2009
- *F. Chen, Y. Zhu, J. Wu, P. Huang, D. Cui, Nano Biomed. Eng, 4, 2012, 41-49*
- *J.S. Dalton, P.A. Janes, N.G. Jones, J.A.Nicholson, K.R. Hallam, G.C. Allen, Environ. Poll., 120, 2002, 415-422*
- *M. F. J. Dijkstra, A. Michorius, H. Buwalda, H. J. Panneman, J. Winkelmann, A.A.C.M. Beenackers, Catal. Today 66, 2001, 487*
- *N. T. Dung, N. V. Koha, J. M. Hermann, Inter. J. Photoenergy, 7, 2005, 11*
- *Estensione del decreto ministeriale 25-08-2000 all.4 comma 2 D.M. 12-07-1990*
- *V.Fang, J. Kennedy, J. Futter, J. Manning, GNS Science report 39, 2013*
- *D. Fowler; et al. New Phytologist 139, 1998, 11–23*
- *L. Frazer, Environ. Health Persp.109, 4, 2011, 174-177*
- *A. Fujishima, TiO<sub>2</sub> photocatalysis: fundamentals and applications, Tokio BKC, 1999*
- *A. Fujishima, T. N. Rao, D. A. Tryk, J. Of Photochem. Photobiol., C: Photochem. Rew., 1, 2000, 1-21.*
- *T. Fukui, K. Murata, S. Ohara, H. Abe, M. Naito, K. Nogi, J. of Pow. Sour., 125,1, 2004, 17-21*
- *E.Gaffet, Comptes rendus de l'Academie des Sciences - Physics,12, 2011, 648-658*
- *I.S. Harding, N. Rashid, K.A. Hing, Biomaterials, 34, 2005, 6818–6826*
- *A.L. Hashim, X. Zhang, J.W. Wojtkowiak, G.V. Martinez, R.J. Gillies, NMR Biomed., 6, 2011, 582-591*
- *K. Hashimoto, H. Irie, A. Fujishima, Jap. J. of Appl. Phys., 12, 2005, 8269-8285*
- *J. M. Hermann, Catal. Today, 53, 1999, 115-129*
- *I.T. Horvath, Encycl. Catal., 5, 2003, 577*
- *A.Houas et al., Applied Catalysis B: Environmental 31, 2001, 145-157*

- M. Iafisco, B. Palazzo, M. Marchetti, N. Margiotta, R. Ostuni, G. Natile, M. Mopurgo, V. Gandin, C. Marzano, N. Roveri, *J. Mater. Chem.*, 19, 2009, 8385-8392
- ISO 9277, 2010
- ISO/TS27678, *Nanotechnology- Terminology and definitions*, Sept. 2008
- K. Kabra, R. Chaudhary, R. Sawhney, *Indian Eng. Chem. Res.* 43, 2004, 7683
- J. K. Kaldellis, A. Kokala, *Energy* 35, 2010, 4862-4869
- Knözinger, Helmut and Kochloefl, Karl (2002) "Heterogeneous Catalysis and Solid Catalysts" in *Ullmann's Encyclopedia of Industrial Chemistry*, Wiley-VCH, Weinheim.
- Y. M. Kong, H. E. Kim, H. W. Kim, *J. Biomed. Mater. Res :B Appl. Biomater.* 84, 2008, 334-339.
- I. K. Konstantinou, T. A. Albanis, *Appl. Catal. B: Environ.* 49, 2004, 1
- Kronos international, 1996
- N. Lyczko, A. Nzihou, P. Sharrak, *Proc. Eng.*, 83, 2014, 423-431
- S. E. Lobo, T. N. Arinzeh, *Materials*, 3 , 2010, 815-826
- J.T.Lue, *Enc. Nanoscien. Nanotech.*, vol. 10, 1-46
- T. Luttrell, S. Halpegamage, J. Tao, A. Kramer, E. Sutter, M. Batzill, *Scient. Reports*, 4:4043, 2014.
- Z. Ma, F. Zaera, *Enc. Of Inorg. Chem.*, 2006, Wiley ed.
- N. Margiotta, C. Marzano, V. Gandin, D. Osella, M. Ravera, E. Gabano, J.A. Platts, E. Petruzzella, J. D. Heoschele, G. Natile, *J. Med. Chem.*, 16, 2012, 7182-7192
- A. Millis, S. Le Hunte, *J. Photochem. Photobiol. A* 108, 1997, 1
- C. Minero, D. Vione, *Appl. Catal. B: Environ.*, 67, 2006, 257
- P. Pascaud, F. Errasifi, F. Brouillett, S. Sarda, A. Barrough, A. Legrouri, C. Rey, *J. Of Mater. Scien.: Mater. And Med.*, 10, 2014
- Patent WO 2005/082780 MENARINI
- M. Pelaez, N. Nolan, S. Pillai, M. Seery, P. Falaras, *Appl. Catal.B: Environ.* 2012
- J. Perkowsky, S. Bzdon, A. Bulska, W. K. Jozwiak, *Polish J. Environ. Stud.* 15, 2003, 457
- M. A. Rauf, M. A. Meetani, A. Khaleel, A. Ahmed, *Chem. Eng. Journal*, 157, 2010, 373-378
- N. Riaz, M. Bustam, C. Kait, Z. B. Man, M. Khan, A. M. Shariff, *Scient. World. J.*, 6, 2014
- A. Roucoux, J. Shoultz, H. Patin, *Chem. Rev.*, 102, 2002, 3757-3778
- N. Roveri, E. Foresti, M. Lelli, I. G. Lesci and M. Marchetti , *Microscopy: Science, Technology, Applications and Education*, 1868-1879, 2010

- *E. Sassoni, E. D'Amen, E. Franzoni, N. Roveri, Material letters, submitted*
- *S. Sakka, Handbook of sol-gel science and technology, Kluwer academic publisher, 2005*
- *R. K. Singh, H. W. Kim, Tiss. Eng. Regen. Med., 6, 2013, 296-309*
- *E. Skoplaki, J.A.Palivos, Solar Energy 83, 2009, 614-624*
- *Y. Tezuka, S. Shin, T. Lshii, T. Ejima, S. Suzuki, S. Sato, J. Phys. Soc. Jpn. 63, 347, 1994*
- *E. Verron, I. Khairoun, J. Guichex, J.M.Bouler, Drug Disc. Tod., vol 15, 2010, 547-552*
- *K. Wang, C. Zhou, Y. Hong, X. Zhang, Interface focus, 2, 2012, 259-277*
- *P. Wardman, J. Phys. Chem., 18, 1989, 1637-175*
- *P. Wilhelm, D. Stephan, J. of Photochem. and Photobiol. A: Chemistry, 185, 2007, 19-25*
- [www.minerali.it](http://www.minerali.it)
- [www.minfind.com](http://www.minfind.com)
- *S. Xia, L. Zhang, G. Pan, P. Qian, Z. Ni, Phys. Chem. Chem. Phys., 2015, 17, 5345-5351*
- *S. Zalesskiy, V. Ananikov, Organometallics, 31,6, 2012, 2302-2309*
- *T. Zhu, S.P. Gao, J. Phys. Chem.:C, 118 (21), 2014, 11385-11396*